Wp-2 basic investigation of transition effect

Babinsky, Holger; Dupont, Pierre; Polivanov, Pavel; Sidorenko, Andrey; Bur, Reynald; Giepman, Rogier; Schrijer, Ferry; van Oudheusden, Bas; Sansica, Andrea; More Authors

DOI
10.1007/978-3-030-47461-4_3

Publication date
2021

Document Version
Final published version

Published in
Transition Location Effect on Shock Wave Boundary Layer Interaction

Citation (APA)
Babinsky, H., Dupont, P., Polivanov, P., Sidorenko, A., Bur, R., Giepman, R., Schrijer, F., van Oudheusden, B., Sansica, A., & More Authors (2021). Wp-2 basic investigation of transition effect. In P. Doerffer (Ed.), *Transition Location Effect on Shock Wave Boundary Layer Interaction* (pp. 129-225). (Notes on Numerical Fluid Mechanics and Multidisciplinary Design; Vol. 144). SpringerOpen. https://doi.org/10.1007/978-3-030-47461-4_3

WP-2 Basic Investigation of Transition Effect

Holger Babinsky, Pierre Dupont, Pavel Polivanov, Andrey Sidorenko, Reynald Bur, Rogier Giepman, Ferry Schrijer, Bas van Oudheusden, Andrea Sansica, Neil Sandham, Matteo Bernardini, Sergio Pirozzoli, Tomasz Kwiatkowski, and Janusz Sznajder

Abstract An important goal of the TFAST project was to study the effect of the location of transition in relation to the shock wave on the separation size, shock structure and unsteadiness of the interaction area. Boundary layer tripping (by wire or roughness) and flow control devices (Vortex Generators and cold plasma) were used for boundary layer transition induction. As flow control devices were used here in the laminar boundary layer for the first time, their effectiveness in transition induction was an important outcome. It was intended to determine in what way the application of these techniques induces transition. These methods should have a significantly different effect on boundary layer receptivity, i.e. the transition location. Apart from an improved understanding of operation control methods, the main objective was to localize the transition as far downstream as possible while ensuring a turbulent character of interaction. The final objective, involving all the partners, was to build a physical model of transition control devices. Establishing of such model would

---

H. Babinsky (✉)
Department of Engineering, University of Cambridge, Cambridge, UK
e-mail: hb@eng.cam.ac.uk

P. Dupont
Aix-Marseille University, Marseille, France

P. Polivanov · A. Sidorenko
Khristianovich Institute of Theoretical and Applied Mechanics of the Siberian Branch of the RAS, Novosibirsk, Russia

R. Bur
Aeroelasticity and Aeroacoustics Department, ONERA - Aerodynamics, Meudon, France

R. Giepman · F. Schrijer · B. van Oudheusden
Technische Universiteit Delft, Delft, Netherlands

A. Sansica · N. Sandham
University of Southampton, Southampton, UK

M. Bernardini · S. Pirozzoli
Universita di Roma “La Sapienza”, Rome, Italy

T. Kwiatkowski · J. Sznajder
Łukasiewicz Research Network – Institute of Aviation, Warsaw, Poland

P. Doerffer et al. (eds.), *Transition Location Effect on Shock Wave Boundary Layer Interaction*, Notes on Numerical Fluid Mechanics and Multidisciplinary Design 144,
https://doi.org/10.1007/978-3-030-47461-4_3

simplify the numerical approach to flow cases using such devices. This undertaking has strong support from the industry, which wants to include these control devices in the design process. Unfortunately only one method of streamwise vortices was developed and investigated in the presented study.

1 Study of Transition Control Devices Operation

1.1 IUSTI

1.1.1 Tripping Devices Characteristics

Experiments achieved for the natural transitional SWBLI have shown that quite large aspect ratio were obtained $\left(L/\delta_0^* > 150\right)$ with evidences of unsteadiness depending on the shock strength and/or on the unit Reynold number. Moreover, the transition to turbulent flow is not observed along the interaction for this natural case and the reattachment point is found downstream of the impinging shock location. Large eddy Simulations achieved at the IUSTI for similar flows have shown that the size of the interaction as well as the location of the reattachment depends on the level of the upstream perturbations in the laminar boundary layer. The IUSTI's wind tunnel have significantly lower external perturbations than classical high pressure wind tunnel: this could explain the large differences observed on the length scales of the interaction. The upstream level of the perturbations could influence the length of transition along the interaction: higher levels will impose quicker transition, imposing the reattachment of the layer when the flow is turbulent and, as a consequence, a smaller interaction length. In order to validate these results, an attempt was made to modulate the upstream level of perturbations in the incoming boundary layer. Only one type of tripping device, a step, has been investigated for this study. The step spans the entire plate and several heights have been used: from $h = 0.05$ mm to $h = 0.36$ mm which corresponds to a height ratio of respectively $h\delta_h = 0.08$ and 0.56 at $P_0 = 0.4\,\text{atm}$ (respectively 0.11 and 0.8 at $P_0 = 0.8\,\text{atm}$) where δ_h is the boundary layer thickness at the position of the step. The width of the step is of 2 mm. Main parameters are reported in Table 1.

1.1.2 Mean and Turbulent Velocity Fields

For limited heights, the upstream boundary layer remains laminar. Downstream from the separation point, typical profiles for mixing layer can be observed, as well as for the natural case, but RMS levels becomes slightly higher, with maxima near the reattachment of about 20% (to compare with 17% in the natural case). For all cases,

Table 1 Interaction parameters overview with tripped boundary layer

P_0 (atm)	Step	h (mm)	Rehi	x_{trip} (mm)	h/5 h	x_o (mm)
0.4	*Natural interaction*					
						68.4
	Tripped interaction					
	B2	0.100	142	52	0.156	
	B3	0.215	657	52	0.336	
	B4	0.300	1279	52	0.469	
	B5	0.360	1842	52	0.563	
	B6	0.250	1013	40	0.446	75.4
	B7	0.215	617	59	0.316	
0.8	*Natural interaction*					
						77.5
	Tripped interaction					
	B2	0.100	402	52	0.222	
	B3	0.215	1858	52	0.478	
	B4	0.300	3617	52	0.667	
	B5	0.360	5209	52	0.800	
	B6	0.250	2864	40	0.625	96.0
	B7	0.215	1744	59	0.448	

the flow remains clearly separated: backward flow is well observed with maximum reverse velocity up to 7% of the external velocity.

The length of the tripped interactions have been reported on Fig. 32 (chapter "WP-1 Reference Cases of Laminar and Turbulent Interactions"). The effect off the tripping device on the interaction length is clearly visible: the length is decreasing of ≈9% for the 0.4 atm case, but more than 25% in the 0.8 atm case. When normalized with the upstream incompressible boundary layer displacement thickness, the decreases is about 60%. This may be the result of a earlier turbulence transition inside the interaction, promoted by the upstream perturbations, as suggested from the Large Eddy Simulations performed at the IUSTI.

The Van Driest representation of the mean velocity profiles downstream of the tripped interaction (case B3 $P_0 = 0.4$ atm) is compared to the natural case on Fig. 1. We see that a well-defined log-law can be observed for the tripped case. In both cases, downstream from the interaction, the profiles exhibit large velocity fluctuations, higher than expected for a classical turbulent profile: these large fluctuations are the result of the relaxation of the flow, downstream of the interaction. Similar results were obtained in separated turbulent OSWBLI [1]. The near wall downstream boundary layer was recovering very quickly with the development of a new log-law region, based on the downstream wall conditions, while the external part of the layer was out of equilibrium with large energetic eddies shed in the downstream flow.

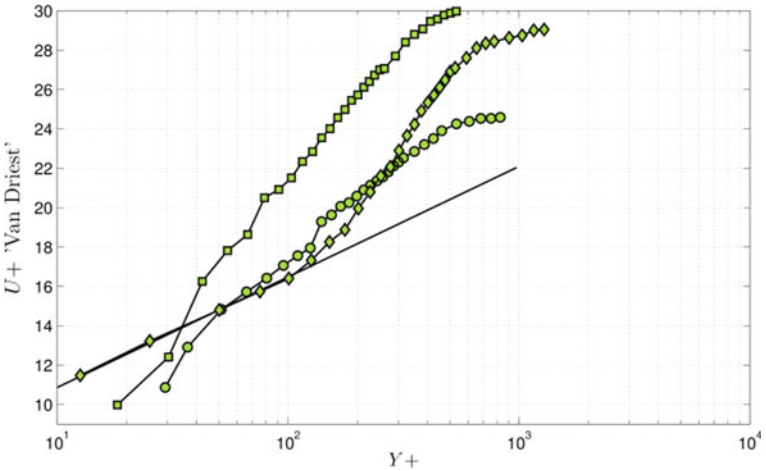

Fig. 1 Van Driest representation of the velocity profile downstream of the interaction ($X^* = 0.35$), Θ_3 angle: :B0, $P_0 = 0.4$ atm, □: B2, $P_0 = 0.4$ atm, ◇: B2, $P_0 = 0.8$ atm

The longitudinal evolution of the maximum value of u' / U_e along the interaction are reported Fig. 33 (chapter "WP-1 Reference Cases of Laminar and Turbulent Interactions") for the tripped case B2 at $P_0 = 0.4$ atm and $P_0 = 0.4$ atm. Very similar amplifications rate than for the natural case are obtained. In cases of tripped interaction, the maximum values are about 20% to compare to the 17% observed in the natural case. Over-imposed on the figure are also reported LES results for increased upstream perturbations (blue line). As for tripped interactions, similar amplification rates and saturation levels are obtained.

1.1.3 Unsteadiness Characterization

The Power Spectral Density (PSD) of the external radiated fluctuations along the interaction, for the B2 0.8 atm case, are presented on Fig. 2a, for the Θ_3 case. The cyan curve represents the upstream tripped laminar boundary layer. Compared to the natural case, we see that the frequencies amplified through the shear layer are similar. Nevertheless, the amplification is rather higher, especially in the 1–10 kHz domain and a typical frequency at 2 kHz is strongly amplified.

Transfer functions are presented on Fig. 15b. The representation is similar to the one used for the natural case. Again, a trend similar to that of natural case is observed. Nevertheless, the maximum amplification rate for frequencies of ≈1–10 kHz is one decade larger for the tripped boundary layer. In the compression waves zone ($X^* = -1$), only the 1–10 kHz domain is strongly amplified. Higher frequency scales are amplified downstream of the compression waves in a more moderate way, with an amplification rate from 2 to 3 times higher than the natural one. These results confirm the unsteady aspect of the transitional interactions, and the high sensitivity

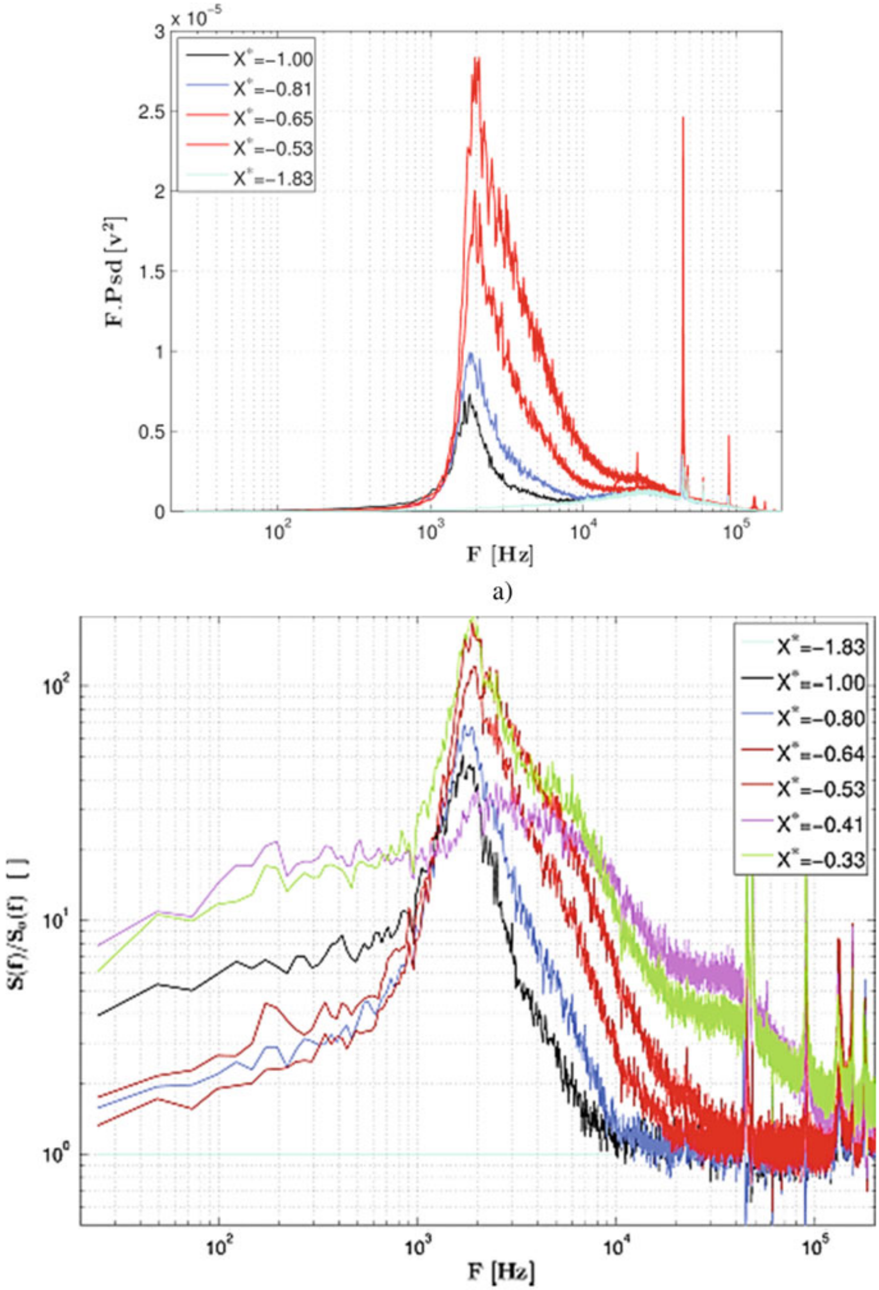

a)

b)

Fig. 2 Θ_3 flow deviation $P_{gen} = 0.8$ atm, tripped boundary layer; **a**: Pre multiplied PSD, **b**: Transfer function

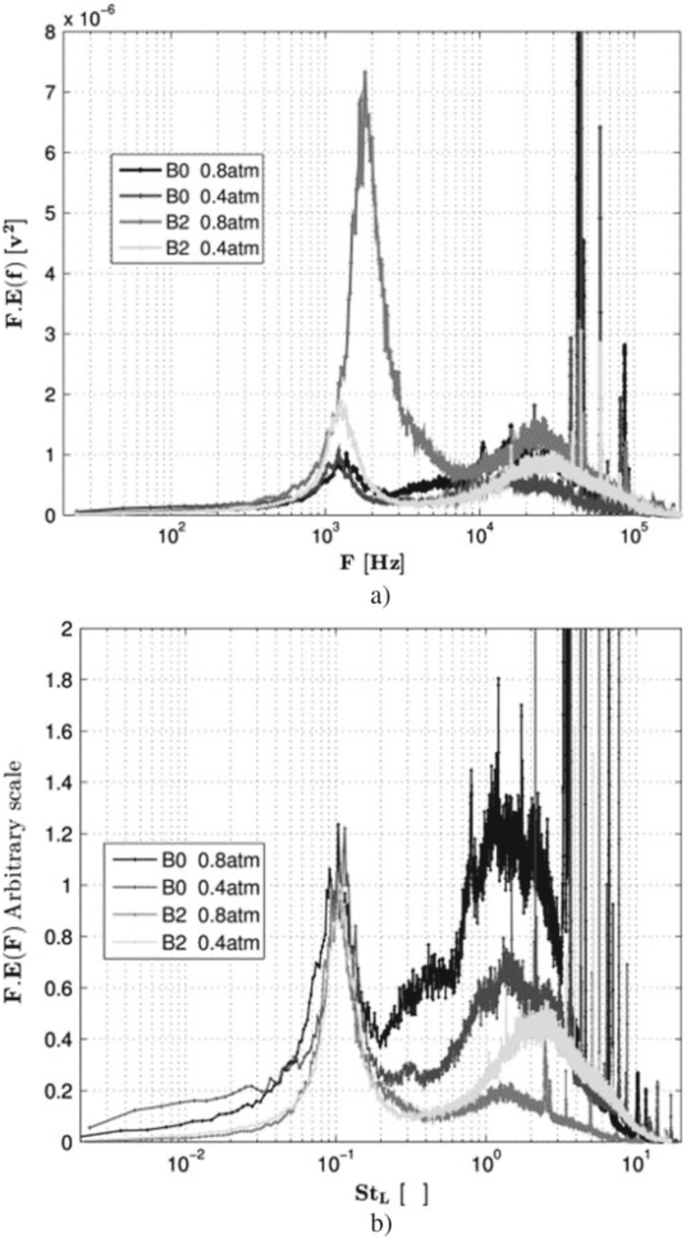

Fig. 3 Pre multiplied PSD, natural (*B*0) and tripped (*B*2) boundary layer, Θ_3 flow deviation, at $P_{gen}=$ 0.4 atm and $P_{gen}=$ 0.8 atm total pressure. **a**: pre-multiplied spectra vs frequency *F*, **b**: normalized pre-multiplied spectra vs Strouhal number $St_L = FL\big/U_1$

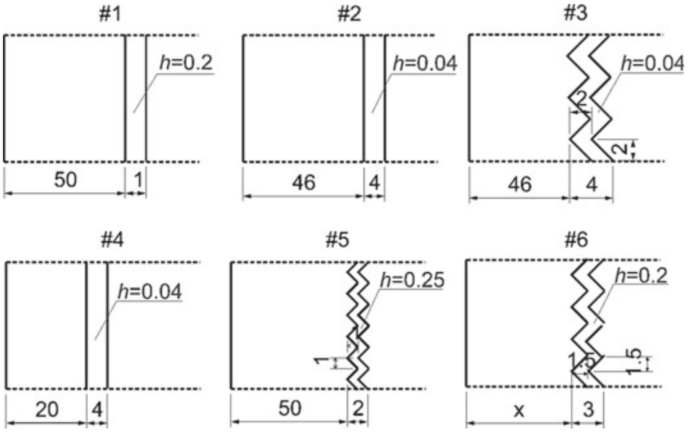

Fig. 4 Roughness elements

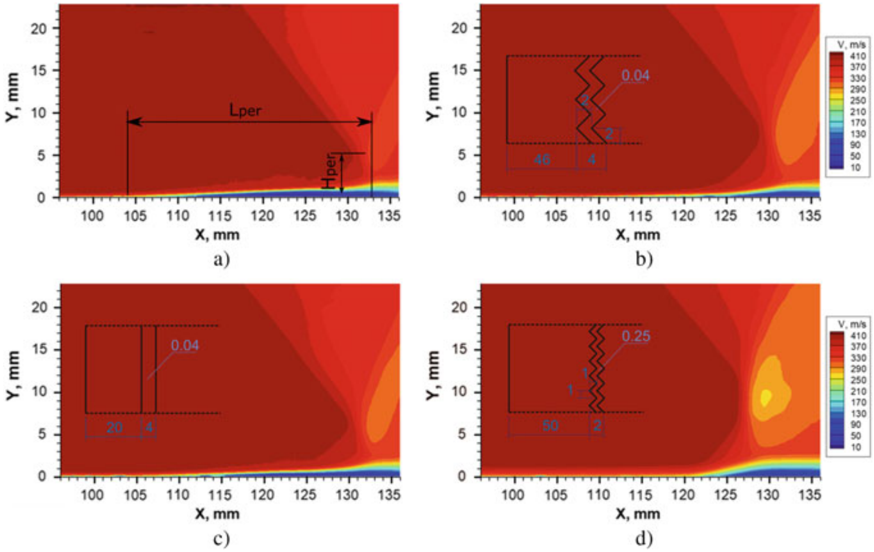

a) b) c) d)

Fig. 5 Velocity fields for different roughness elements: **a** laminar case (reference), **b** #3, **c** #4, **d** #5 $\mathrm{Re}_1 = 10.9 \cdot 10^6\ \mathrm{m}^{-1}$

of such flow to the incoming unsteady conditions: the maximum amplification rate observed is multiply by a factor 10 (20–200), at a frequency of ≈2 kHz.

Figure 3 presents the pre-multiplied PSD measured at the middle of the compression zone ($X^* = -1$) for natural interaction and for *B2 case* tripped interaction, at stagnation pressure of 0.4 atm and 0.8 atm. This figure allows to notice the influence of the tripping on the unsteadiness of the compression zone. We first notice that the amplitude of the oscillation of the compression zone for the tripped interaction (*B2*

Fig. 6 Dimensionless parameters of SWBLI

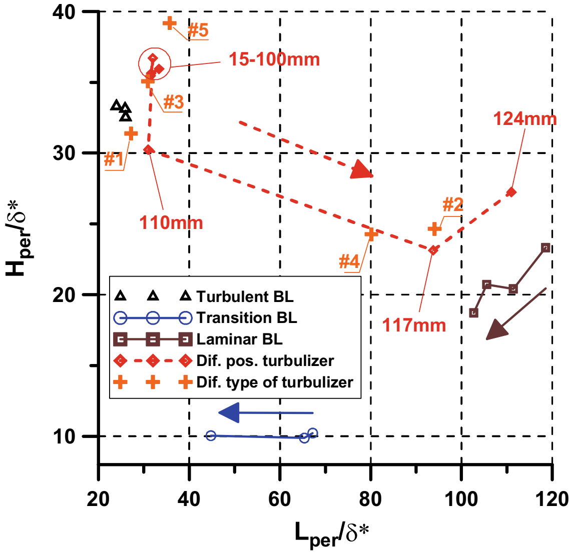

case) is higher than the one of the natural interaction (*B0 case*), both for 0.4 atm and 0.8 *atm* cases. Figure 3 is the dimensionless frequency representation of Fig. 3. The energy of the PSD are normalized to unity. This compilation gives a well-defined Strouhal number of $St_L = 0.10 \left(St_L = FL\big/U_1\right)$ for the low frequency unsteadiness of the compression zone. However, this compilation suffers from the limited extent of the length of interaction variation: it varies from 42.7 to 25.3 mm from natural to tripped interaction.

1.2 ITAM

Passive and active methods were considered for flow control in SWBLI for the case of laminar incoming boundary layer. The main idea was excitation of additional disturbances by a roughness or an electric discharge which should lead to decrease of the separation zone length.

1.2.1 Passive Flow Control Devices

Study of the effect of the surface roughness shape and roughness location was carried out for the case of L = 250 mm and the stagnation pressure $P_0 = 0.7 \times 10^5$ Pa. In this study two types of roughness were considered (Fig. 4). The first type was a straight strip with rectangular cross-section (#1, #2, #4) and the second was a zig-zag strip (#3, #5, #6). As can be seen from the figure, several parameters of the roughness

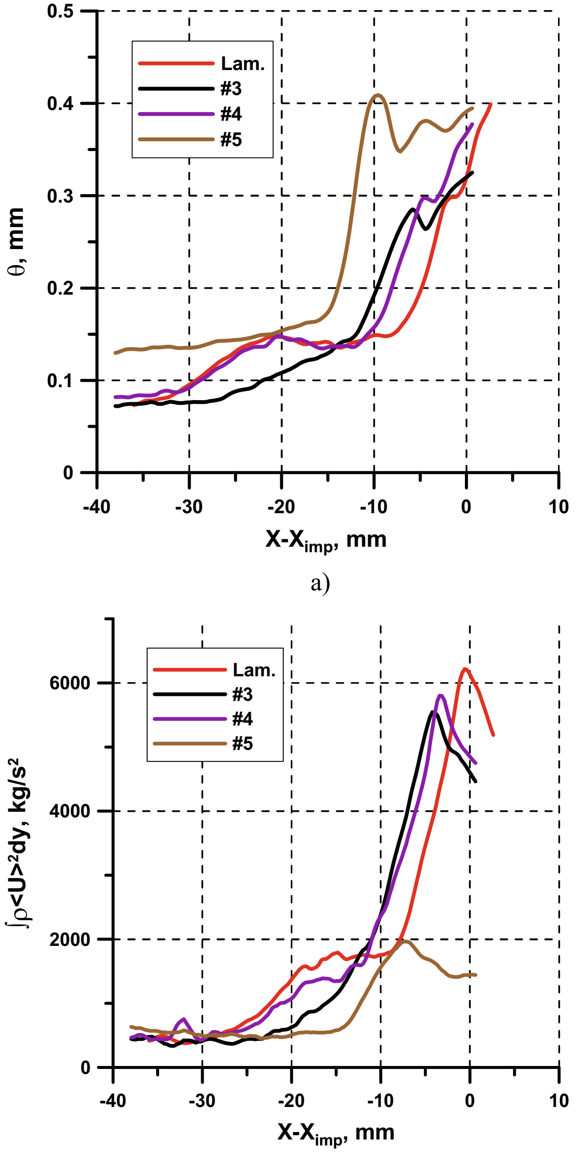

a)

b)

Fig. 7 **a** The momentum thickness distribution and **b** the integrated RMS of velocity fluctuations along the SWBLI for different types of turbulators ($\mathrm{Re}_1 = 10.7 \cdot 10^6\ \mathrm{m}^{-1}$)

were varied namely thickness, width, plane shape and location relative to the leading edge.

It was decided to use such parameters as the length (L_{per}) and height (H_{per}) of the interaction zone normalized by the displacement thickness of the inflow boundary layer ($\delta*$) to make comparative analysis (Fig. 5a). To find L_{per} from PIV data

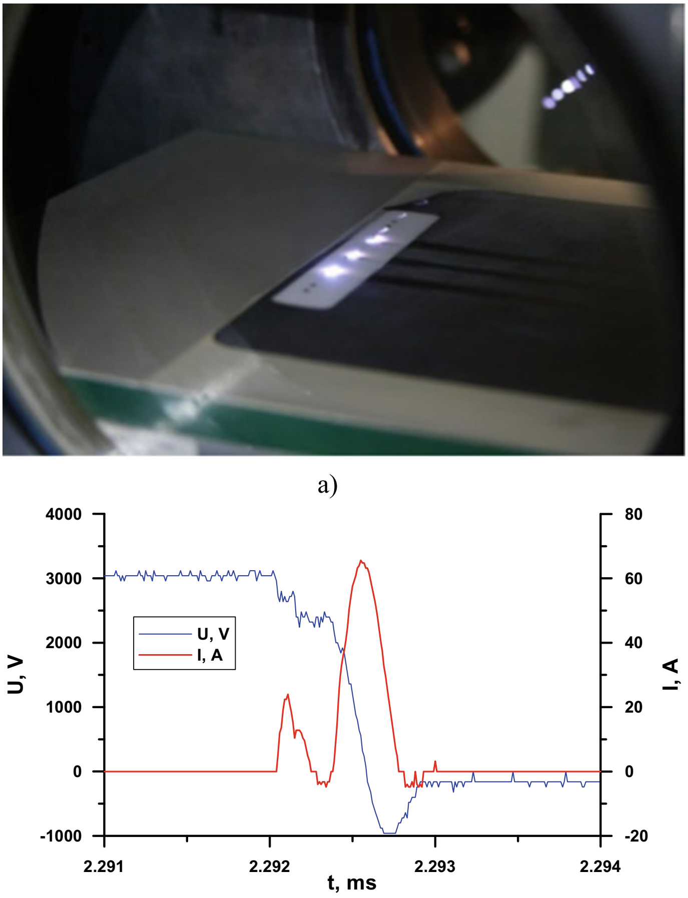
a)

b)

Fig. 8 **a** Model with spark discharge actuator and **b** voltage and current oscillograms

Fig. 9 Spark discharge high voltage generator

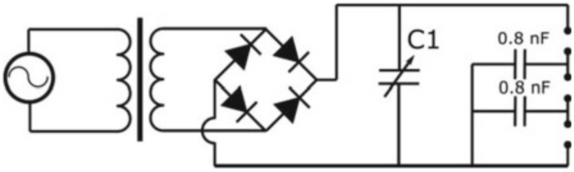

the minimal distance from the wall Y was determined where the reliable velocity measurements had been obtained. For this Y the longitudinal distribution of U was considered. Position where drop of velocity exceeds 5% of the corresponding inflow value was defined as the beginning of interaction. Significant growth of the velocity indicates the end of interaction. Upper border of the interaction H_{per} was defined as

Fig. 10 Discharge characteristics: **a** pulse power and **b** pulse duration vs repetition frequency (average power was approximately 11 W)

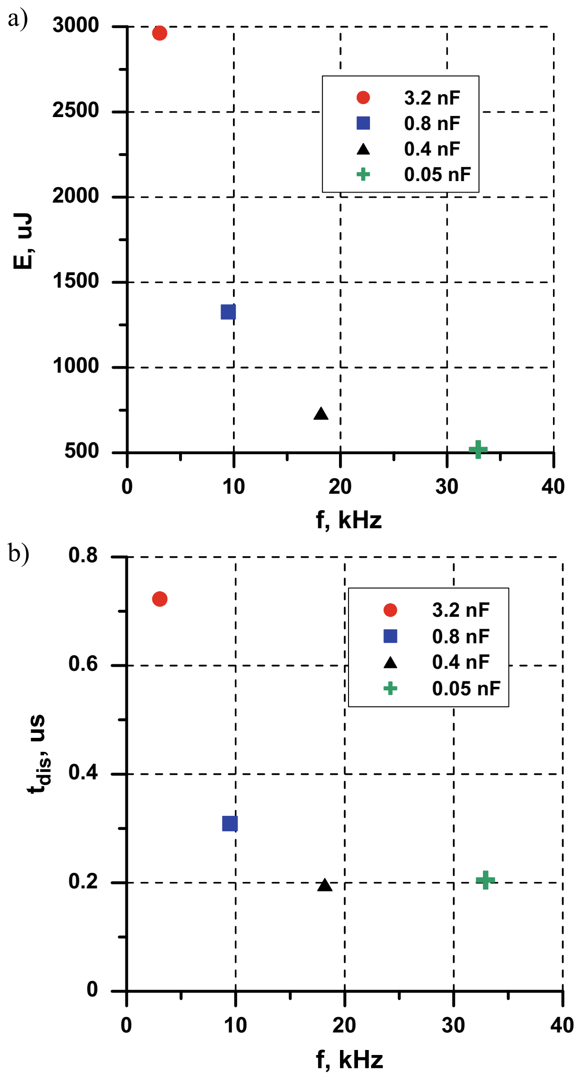

the most downstream point where the flow speed decreased by 5% in comparison with inviscid upstream flow.

The effect the roughness shape on the SWBLI (denoted by plus in Fig. 6) was considered. Flat roughness of low thickness (#2, 4) does not lead to rapid turbulization of the flow (the inflow boundary layer remained laminar) and zone of interaction is close to the laminar case (Fig. 5c). But nevertheless some perturbations were excited leading to decrease of SWBLI length. Flat or zig-zag (#1, 5) roughness of large thickness quickly produced turbulent boundary layer (Fig. 5d). This results in a flow pattern typical for turbulent interaction.

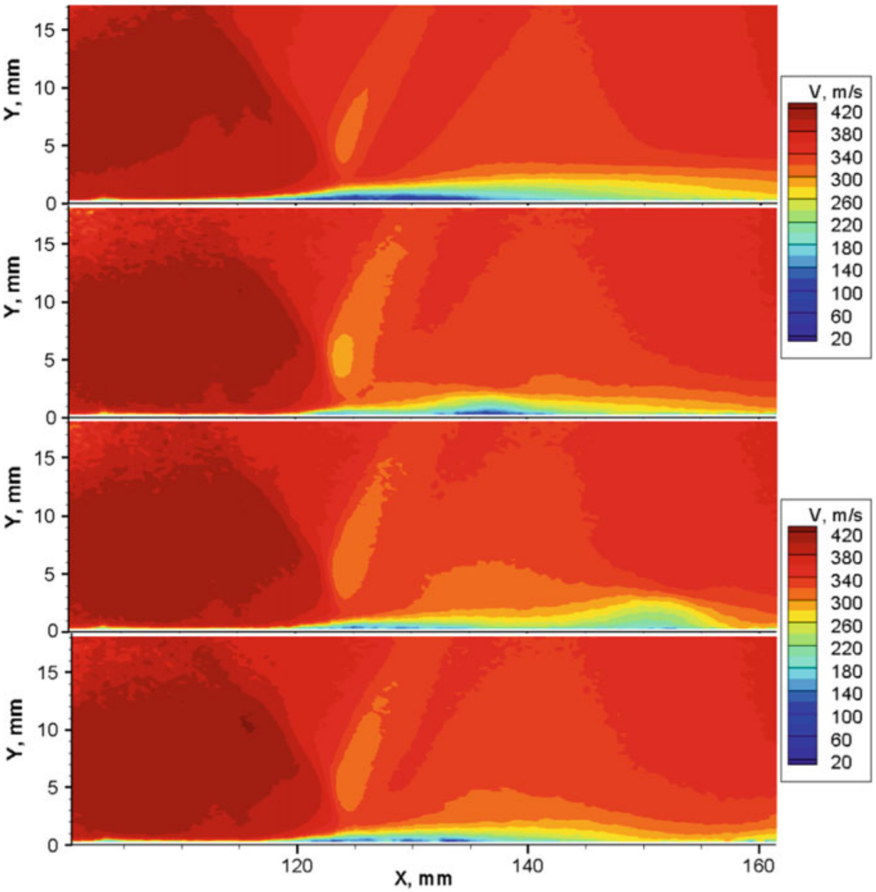

Fig. 11 Mean velocity fields at various discharge phase ($E_{dis} = 0.7$ mJ, $\beta = 4°$). Top to bottom: reference, $\Delta t = 100, 160, 220\ \mu s$

The most interesting data were obtained for the zig-zag roughness of small thickness #3. This roughness does not lead to rapid turbulization of the flow and the boundary layer remained laminar up to the zone of interaction (Fig. 5b). But the length and height of the interaction is much closer to the turbulent case. Most probable that the reason of such behavior is the presence of additional perturbations given by the roughness. The power of perturbations is not sufficient for the flow turbulization flow without adverse pressure gradient but enough to trigger earlier laminar-turbulent transition in the shear layer with presence of adverse pressure gradient in the SWBLI.

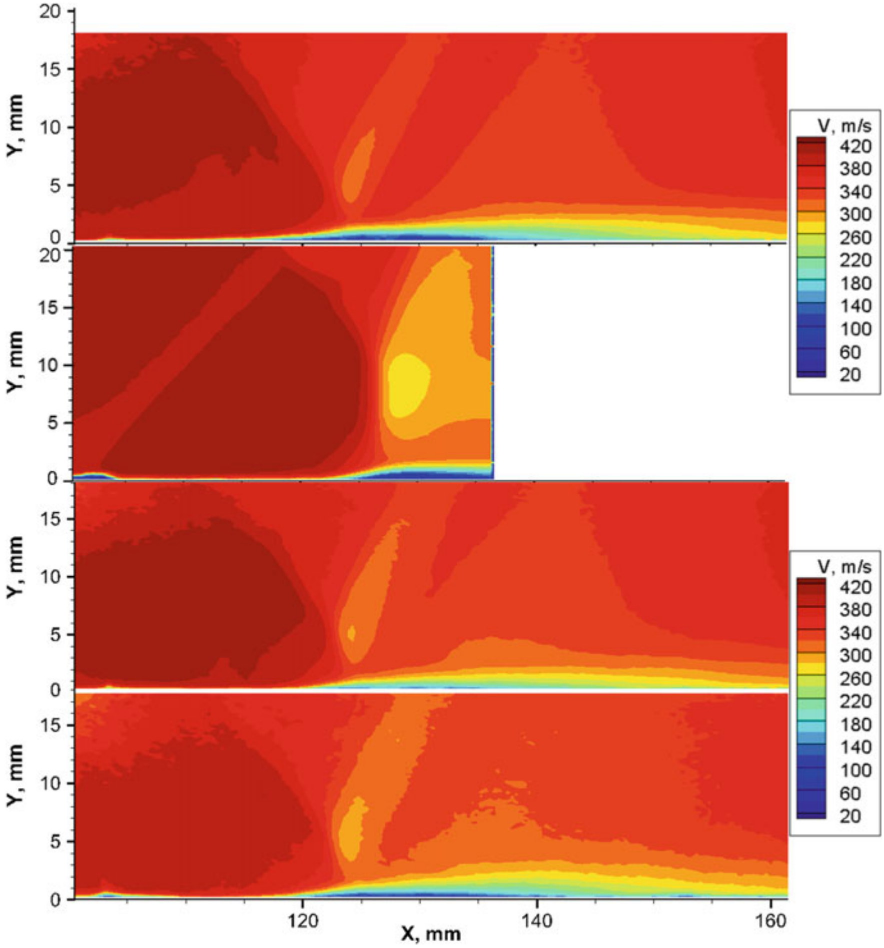

Fig. 12 Mean velocity fields at $\alpha = 4°$. Top to bottom: laminar case, turbulent case, average discharge case $E_{dis} = 0.7$ mJ, $E_{dis} = 1.3$ mJ

The next step was to study the effect of the turbulizer position on the SWBLI. The roughness sample # 6 providing rapid turbulization flow was chosen (denoted by diamond in the Fig. 6). Altogether 7 locations were investigated $X = 15$, 50, 85, 100, 110, 117, 124 mm (arrow in Fig. 6 indicates increase of distances). For all positions of the turbulizer upstream of separation bubble the SWBLI was typical for the turbulent case and dimensionless parameters were approximately the same. Since the thickness of the inflow turbulent boundary layer decreases with shift of the turbulizer downstream, the dimensional parameters also decreased. When turbulizer was placed at the beginning of the interaction zone H_{per}/δ^* decreased to 30. And the flow pattern was very similar to the case obtained with the roughness #3. Perhaps in this case we observed the similar processes. When the turbulizer #6 was in location

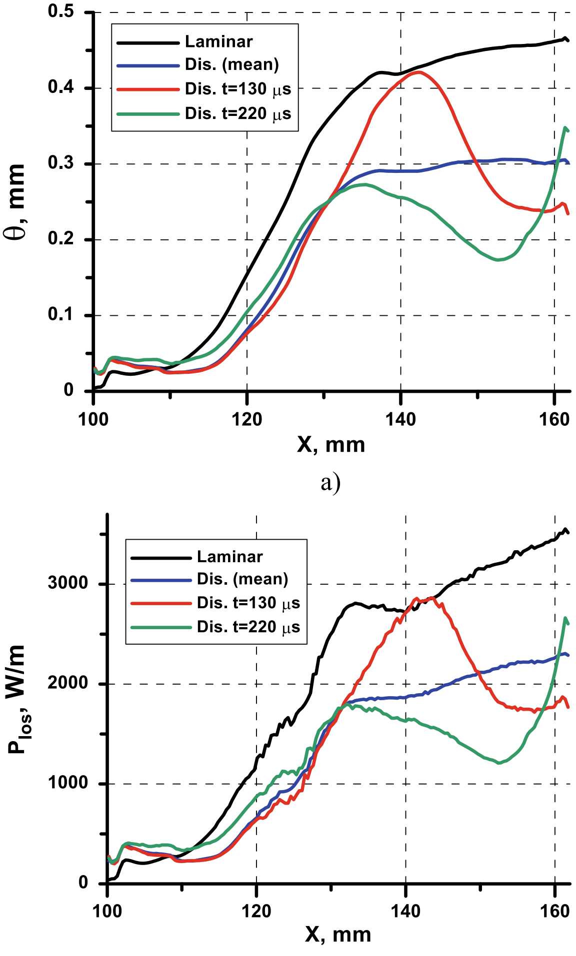

a)

b)

Fig. 13 BL characteristics **a** momentum thickness and **b** energy losses along SWBLI (E_{dis}= 0.7 mJ, $\beta = 4°$)

near the SWBLI it was not able to provide the complete turbulization of the boundary layer. But it introduced significant perturbations which quickly grew in the interaction zone and resulting to turbulization of the flow in SWBLI.

In Fig. 7 one can see the effect of the some type of turbulators on momentum thickness. The momentum thickness distributions obtained for the turbulators, which do not cause immediate laminar-turbulent transition upstream of the interaction zone, are more or less similar to the laminar case. The momentum thickness for the natural laminar case at the end of the measurement area is close to the turbulent regime #5 but with higher level of pulsations. Taking into account the results obtained in

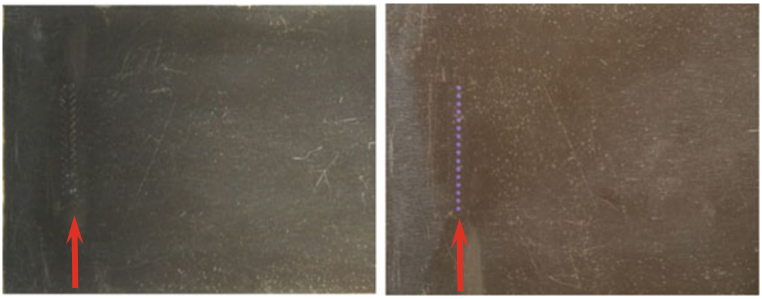
a) - “ZZ” tape b) - Cadcut

Fig. 14 Turbulator devices mounted on the flat plate

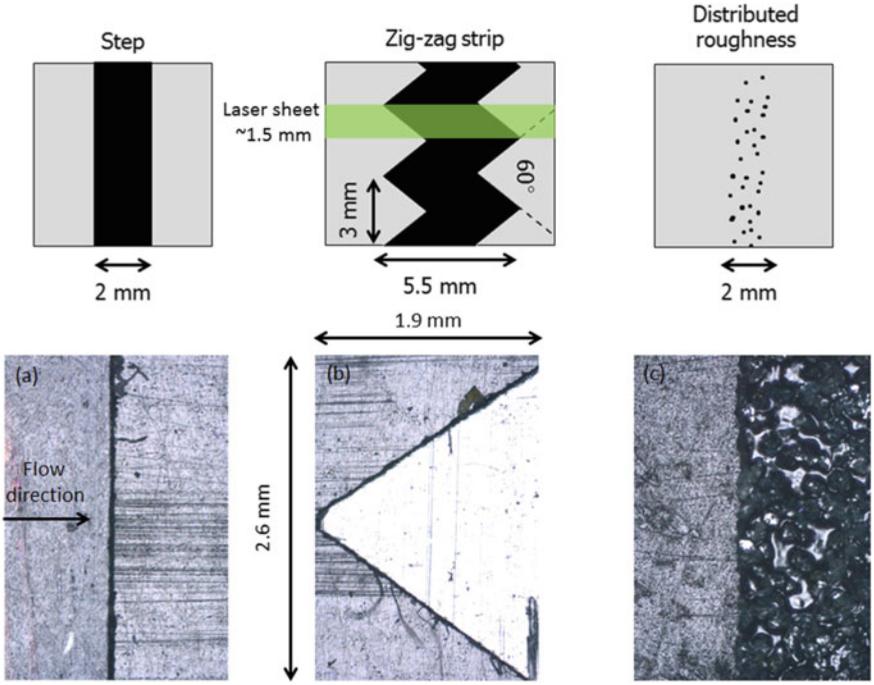

Fig. 15 Schematic representation of the tripping devices (top) and tripping devices imaged with a confocal microscope (bottom); **a** step **b** zig-zag tooth **c** distributed roughness

Chap. 2, it can be concluded that the turbulators did not allow to improve the flow in the SWBLI zone.

1.2.2 Active Flow Control Device

The plasma control devices were studied in the experiments. The spark discharge (SD) was chosen among others to achieve high concentrations of the energy in the plasma region. The model with installed SD actuator in shown in Fig. 8. It has ceramic insert made from MACOR holding a line of flush mounted electrodes. The electrodes are placed at distance 93 mm from the leading edge. There are three pairs of the electrodes with discharge gaps of 4.5 mm. Distance between the neighbor electrode pairs is 14.5 mm. All tree discharge gaps are connected in-series. The capacitors connecting the interim electrodes to the ground were used to assist the breakdown (Fig. 9).

Spark discharge actuator was fed by high voltage source using two transformers DAEHAN 15000 V/30 mA. The self-adapting scheme was used including a battery of capacitors C1 connected in parallel to the actuator (Fig. 9). This capacity is charged up to discharge level and consequently discharges. This process is periodic and the period depends on the environmental conditions and total capacity. Therefore the discharge repetition process is self-regulated and the frequency is not perfectly stable. In the following discussion this frequency is deduced as $f = 1/T$ where T is averaged period of the discharges.

PIV measurements were synchronized with plasma discharge using time delay unit. The duration of the current pulse in the spark was less than 1 μs (Fig. 8b) and average power for one discharge gap was estimated as $P_{dis} = 11$ W. Figure 7 shows pulse energy and frequency for several values of capacity C1.

The PIV data obtained for pulse energy of $E_{dis} = 0.7$ mJ ($f = 18.2$ kHz), $\beta = 4°$ are shown in Fig. 11 as the velocity fields corresponding to various discharge phases. High average frequency of the discharge means that the flow disturbances produced by the sparks travel downstream with small distance between them ($\approx$15–20 mm). Since the high voltage system is self-regulated the breakdowns are not perfectly periodical. In the experiments PIV system was triggered by a discharge and the traces of the preceding discharges present in each single velocity distribution. However in the averaged data shown in Fig. 11 one can see only trace of the triggering breakdown since the delay between the sparks is not perfectly constant.

At the moment $\Delta t = 100$ μs the disturbance generated by the discharge passes the interaction. It can be seen that the compression waves upstream of the interaction are concentrated close to the interaction and they are more intense in comparison with the reference laminar case. This is evidence of diminishing or disappearance of the laminar separation zone upstream of the interaction. This is similar to the turbulent test case but the reflected shock wave is weaker. Fullness of the velocity profiles increases in the interaction and downstream.

The disturbance is represented by the area of low velocity in the boundary layer due to the hot spot with low density and high temperature. Decrease of velocity in this spot is amplified when it goes through the shock wave because of changes of the shocks configuration induced by the spot.

Figure 12 presents the comparison of laminar and turbulent (artificial turbulization, zig-zag trigger in position of $X = 100$ mm) test cases and cases with discharge excitation with various power. It can be seen that discharge actuator allows to achieve less intensive shock wave and slow growth of the wake. The best result was obtained for the lower value of spark energy.

Variation of the momentum thickness for the case of $E_{dis} = 0.7$ mJ, $\beta = 4°$ is presented in Fig. 13. It can be seen that the spark discharge is able to reduce the average momentum thickness in the wake by 30% in comparison with laminar case.

Comparison of the averaged θ distribution with instantaneous ones presented in the same figure shows that in the region of the hot spot there is increase of losses. Therefore the positive effect of the disturbances provided by the discharge may be eliminated by the hot spot.

The flow control efficiency may be estimated basing on θ value at the end of measurement region as $\eta_{dis} = 0.5\rho U^3(\theta_{lam} - \theta_{dis})/P_{dis}$. For $\beta = 4°$ the maximum value of efficiency η_{dis}= 225% was obtained for minimum spark energy $E_{dis} =$ 0.7 mJ. If the spark energy was increased up to $E_{dis} = 1.3$ mJ the efficiency dropped to 167%. Increase of spark energy **up to 3 mJ resulted in negative efficiency −55%. This means that the disturbance** generated by the spark is sufficient but there in negative effect provided by the hot spot increasing with the power. This conclusion agrees with results of computational study [1] where some optimum of pulse energy was found for the flow turbulization by a discharge. In the case of exceed of energy the effect diminishes due to heat spot formation. Since the flow parameters of study [1] and the presented experiments are close it can be assumed that decrease of energy by factor of 10 will allow to keep positive effect and increase the control efficiency.

1.2.3 Conclusions

Spark discharge actuators were tested and found to be effective to excite powerful periodic disturbances and control the interaction region. Basing on the quantitative analysis it may be concluded that spark discharge actuator improves the average flow in the interaction region. It was found that for all studied parameters of the discharge the pulse energy was sufficient for the generation of a turbulent spot and the suppression of the separation zone. However increasing of the discharge power leads to formation of the powerful hot spot which results in higher losses in the boundary layer. The analysis shows that active flow control may be more effective in comparison with passive control by the roughness.

1.3 ONERA-DAFE

1.3.1 Selected Configuration

A configuration has been retained for testing several control devices on the transition process, but also for related CFD simulations (RANS and LES) and flow stability analysis. In this configuration, the flat plate is located at $Z = 40$ mm from the test section lower wall to avoid blockage effect under the plate and at $X = -11.45$ mm into the Mach number rhombus ($X = 0$ is corresponding to the nozzle exit plane, see Fig. 36 and Table 5, chapter “WP-1 Reference Cases of Laminar and Turbulent Interactions”) to avoid perturbation from the reflection of the Mach wave emanating from the plate leading edge (P3 position). The angle of attack α of the shock generator wedge is chosen equal to 2.5° to produce a moderate shock intensity. For this selected configuration, the laminar boundary layer separates and the transition process appears into the viscous interaction domain.

1.3.2 Control Devices Under Study

Several parameters are tested in order to optimize the effectiveness of control devices on the boundary layer transition, namely:

- Two types of 3-D turbulator device: a Cadcut device and a “ZZ” tape with a width of 6 mm (see Fig. 14).
- The height of device: the “ZZ” tape has two different heights h, 100 and 200 μm (called ZZ100 and ZZ200), leading to the Reynolds number values Re_h based on these heights respectively equal to 1400 and 2800; for comparison purpose, the height of the Cadcut device is chosen equal to 102 μm. These values are scaled to the compressible displacement thickness of the incoming boundary layer obtained by calculation (equal to 130 μm at 30 mm from the flat plate leading edge).
- The location of device with respect to the flat plate leading edge: the “ZZ” tape is located far upstream of the “averaged” natural (without the shock-wave) boundary layer transition position, but also upstream of the boundary layer separation region; then, two locations are selected, respectively at: $17 \leq X_{d1}$ (mm) ≤ 23 and at: $24 \leq X_{d2}$ (mm) ≤ 30 (corresponding to $\mathrm{Re}_{xd} \approx 280{,}000$ and 380,000).

1.4 TUD

The basic test setup used for the study of the transition control devices is identical to that described in Sect. 2.3a and consists of a full-span flat plate and a symmetric partial-span shock generator, see [2] for more information. Earlier studies showed that the flat plate boundary layer remains laminar up to 55 mm from the leading edge

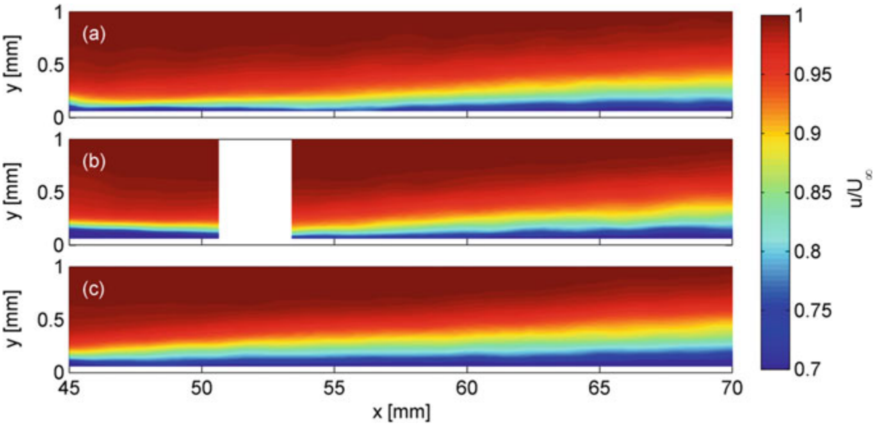

Fig. 16 Streamwise component of the velocity field downstream of the transition control devices. **a** zig-zag strip **b** step **c** distributed roughness patch

($Re_{x,tr} = 1.9 \cdot 10^6$). Natural transition takes place over a length of 35 mm and a fully turbulent boundary layer is established at approximately $x_{\text{turb}} = 90$ mm ($Re_{x,turb} = 3.2 \cdot 10^6$). In the SWBLI experiments the shock generator was set to a flow deflection angle of 3°, resulting in a theoretical (inviscid) pressure rise over the interaction of $p_3/p_1 = 1.35$.

The tripping devices were placed in the laminar regime of the boundary layer, at $x_{\text{trip}} = 40$ mm from the leading edge ($Re_{x,trip} = 1.4 \cdot 10^6$). The boundary layer at this location has been documented in Sect. 2.3b. Three types of tripping devices were investigated: a step-wise strip, a patch of distributed roughness (carborundum) and a zig-zag strip. Figure 15 shows a schematic representation of the trips and Fig. 16 shows the details of the trips as imaged with a confocal microscope. The devices spanned the entire plate width and had a roughness height of $k = 0.1$ mm, which corresponds to $Re_k = U_\infty k/\nu_\infty = 3.5 \cdot 10^3$ or $Re_{kk} = U_k k/\nu_k = 1.4 \cdot 10^3$. These values may be compared to the experimental study on tripping wires in supersonic flow [3], which delivers a critical $Re_k = 2.1 \cdot 10^3$ (equivalent $k = 0.06$ mm) for the present measurement conditions. It is therefore to be expected that the $k = 0.1$ mm trips introduce boundary layer transition in close proximity to the trip.

The velocity field downstream of the tripping devices is presented in Fig. 16 for the zig-zag strip (a), step (b) and distributed roughness patch (c). Velocity field data is missing for the step in the region from 50.6 to 53.4 mm due to a failed measurement (the incoming boundary layer was already transitional), but for all other datasets it has been confirmed that the incoming boundary layer is laminar. To provide more insight in the flow field downstream of the tripping devices, velocity profiles were extracted at x = 45, 50 and 55 mm (Fig. 17). The trips were centered around x = 40 mm and the trip to measurement station distance for Figs. 17a–c therefore equals 5, 10 and 15 mm, respectively. Or equivalently: 25, 50 and 75 undisturbed boundary layer thicknesses δ_{95} downstream of the centre of the trip.

Fig. 17 Velocity profiles at x = 45 mm (**a**); 50 mm (**b**) and 55 mm (**c**)

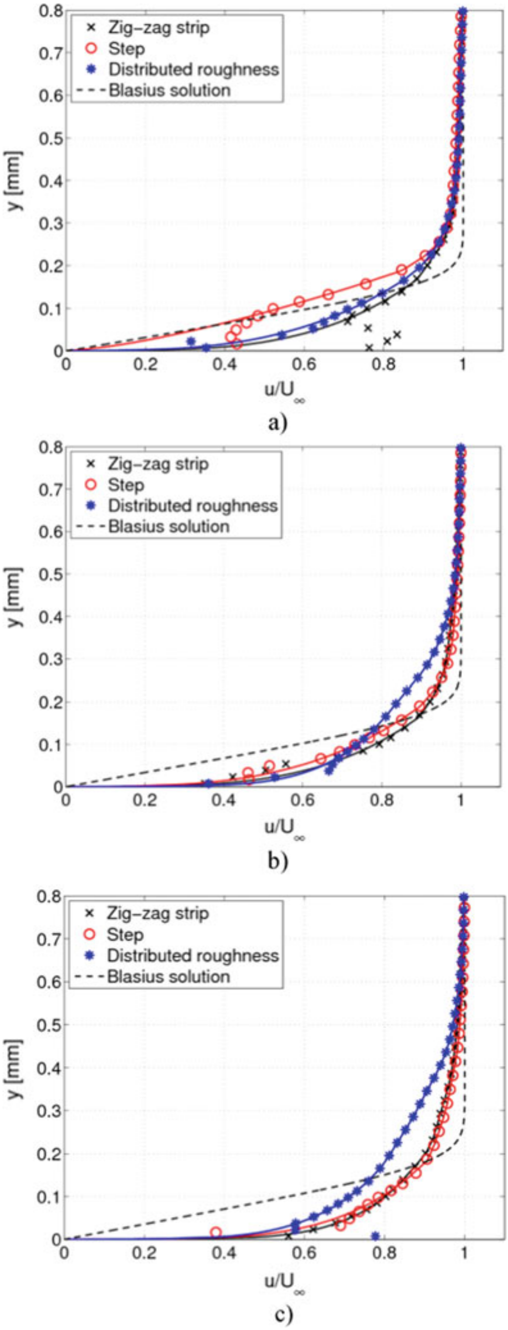

The laminar boundary layer upstream of the tripping devices is lacking seeding in the near-wall region ($y < 0.1$ mm) of the flow. The boundary layer undergoes transition when crossing the trips, and due to the increased turbulent mixing the seeding conditions are found to improve gradually when moving downstream from the trip. For the first measurement station ($x = 45$ mm) it is however still difficult to accurately determine the velocity field in the near-wall region of the flow and some outliers may be observed in the data close to the wall. In order to calculate the integral boundary layer parameters from the experimental data it is therefore necessary to extrapolate the data towards the wall. The power law fit used for this purpose is indicated in the graphs.

At $x = 45$ mm (Fig. 38, chapter "WP-1 Reference Cases of Laminar and Turbulent Interactions") one may observe that the boundary layer displays a turbulent character for both the zig-zag strip and the distributed roughness, whereas for the case of the step the boundary layer is closer to a laminar profile. This difference disappears further downstream ($x = 50$ and 55 mm) and at these locations the boundary layer is turbulent for all trips, where it may be interesting to notice that the distributed roughness results in a substantially thicker boundary layer than the zig-zag strip and the step.

These observations are reflected in Fig. 18, which displays the development of the integral boundary layer parameters. For the computation of these properties, a power-law fit is used for the velocity data points close to the wall. The initial stage of the zig-zag strip and the step is different, but eventually both result in a turbulent boundary layer with approximately the same displacement and momentum thickness. The distributed roughness on the other hand results in a substantially thicker turbulent boundary layer compared to the other two tripping devices (displacement thickness is about 10 μm larger and momentum thickness about 8 μm larger). The scale on the right-hand side of the graphs indicates the development of δ_i^* and θ_i as a ratio of the undisturbed (laminar) values ($\delta_{i,0}^*$ and $\theta_{i,0}$) measured at the location of the trip. The displacement thickness temporarily becomes smaller than its undisturbed value due to the process of transition, which fills up the boundary layer profile. On the other hand, the momentum thickness downstream of the trip is always larger than its undisturbed value.

Finally, the shape factor development clearly shows that the zig-zag strip and the distributed roughness patch deliver a turbulent boundary layer much closer to the trip than the step. A shape factor of 1.4 is reached approximately 6 mm downstream of the centreline of the zig-zag strip and the distributed roughness patch. The same value is reached only after approximately 11 mm for the step. This implies that for the same degree of effectiveness the step should be placed further upstream of an impinging shock wave than the other two tripping devices.

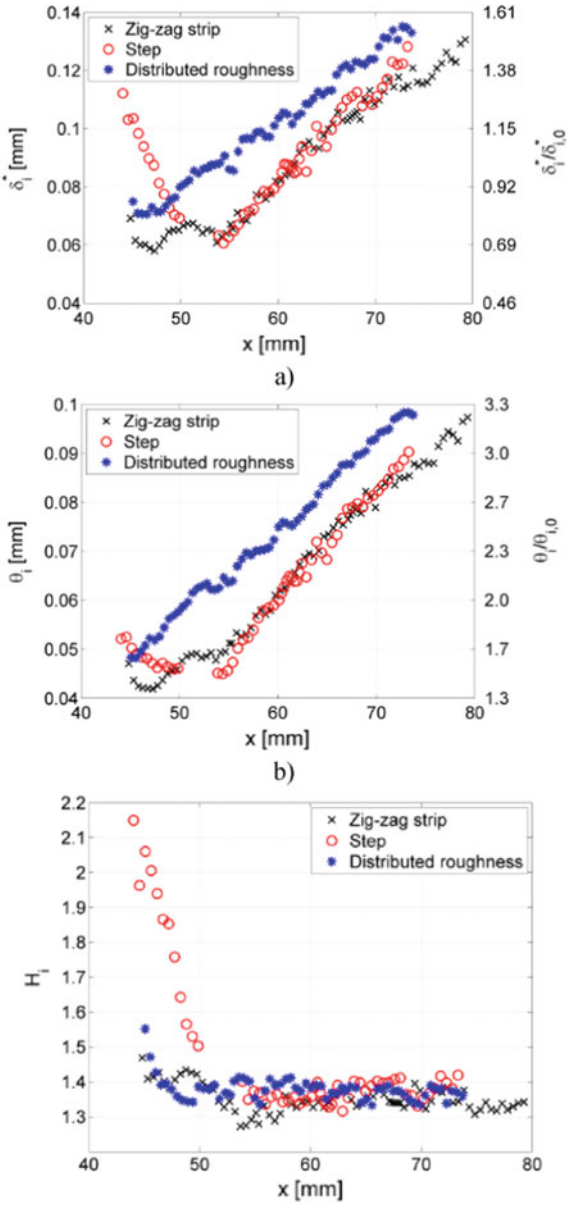

Fig. 18 Development of the boundary layer properties downstream of the tripping devices: **a** incompressible displacement thickness δ_i^*, **b** incompressible momentum thickness θ_i; **c** incompressible shape factor H_i

1.5 SOTON

1.5.1 Non-thermal Plasma Modelling

A linearised electric body force is used to model the effect of a non-thermal plasma flow control device [4]. The objective is to obtain a simplified representation of the body forces induced by the plasma actuator on the fluid without directly computing the electric field distribution. The Navier-Stokes equations, inclusive of the electrical body forces, become:

$$\frac{\partial \rho}{\partial t} + \frac{\partial\left(\rho u_j\right)}{\partial x_j} = 0 \tag{1}$$

$$\frac{\partial \rho u_i}{\partial t} + \frac{\partial \rho u_i u_j}{\partial x_j} = -\frac{\partial \rho}{\partial x_i} + \frac{1}{\mathrm{Re}}\frac{\partial \tau_{ij}}{\partial x_j} + D_c \bar{F}_i \tag{2}$$

$$\frac{\partial E_t}{\partial t} + \frac{\partial (E_t + p) u_j}{\partial x_j} = \frac{1}{\mathrm{Re}}\frac{\partial u_i \tau_{ij}}{\partial x_j} - \frac{1}{(\gamma - 1)\mathrm{Re}\,\mathrm{Pr}\, M^2 \partial x_j}\left[\kappa \frac{\partial t}{\partial x_j}\right] + D_c u_i \bar{F}_i \tag{3}$$

Apart from the usual notation, ρ_c is the dimensionless charge density and E_i (i = 1, 2, 3) are the three electric field components in the streamwise, wall-normal and spanwise directions, respectively. An alternative notation for the electric field distribution is $E = (E_x, E_y, E_z)$. The dimensionless parameter D_c is the ratio between electrical and inertial forces and can be expressed as

$$D_c = \frac{\rho^*_{c,ref} e^*_c E^*_{ref} \partial^*_{1,0}}{\rho^*_\infty {U^*_\infty}^2} \tag{4}$$

where $\rho^*_{c,ref}$ is the reference charge density, e^*_c is the electronic charge and E_{ref} is the reference electric field. The first modelling step is to linearise the distribution of the electric field that is mainly concentrated in the vicinity of the cathode and decreases in intensity moving downstream over the anode and away from the wall.

The electric field distribution can therefore be confined within a triangular region (in light blue) as schematically represented in Fig. 19.

The variation in space of the intensity of the electric field can be simplified as

$$|\boldsymbol{E}(x, y)| = E_0 - k_1 (x - x_E) - k_2 \gamma \tag{5}$$

with V the applied voltage and d the distance between cathode and anode in the streamwise direction. The electric field equals the breakdown electric field strength E_b at the boundary of the triangular region, allowing the constants k_1 and k_2 to be calculated as

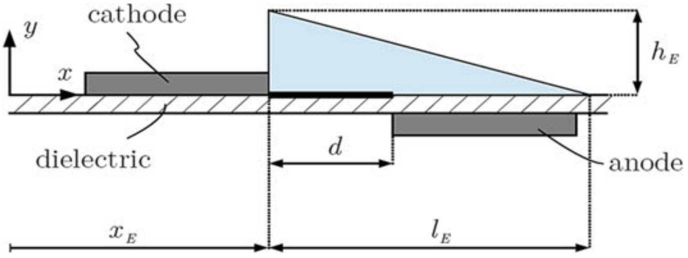

Fig. 19 Linearisation of the electric field

$$k_1 = \frac{E_0 - E_b}{l_E} \text{ and } k_2 = \frac{E_0 - E_b}{h_E} \tag{6}$$

where l_E and h_E are the streamwise length and wall-normal height of the linearised electric field distribution, respectively. Thus, the components of the electric field distribution (E_x, E_y) can be described as

$$\boldsymbol{E}(x, y) = |\boldsymbol{E}(x, y)| \left(\frac{k_2}{\sqrt{k_1^2 + k_2^2}}, \frac{k_1}{\sqrt{k_1^2 + k_2^2}}, 0 \right) = \left(E_x, E_y, 0\right) \tag{7}$$

Since the DBD is uniform in the spanwise direction, $E_z = 0$. In this way, it is possible to obtain the body forces (f_x, f_y) that are applied by the charged particles of the plasma to the neutral particles of the fluid as the parameter α is the collision efficiency and for simplicity can be set to unity [4], while the charge density ρ_c is assumed to be constant in the plasma region. The function δ ensures that the body forces are active only in the linearised-triangular region where the plasma is present and can be described as

$$f_x = \alpha E_x \rho_c e_c \delta \text{ and } f_y = \alpha E_y \rho_c e_c \delta \tag{8}$$

Although in the AC cycle during which the voltage is applied the plasma discharge happens only in a small fraction of time Δt, the frequencies of discharge are high under high applied voltage frequency and it is therefore possible to apply the averaged forces continuously over the whole cycle. The time-averaged body forces (F_x, F_y) can finally be written as

$$\delta = \begin{cases} 1, & |\boldsymbol{E}| \geq E_b \\ 0, & |\boldsymbol{E}| < E_b \end{cases} \tag{9}$$

where F_{ac} is the frequency of applied voltage. Although the real applied voltage has an unsteady nature, it is important to specify that this approach yields a steady representation of the actuator and its effects on the fluid. In addition, the cathode is assumed to have an infinitely small thickness in order to avoid the introduction of a surface step. The drawback to this simplified approach is the requirement of several input values that need to be specified from available experimental data. On the other hand, it avoids solving the Boltzmann and transport equations (per number of species, depending on the plasma chemistry) for electric field and species energy distributions that are typically computationally very expensive. For all simulations with plasma actuation the input parameters used here are taken from the experiments cited in [4].

$$\overline{F}_x = F_{ac} f_x \Delta t \text{ and } \overline{F}_y = F_{ac} f_y \Delta t \tag{10}$$

1.5.2 Thrust Direction, Unsteady Actuation and Spanwise Treatment

The general idea is to use the plasma actuator to force specific unstable modes of the boundary-layer, working as a transition tripping device. This can be done by changing the preferred direction of the electrical forces and applying a time and/or span variation to the body forces as described below:

- Thrust Direction: The effect of the DBD can be either flow-wise or flow-opposing, resulting in a “co-flow” or “counter-flow” actuation, respectively. Thus, the preferred thrust direction changes and momentum is either added to or subtracted from the boundary-layer.

  Unsteady Actuation and Spanwise Treatment: Linear stability theory provides frequencies and spanwise wavenumbers (ω, β) of the most unstable modes that can be used to apply a time and span modulation to the electrical body forces F_i as

$$F_i^{unsteady} = F_i^{steady} \cdot \left[1 + \sin\left(\beta_{pl} z\right)\right] \cdot \left[1 + \sin\left(-\omega_{pl} t\right)\right] \tag{11}$$

  where a factor of unity is added to the sine variation to avoid changes of sign in the body forces and provide the same amount of momentum input. The span variation of the body forces should not be confused with the spanwise shape of the electrodes. This model assumes that the electrodes are straight-edged elements (Fig. 20a) and the spanwise component of the electric field is equal to zero ($E_z = 0$). However, spanwise components of the electric field can be added in “serpentine” and “horseshoe” configurations (Fig. 20b, c), as suggested by [5].

In the current contribution, the effect of spanwise electric field components is investigated by modifying Eq. 2.8 to

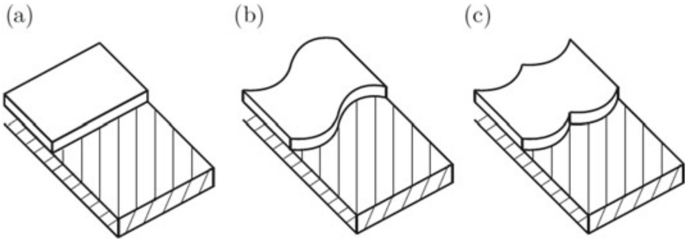

Fig. 20 DBD spanwise shapes for straight-edged (**a**), serpentine (**b**) and horseshoe (**c**) configurations

Fig. 21 Electric field spanwise component for co-flow serpentine (**a**) and horseshoe (**b**) configurations

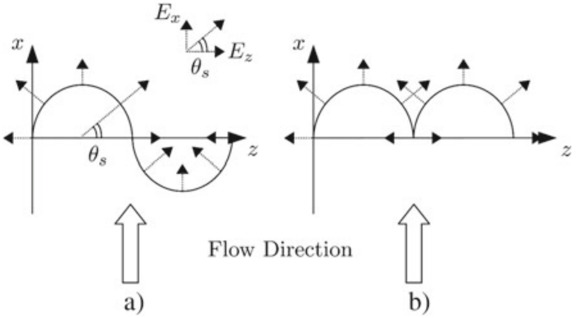

$$\boldsymbol{E}(x,y,z)=|\boldsymbol{E}(x,y,z)|\left(\frac{k_2}{\sqrt{k_1^2+k_2^2}}\sin\theta_S,\ \frac{k_1}{\sqrt{k_1^2+k_2^2}},\ \frac{k_2}{\sqrt{k_1^2+k_2^2}}\sin\theta_S\right)\quad(12)$$

where θ’s is the angle between the spanwise direction and the electric field direction on a generic x-z plane (as shown in Fig. 21a, b for the case of co-flow serpentine and horseshoe actuations, respectively).

1.5.3 Attached Boundary-Layer

Several DNS simulations are carried out to verify the effectiveness of a non-thermal plasma DBD as a flow control device. Different actuation configurations are tested with the intention of accelerating the transition to turbulence first in an attached zero-pressure gradient boundary-layer.

Inflow conditions, domain size and grid resolution are presented in Table 2. The domain height could not be reduced any further since a Mach wave is generated at the plasma location and its weak reflection from the domain top boundary needs to fall outside the numerical domain. The grid resolution is $(N_x, N_y, N_z) = (1680, 144, 240)$, corresponding to a grid size in wall units (when transition occurs) equal to $\left(\Delta x^+, \Delta y_w^+, \Delta z^+\right) = (5, 0.98, 5)$. The input parameters of the DBD plasma device

Table 2 Numerical setup for the zero-pressure gradient case

M	1.5
$\delta^*_{1,0}$	0.00075
$\mathrm{Re}_{\delta^*_{1,0}}$	75.00
T^*_∞	202.17
$L_x \times L_y \times L_z$	310 × 115 × 27.32
$N_x \times N_y \times N_z$	168 × 144 × 240
$\Delta x^+ \times \Delta y^+_w \times \Delta z^+$	4 × 0.85 × 4

are taken from the experiments used in Shyy et al. [4] (as described in Sect. 2) and give a dimensionless parameter $\mathrm{D_c} = 1.75 \times 10^{-5}$ (applied voltage of 5 kV). The plasma actuator has an upstream effect on the boundary-layer, therefore the DBD is placed at $\mathrm{Re_x} = 1.25 \times 10^5$ in order to allow the boundary-layer to follow the laminar skin-friction solution for about 30 $\delta_{\mathrm{i,0}}$ upstream of the actuation location. Another important detail of the numerical setup is how the electric field distribution changes depending on the direction of the actuation. For all the cases with counter-flow actuation the electric field distribution is mirrored with respect to a vertical axis. All simulations presented here use unsteady plasma actuation with frequency equal to the most unstable modes predicted by LST (i.e. $\omega_{\mathrm{pl}} = 0.1011$). The effects of the electric field spanwise treatment are also investigated. First, a spanwise variation of the electric field is applied according to the spanwise wavenumber of the most unstable mode predicted by LST ($\beta_{\mathrm{pl}} = 0.23$) and compared to an actuation with no spanwise variation (i.e. $\beta_{\mathrm{pl}} = 0$). For these cases, the electric field spanwise component (and related body-force) is zero. Secondly, different spanwise shapes of the dielectrics, such as straight-edged, serpentine and horseshoe, are used to study the effects of a spanwise component $\mathrm{E_z}$ of the electric field on the tripping. When the serpentine or horseshoe configurations are used, no additional spanwise modulation of the electric field distribution is introduced ($\beta_{\mathrm{pl}} = 0$).

1.5.4 Plasma Regions Size

Regardless of the flow speed, higher plasma induced velocities can be directly translated into a more effective actuation. The highest induced velocities are typically no larger than 8–10 m/s [6]. For low subsonic flows, these values have been demonstrated to be high enough to obtain drag and separation reduction as well as turbulence tripping, but for supersonic applications this might no longer be true. As shown by [7], depending on the value of the applied voltage the size of the ionised region and induced velocities change accordingly. It is therefore important to reproduce the size of the plasma and the induced velocity field accurately. However, due to the lack of experimental data at M = 1.5, the size of the ionised flow is currently unknown. For this reason, the effect of the plasma region size on the induced velocity flow field is

Table 3 Induced flow velocity summary for plasma size investigation. Counter-flow actuation with straight-edged electrodes and applied voltage of V = 5 kV

(l_E, h_E)(mm)	U^*_{ind}(m/s)	Transition
(3.00, 1.50)	14.1	No
(1.40, 0.30)	0.8	No
(0.07, 0.15)	0.2	No

here studied for counter-flow actuation with a straight-edged electrode and applied voltage of V = 5 kV.

Table 3 summarises the results of this investigation. The first selected plasma size corresponds to the original one from Shyy et al. [4] ($l_E = 3.00$ mm, $h_E = 1.50$ mm) and the results show a value of the maximum induced streamwise velocity of 14.1 m/s. In agreement with the general findings of other researchers who have of U_{ind} found that the modelled induced velocities and body-forces are usually overestimated [8], the value obtained is higher but not significantly different from what modern experimental plasma actuators can achieve. It is important to notice that the height of the plasma region is about 10 times larger than the boundary-layer thickness (δ 99 = 0.15 mm). This means that the actuation is more efficient inside the boundary-layer, but also that part of the energy is lost by doing work on the free-stream. Two other electric field distribution sizes are tested: $l_E = 1.40$ mm, $h_E = 0.30$ mm and $l_E = 0.70$ mm, $h_E = 0.15$ mm, where the latter corresponds to a plasma region whose height is rescaled to fit into the boundary-layer. It can be seen that the induced velocity field decreases when the size of the electric field distribution is decreased. This occurs despite the applied voltage being fixed, which is explained by the fact that the gradient of the linear distribution of the electric field is higher for decreasing plasma sizes. In this way, the region with high body-force intensity becomes concentrated very close to the wall. This study shows that the induced flow is very dependent on the modelled electric field distribution and on the definition of the experimental inputs. An optimisation of the electric field distribution with respect to the boundary-layer thickness could be carried out but it is not in the scope of this work. However, despite the increased induced velocity field, transition is not triggered for any of these configurations. With the intent to efficiently force only the boundary-layer, the size of the plasma region selected for the following investigations is $l_E = 0.70$ mm, $h_E = 0.15$ mm, where the electric field distribution does not extend beyond the boundary-layer thickness.

1.5.5 Induced Velocity Field

A forcing amplitude study is carried out for $D_c = 1.75 \times 10^{-5}$, 4.37×10^{-4} and 4.37×10^{-3}, corresponding to applied voltage rms-values $V_{rms} = 5$, 125 and 1250 kV, respectively. Although technically not feasible, boundary-layer transition only occurs when $U_{ind} \approx 60$ m/s is applied (this will be discussed in more detail in the next section where skin friction distributions are reported). Table 4 summarises for each actuation

Table 4 Induced flow velocity summary for each actuation configuration

Case no.	Direction	V_{rms} (kV)	Span treatment	u	Transition
1	Co-flow	5	$E_z = 0, \beta_{pl} = 0.23$	0.2	No
2	Co-flow	1250	$E_z = 0, \beta_{pl} = 0.23$	48.1	No
3	Counter-flow	5	$E_z = 0, \beta_{pl} = 0.23$	0.2	No
4	Counter-flow	1250	$E_z = 0, \beta_{pl} = 0.23$	53.1	No
5	Counter-low	1250	$E_z = 0, \beta_{pl} = 0.00$	35.5	No
6	Counter-flow	1250	$E_z \neq 0$-Serpentine	58.8	Yes
7	Counter-flow	5	$E_z \neq 0$-Horseshoe	0.2	No
8	Counter-flow	125	$E_z \neq 0$-Horseshoe	8.6	No
9	Counter-flow	1250	$E_z \neq 0$-Horseshoe	59.7	Yes

configuration the maximum induced streamwise velocities (Uind*) and whether transition occurred. Since the cases with low applied voltage did not yield to transition, only the results for $V_{rms} = 1250$ kV will be discussed for this attached boundary-layer (no-shock) case (i.e. cases 2; 4; 5; 6; 9).

Attention is focused first on the effect of the actuation direction (cases 2 and 4). The streamwise velocity profiles at different x-locations around the dielectric region (indicated with an arrow) at $z = L_z/4$ are reported in Fig. 22 for a case without actuation (black circles) and cases with co-flow (blue solid line) and counter-flow (red solid line) actuation. While the profiles upstream of the actuator are undisturbed, the downstream profiles are strongly distorted forwards or backwards for co-flow and counter-flow actuation, respectively. It is also possible to notice at $Re_x \approx 1.75 \times 10^5$

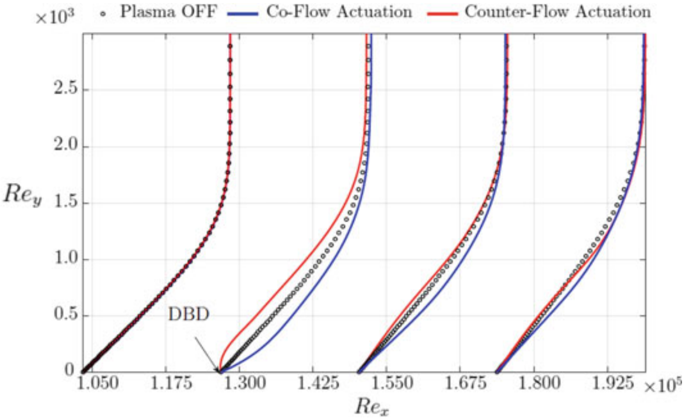

Fig. 22 Streamwise velocity profiles for no-actuation (black circles), co-flow (blue solid line, case 2) and counter-flow (red solid line, case 4) actuations with straight-edged electrodes. The DBD actuator location is indicated by an arrow

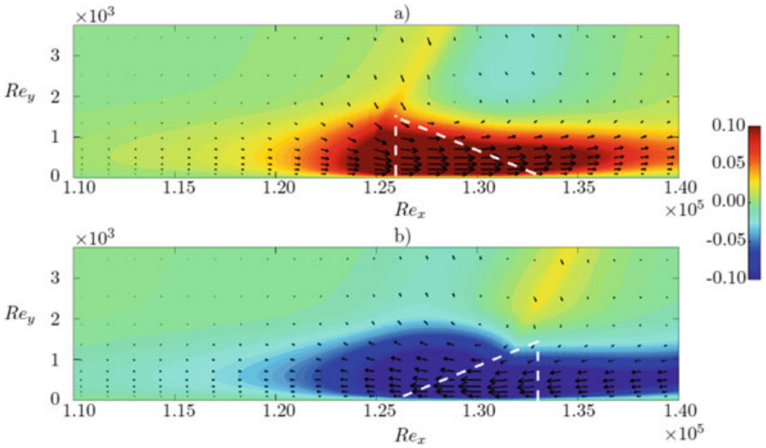

Fig. 23 Induced streamwise velocity vectors superimposed onto the induced streamwise velocity contours on an x-y plane at z = $L_z/4$ for **a** co-flow (case 2) and **b** counter-flow (case 4) actuations with straight-edged electrodes. The DBD position and shape is indicated by the white dashed lines

that the counter-flow actuation is very effective in the creation of a spanwise vortex that will develop downstream.

Induced streamwise velocity vectors are superimposed onto the induced streamwise velocity con tours on an x-y plane at z = $L_z/4$ in Fig. 23, for cases 2 (a) and 4 (b). The white dashed lines indicate the position and shape of the electric field distribution for the co-flow and counter-flow actuations. The preferred direction of the actuation is clearly visible in both cases, along with the generation of the spanwise vortex and a Mach wave above the plasma region.

The same analysis is repeated on an x-z plane at a distance 0.1 $\delta_{1,0}$ off the wall and reported in Fig. 24. Due to the electric field variation in the spanwise direction, a region of high induced velocity in the first half of the domain is created, producing strong tangential forces (the maximum induced streamwise velocities are U^*_{ind} = 48.1 m/s and U^*_{ind} = 53.1 m/s for cases 2 and 4, respectively), compared with the other half that has only a low induced velocity. The resulting wall-normal vortical structure (with opposite sign depending on the direction of the actuation) develops downstream and contributes to destabilising the boundary-layer. When the spanwise variation of the electrical field is removed from the counter-flow actuation (case 5), transition does not occur.

Induced flow fields for an x-y plane at z = $L_z/4$ and an x-z plane at a distance 0.1 $\delta_{1,0}$ off the wall are reported in Fig. 25a, b, respectively. Although the spanwise vortical structure still exists and the induced flow speed is 35.5 m/s, the wall-normal vortex associated with the spanwise variation of the electric field is absent. It is clear that this vortex plays a fundamental role in the destabilisation of the boundary-layer.

The same analysis is done for counter-flow actuation with serpentine (case 6) and horseshoe (case 9) shaped electrodes, with results shown in Figs. 26 and 27. With respect to the flow direction, while the shape of the serpentine electrode is represented

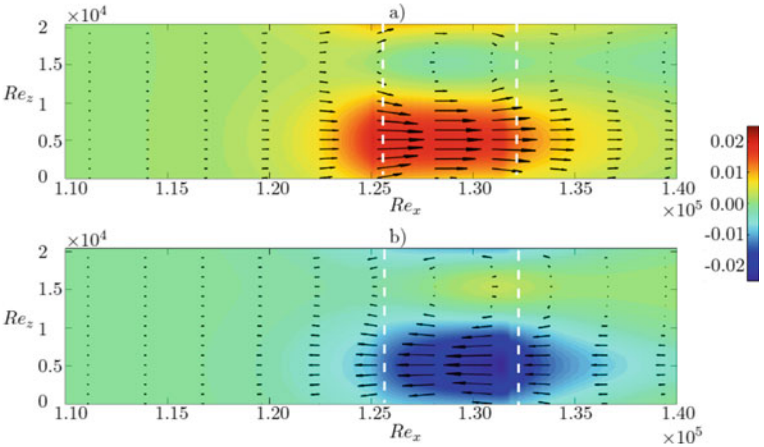

Fig. 24 Induced streamwise velocity vectors superimposed onto the induced stream for **a** co-flow (case 2) and **b** wise velocity contours on an x-z plane at $y = 0.1\ \delta_{1,0}$ counter-flow (case 4) actuations with straight-edged electrodes. The DBD position and shape is indicated by the white dashed lines

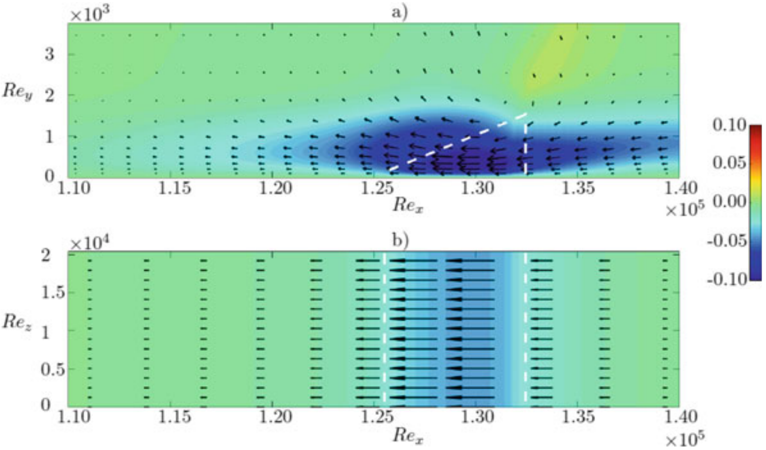

Fig. 25 Induced streamwise velocity vectors superimposed onto the induced streamwise velocity contours on **a** a x-y plane at $z = L_z/4$ and **b** a x-z plane at $y = 0.1\ \delta_{1,0}$ for counter-flow actuation with straight-edged electrodes and no electric field spanwise variation (case 5). The DBD position and shape is indicated by the white dashed lines

by a concave part in $Re_z = (0 - 1) \times 10^4$ and a convex one in $Re_z = (1 - 2) \times 10^4$, the horseshoe configuration consists of two concave regions (see the white dashed lines in Fig. 27).

The introduction of spanwise components of the electric field distribution is beneficial for tripping purposes since both configurations lead to transition. While in the concave portion of the electrode the body forces are all acting towards the centre of

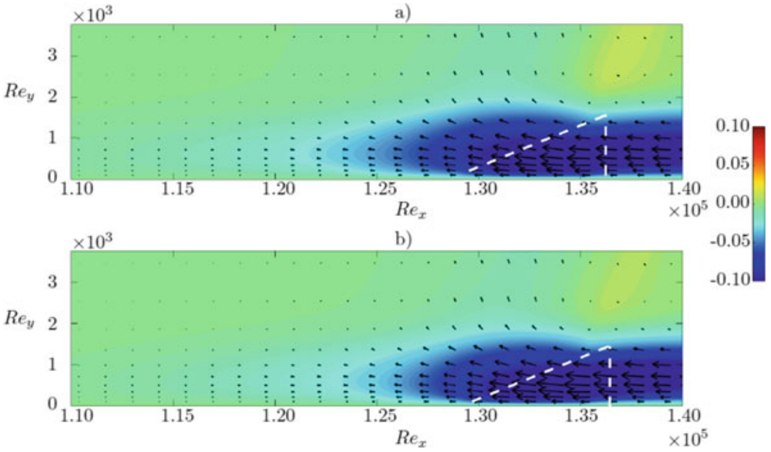

Fig. 26 Induced streamwise velocity vectors superimposed onto the induced stream-wise velocity contours on an x-y plane at z = $L_z/4$ for counter-flow actuation with **a** serpentine (case 6) and **b** horseshoe (case 9) electrodes. The DBD position and shape is indicated by the white dashed lines

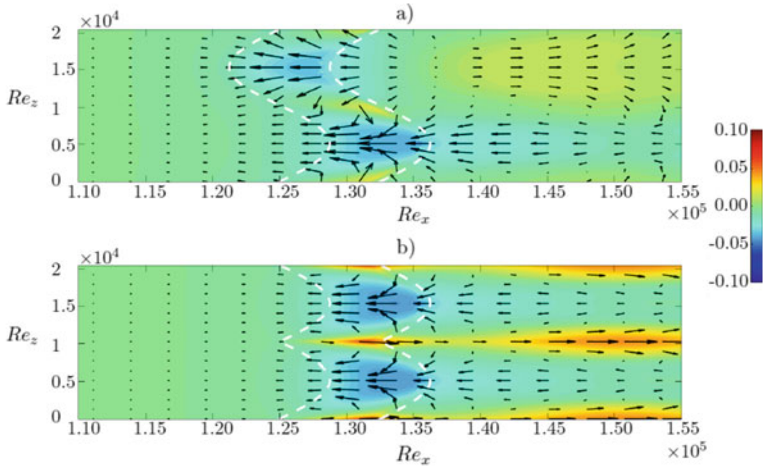

Fig. 27 Induced streamwise velocity vectors superimposed onto the induced streamwise velocity contours on an x-z plane at y = 0.1 $\delta_{1,0}$ for counter-flow actuation with **a** serpentine (case 6) and **b** horseshoe (case 9) electrodes. The DBD position and shape is indicated by the white dashed lines

the portion itself and generate an upward wall-normal jet, in the convex portion the opposite happens and a downward wall-normal jet is produced (Fig. 27a).

The fluid is strongly pulled upstream (or downstream) by the upward (or downward) wall-normal jet, also far downstream of the actuation region. For the horseshoe configuration, high speed streaks are produced at the conjunction of the two concave portions of the electrode and strongly contribute to the transition breakdown process (Fig. 27b).

1.5.6 Skin Friction Distributions

Time and span-averaged skin friction distributions are reported in Fig. 28 for cases 2 (orange solid line), 4 (red solid line), 5 (green solid line), 6 (black solid line) and 9 (blue solid line) along with the laminar (black dashed line) [9] and turbulent (black chain-dotted line) [10] boundary-layer distributions.

The presence of the actuators is shown at $\mathrm{Re}_x = 1.25 \times 10^5$, where spikes in the skin-friction distributions can be seen. Co-flow and counter-flow actuations with straight-edged electrodes (cases 2, 4) do not trigger transition, but it is clear that they both destabilise the boundary-layer and the skin friction distributions deviate from the laminar profile. When the spanwise variation of the electric field distribution is removed (case 5) the skin friction distribution follows the laminar solution, confirming that the generation of wall-normal vortical structure is necessary for a quicker destabilisation of the flow. It is also clear that the spanwise components of the electric field distribution (cases 6 and 9) accelerate the breakdown to turbulence. The generation of wall-normal jets destabilises the boundary-layer very quickly and transition is obtained. The transition scenario is shown in Fig. 29, where skin friction distributions are plotted in the whole wall-plane along with dashed white lines that indicate the position and shape of the electrodes. For straight-edged actuation

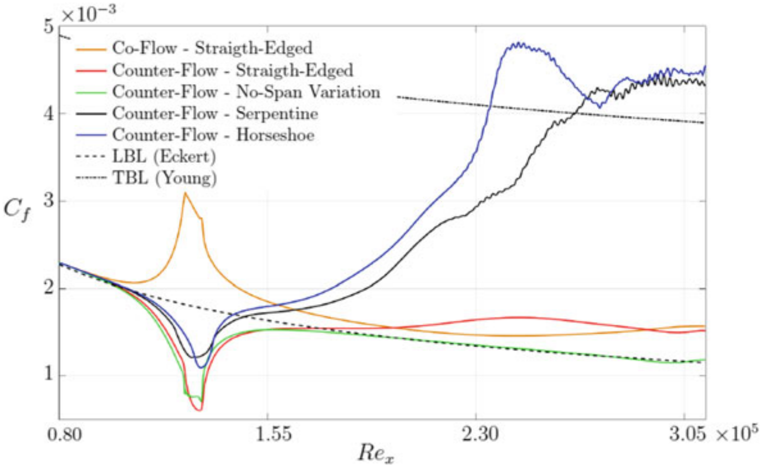

Fig. 28 Time and span-averaged skin friction distributions for different plasma actuation configurations. Cases: 2 (orange solid line), 4 (red solid line), 5 (green solid line), 6 (black solid line) and 9 (blue solid line). Laminar (black dashed line) [9] and turbulent (black chain-dotted line) [10] boundary-layer distributions are also plotted

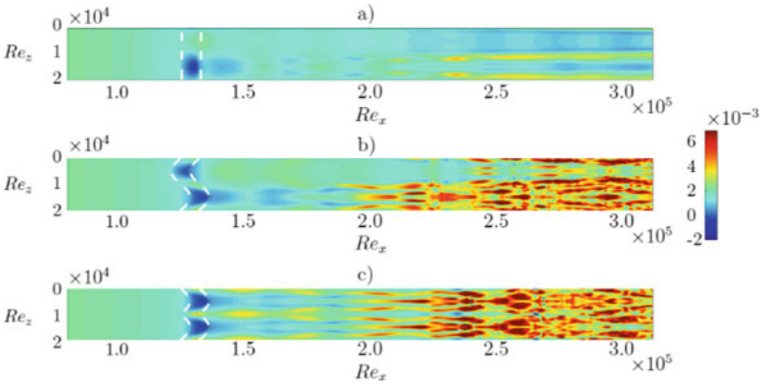

Fig. 29 Skin friction distributions for cases 4 (**a**), 6 (**b**) and 9 (**c**). The DBD position and shape are indicated by the white dashed lines

(Fig. 29a), the destabilisation of the boundary-layer is mainly localised in the portion of the domain where the spanwise variation of the electric field is higher. This suggests that if the actuation amplitude was further increased transition would occur relatively quickly. For the serpentine actuation (Fig. 29b), the breakdown is localised in the portion of domain corresponding to the concave part of the electrode. The body forces that act towards the centre of the electrode portion bring a strong contribution to the breakdown when an upward wall-normal jet is created and the actuator works like an unsteady blowing from the wall. With respect to the horseshoe configuration (Fig. 29c), transition starts at the same streamwise location but the turbulent state is reached further downstream due to this asymmetry. When the symmetry is restored with the horseshoe configuration, the turbulent state is reached earlier.

1.5.7 Transition Visualisation

A streamwise velocity x–y slice at $z = L_z/4$ is reported in Fig. 30 for the no-actuation (a), straight-edged (b), serpentine (c) and horseshoe (d) cases actuated with applied voltage of 1250 kV . For the actuated cases, it is possible to see the presence of vortex roll-ups that precede the breakdown. While for the straight-edged case the boundary-layer becomes unstable but stays laminar, for the serpentine and horseshoe configurations transition occurs at around $Re_x = 2 \times 10^5$.

The iso-surfaces of the Q-criterion for these three cases (Figs. 31, 32 and 33) show that aligned hairpin structures appear, suggesting that secondary instabilities set in and the harmonic or fundamental K-type behaviour precedes the final breakdown to turbulence.

Although the DBD tripping is effective, it is necessary to note once again that this occurs only for very high actuation amplitudes. When the applied voltage from Shyy

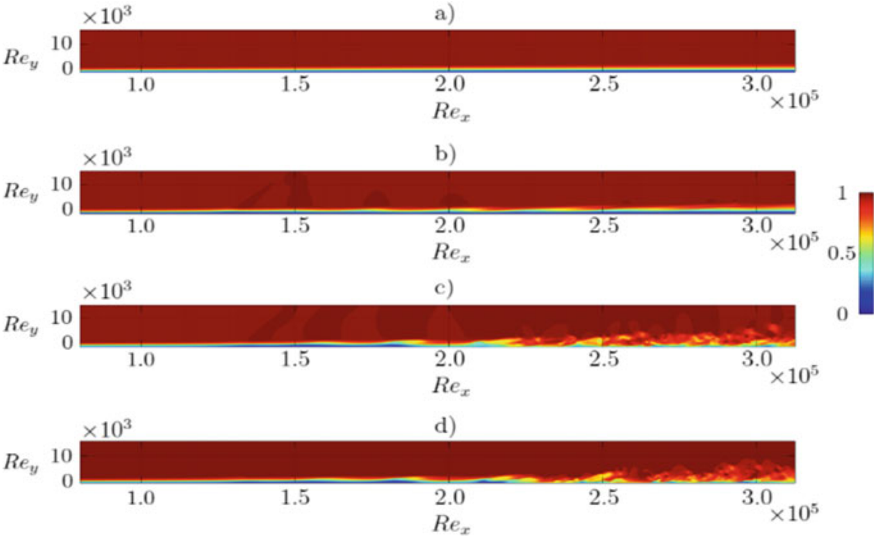

Fig. 30 Streamwise velocity x-y slice at z = L_Z/4 for no-actuation (**a**) and straight-edged (**b**), serpentine (**c**) and horseshoe (**d**) counter-flow actuations

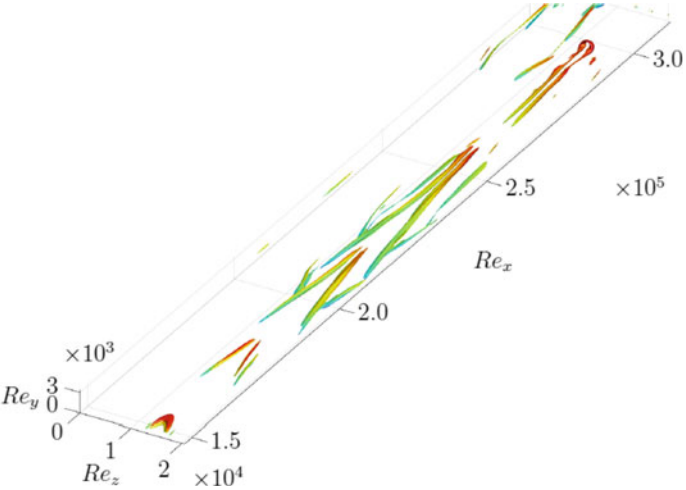

Fig. 31 Iso-surfaces of Q-criterion for straight-edged counter-flow actuation

et al. [4] is used, the plasma-induced velocities are too low to trigger transition and the boundary-layer maintains its laminar state.

This piece of work therefore demonstrates the theoretical potential of plasma actuation for tripping purposes in supersonic flows, but also shows that for real

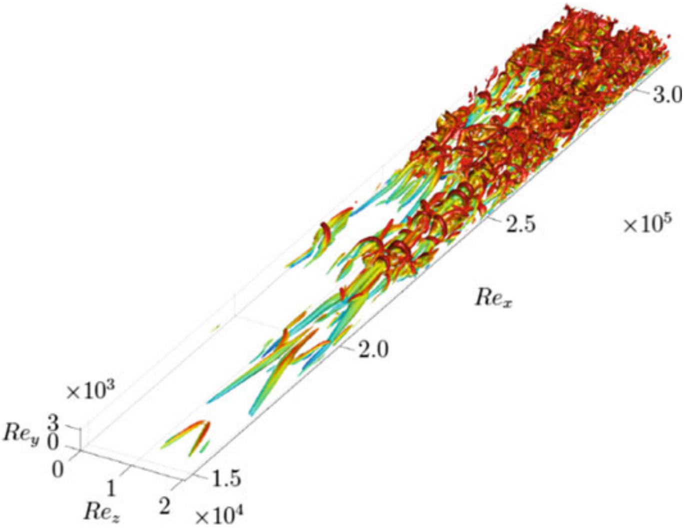

Fig. 32 Iso-surfaces of Q-criterion for serpentine counter-flow actuation

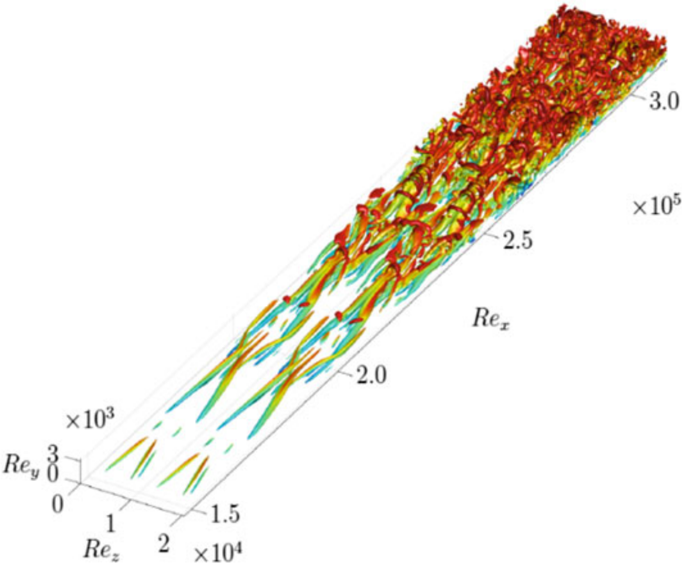

Fig. 33 Iso-surfaces of Q-criterion for horseshoe counter-flow actuation

applications this is not currently feasible since the induced velocities required are 5–10 times larger than those typically achieved in the experiments.

1.6 URMLS

1.6.1 Overview of the Physical Problem and State of the Art

The typical effect of a three-dimensional roughness element on a laminar boundary layer (see the sketch in Fig. 34) is to abruptly shift the transition location upstream with respect to the case of natural transition (i.e. for a smooth surface), with the amount of movement increasing with the roughness height (k). Early experiments [11] suggested that transition is determined by the flow properties of the undisturbed boundary layer evaluated at the edge of the roughness element (hereinafter denoted with the subscript k) through a roughness Reynolds number

$$\mathrm{Re}_k = \rho_k u_k k/\mu_k. \tag{13}$$

While Re_k well identifies the onset of transition in the incompressible regime (i.e. transition is observed when Re_k is greater than a critical value), this parameter cannot account for several effects, including compressibility, roughness shape and

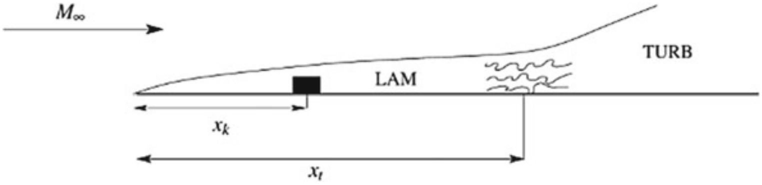

Fig. 34 Sketch of boundary layer transition induced by an isolated roughness element. M_∞ is the Mach number of the (compressible) boundary layer, x_k is the distance of the roughness element by the plate leading edge and x_t indicates the transition location

Fig. 35 Sketch of the computational arrangement used for DNS of transition past the 3D roughness element. The streamwise distance of the obstacle from the inflow station is x_c = 15 δ

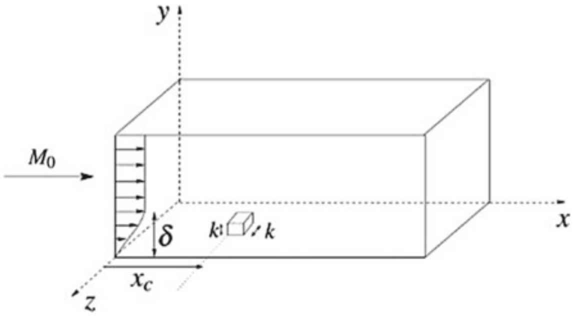

wall temperature. As a consequence, the current prediction of roughness-induced transition at high-speed heavily relies on empirical correlations, a popular one being the Re_θ/M criterion [12].

Past efforts have identified the typical paths to transition, especially in the low-speed regime. Experiments have shown that the flow around an isolated three-dimensional roughness element is characterized by the presence of a steady horseshoe vortex that wraps around the obstacle, with two steady counter-rotating vortices trailing downstream. The streamwise vortices and the associated low-momentum streak lead to a convective shear-layer instability in the wake of the roughness element, characterized by periodic shedding of hairpin-like vortical structures [13, 14]. According to [15], transition occurs when the growth of fluctuations is sufficient to trigger transition, and to penetrate the wall layer.

Recent direct numerical simulations (DNS) [16–17] performed in the supersonic and hypersonic regime indicate that the same scenario observed at low speed also holds at higher Mach numbers, with minor changes due to compressibility. The numerical studies have highlighted the importance of the unstable detached shear layer forming on the top of the roughness element, and have identified the wake behind the roughness element as the primary source for transition.

The activities of URMLS in the project focused on the generation of a DNS database to study the laminar-to-turbulent transition of compressible boundary layers over a flat plate induced by the presence of isolated three-dimensional roughness elements. The initial goal is to widen the range of flow conditions analyzed in literature and understand the effects of the relevant parameters affecting the transition process. The final goal for the WP will be to highlight the effect of different boundary layers states (laminar, transitional and fully turbulent) on the interaction with various shock waves configurations (oblique and normal shock).

1.6.2 Computational Setup and Code Validation

For the purpose of validating the flow solver, we have reproduced the numerical results of [18], who carried out DNS of a laminar boundary layer over a flat plate perturbed by an array of cylindrical roughness elements. The physical parameters for the simulation were selected by those authors to reproduce the experiments of Ergin and White [15], characterized by a roughness Reynolds number $\mathrm{Re}_k = 334$, roughness height $k = 0.332\delta$, cylinder aspect ratio $\mathrm{k/D} = 0.15$ and spanwise spacing between the elements $\lambda_k = 3D$. Since the experiment was conducted at low speed, the Mach number for the simulation, performed with a compressible solver, was set at $\mathrm{M} = 0.1$, which is the same value used here.

A sketch representing our computational arrangement is shown in Fig. 34. The computational domain is a Cartesian box, extending for $L_x = 70\delta$, $L_y = 20\delta$, $L_z = 6\delta$ in the streamwise (x), wall-normal (y) and spanwise (z) directions, where δ, the boundary layer thickness at the inflow station, is chosen as reference length. The grid points have been clustered toward the wall according to a hyperbolic sine mapping

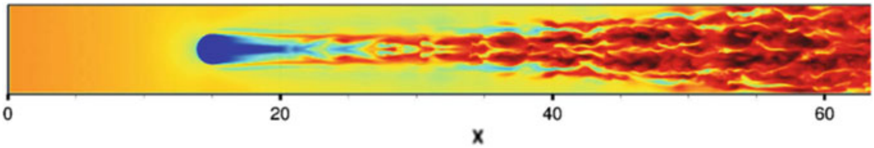

Fig. 36 Contours of the instantaneous streamwise velocity in a wall-parallel plane $y = \mathrm{k}$

function, and non-uniformly distributed in the streamwise and spanwise directions to allow accurate resolution of the region close to the obstacle.

The roughness element, centered at $x_c = 15\delta$, $z_c = L_z/2$, perturbs the laminar boundary layer which develops over the flat plate. The initial condition is determined from a compressible similarity solution, and is also used to prescribe the inflow state. Radiative boundary conditions are assigned at the top and outflow boundaries, and periodicity is enforced in the spanwise direction, implying that the simulated flow mimics that around a periodic array of identical roughness elements.

According to the available experimental and numerical data, at the conditions selected for the validation test, the boundary layer past the roughness element is expected to exhibit bypass transition to a fully turbulent state. This is confirmed in our simulation, as visible in Fig. 36, where contours of the streamwise velocity field are shown in the wall-parallel plane at the edge of the roughness element. The velocity field reveals the presence of a low-momentum streak behind the cylinder, which is perturbed by the passage of an horseshoe vortex system, whose signature is visible in the range $x/\delta = 20$–35. As the flow evolves in the streamwise direction, the flow undergoes transition to a turbulent state, highlighted by the presence of multiple streaks for $x/\delta > 40$.

A quantitative comparison of our data with those of Rizzetta and Visbal [17, 18] is shown in Fig. 37a, where time-averaged velocity profiles are reported at various streamwise stations for the central plane of the computational domain ($z = L_z/2$). Good agreement is found at the various stations, which are representative of the boundary layer streamwise evolution. Additional comparison with the reference DNS data is also shown in Fig. 37b, showing the streamwise evolution of the planar integrated fluctuation energy, defined as

$$\mathrm{e(x)} = \int\int \mathrm{u}_{\mathrm{rms}}^2 \mathrm{dydz} \tag{14}$$

Again, our data are in good agreement with the reference data, predicting the rapid rise of the perturbation energy past the roughness zone, followed by a saturation zone starting at approximately $(x - x_c)/\delta \approx 30$.

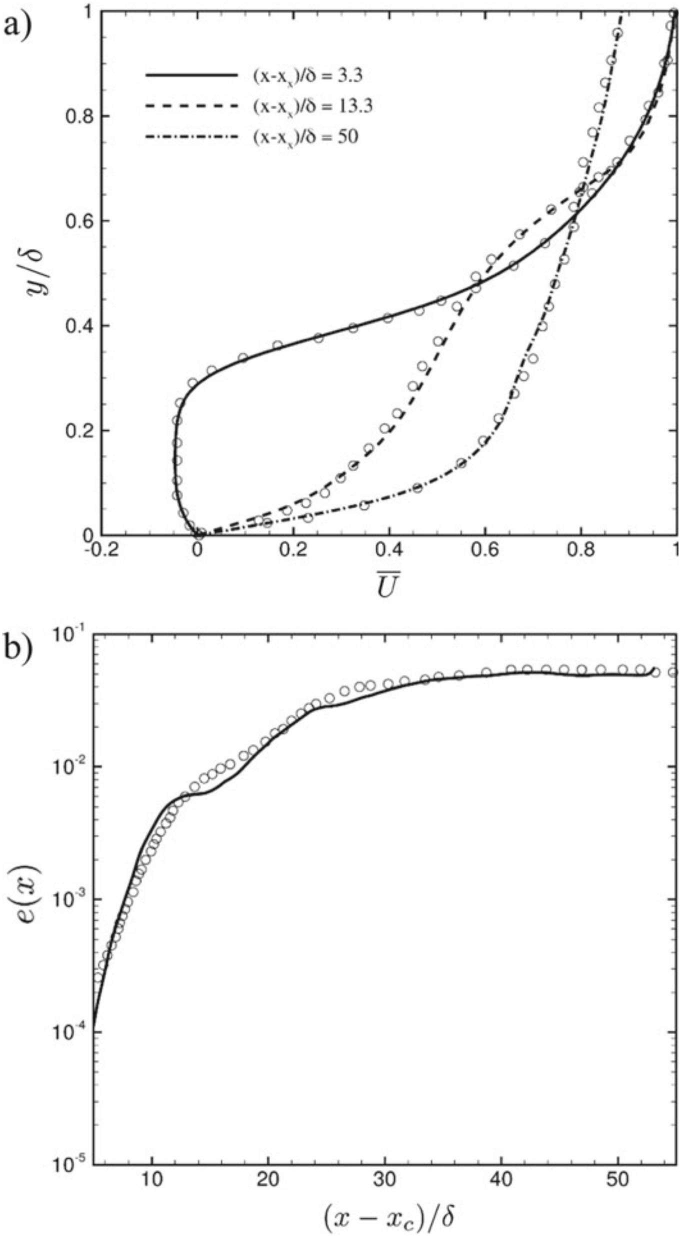

Fig. 37 Comparison with reference numerical data. Time-averaged streamwise velocity at various streamwise stations (**a**) and evolution of the integrated perturbation energy (**b**)

1.6.3 Database Description

Roughness-induced transition in the compressible regime is controlled by many parameters, which makes difficult the identification of general and effective criteria to predict the onset of transition.

In this work we made an effort to produce an extensive DNS database, attempting to cover a wide part of the available parameter space. In particular we have performed a series of simulations varying the following parameters: (i) Mach number (from M = 1.1 to M = 6); (ii) Reynolds number of the incoming boundary layer (the range in terms of roughness Reynolds number is $\mathrm{Re}_k = 400$–1300); (iii) obstacle height as a fraction of the boundary layer thickness ($k/\delta = 0.15, 0.2, 0.25, 0.3, 0.4, 0.7$); (iv) roughness element shapes (we have used hemispheres, cubes and cylinders). Moreover, for the cylindrical elements we also performed simulations changing the obstacle height/diameter aspect ratio (k/D = 0.5, 1, 2). A list of the simulations, all carried out with the same grid and computational setup of the validation test, is reported in Table 5.

It is important to remind that a critical issue in transitional flows is the characterization of the external disturbance environment [19], especially in the supersonic regime, where the boundary layer is quite receptive to free-stream disturbances [20]. In this case the type and the amplitude of the external disturbances can impact the bypass transition process [21], and they can be considered as an additional independent parameter for the problem under investigation. When dealing with numerical experiments, one has the advantage of working with controlled disturbances, and several options are available, as acoustic disturbances, random or well-organized perturbations.

In our simulations, disturbances are triggered within the incoming boundary layer in the form of random fluctuations of all three velocity components, with maximum amplitude of 0.5% of the free-stream velocity, a choice which clearly excites both the acoustic and the vortical modes of motion. Preliminary analysis performed for representative high-Mach number cases has shown that this level of perturbations does not promote the flow transition in the absence of the roughness element. However, the effect of different choices for the external perturbations is not included in this study, this being the main limitation of the present database.

1.6.4 Results—Compressibility Effects

To highlight the qualitative features of the transition process at the various flow conditions, we focus here on the hemispherical roughness element, under adiabatic wall conditions. The time-averaged skin friction coefficient in the symmetry plane is shown in Fig. 38. At all Mach numbers, two flow states occur, depending on the Reynolds number. In the sub-critical state, the boundary layer remains laminar and the skin friction decreases steadily past the obstacle all the way to the end of the computational domain. In the super-critical state, the amplitude of the disturbance caused by the roughness element is sufficient to promote flow breakdown, as indicated by

Table 5 Summary of parameters for DNS study

Shape	k/D	M_∞	k/δ	Re_δ	Shape	k/D	M_∞	k/δ	Re_δ
Hem	0.5	1.1	0.40	2500	Cyl	0.5	1.1	0.40	4300
Hem	0.5	1.1	0.15	6500	Cyl	0.5	2.0	0.40	6500
Hem	0.5	1.1	0.30	6500	Cyl	0.5	4.0	0.40	28000
Hem	0.5	2.0	0.40	4000	Cyl	1.0	1.1	0.40	3655
Hem	0.5	2.0	0.40	9000	Cyl	1.0	1.1	0.40	6500
Hem	0.5	4.0	0.40	15000	Cyl	1.0	2.0	0.40	7500
Hem	0.5	4.0	0.40	28000	Cyl	1.0	4.0	0.40	28000
Hem	0.5	6.0	0.40	40000	Cyl	2.0	1.1	0.40	2500
Hem	0.5	6.0	0.40	85000	Cyl	2.0	2.0	0.40	4000
Cub	1.0	1.1	0.40	3655	Cyl	2.0	2.0	0.40	9000
Cub	1.0	2.0	0.40	6500	Cyl	2.0	4.0	0.40	20000
Cub	1.0	2.0	0.40	14000	Hem	0.5	1.1	0.40	3655
Cub	1.0	4.0	0.40	38000	Hem	0.5	1.1	0.25	6500
Cyl	0.5	1.1	0.40	6500	Hem	0.5	2.0	0.40	3000
Cyl	0.5	2.0	0.40	9000	Hem	0.5	2.0	0.40	6500
Cyl	0.5	4.0	0.40	40000	Hem	0.5	4.0	0.70	5000
Cyl	1.0	1.1	0.40	5000	Hem	0.5	4.0	0.40	25000
Cyl	1.0	2.0	0.40	6500	Hem	0.5	6.0	0.70	14000
Cyl	1.0	4.0	0.40	20000	Hem	0.5	6.0	0.40	70000
Cyl	1.0	4.0	0.40	40000	Cub	1.0	1.1	0.40	2500
Cyl	2.0	1.1	0.40	6500	Cub	1.0	2.0	0.40	5000

(continued)

Table 5 (continued)

Shape	k/D	M_∞	k/δ	Re_δ	Shape	k/D	M_∞	k/δ	Re_δ
Cyl	2.0	2.0	0.40	6500	Cub	1.0	2.0	0.40	11500
Cyl	2.0	4.0	0.40	15000	Cub	1.0	4.0	0.40	28000
Hem	0.5	1.1	0.40	2900	Cyl	0.5	1.1	0.40	5000
Hem	0.5	1.1	0.20	6500	Cyl	0.5	2.0	0.40	7500
Hem	0.5	1.1	0.40	6500	Cyl	0.5	4.0	0.40	34000
Hem	0.5	2.0	0.40	5000	Cyl	1.0	1.1	0.40	4300
Hem	0.5	2.0	0.40	11500	Cyl	1.0	2.0	0.40	5000
Hem	0.5	4.0	0.40	20000	Cyl	1.0	2.0	0.40	9000
Hem	0.5	4.0	0.40	40000	Cyl	1.0	4.0	0.40	34000
Hem	0.5	6.0	0.40	50000	Cyl	2.0	1.1	0.40	3655
Hem	0.5	6.0	0.40	100000	Cyl	2.0	2.0	0.40	5000
Cub	1.0	1.1	0.40	6500	Cyl	2.0	2.0	0.40	11500
Cub	1.0	2.0	0.40	9000	Cyl	2.0	4.0	0.40	40000
Cub	1.0	4.0	0.40	20000					

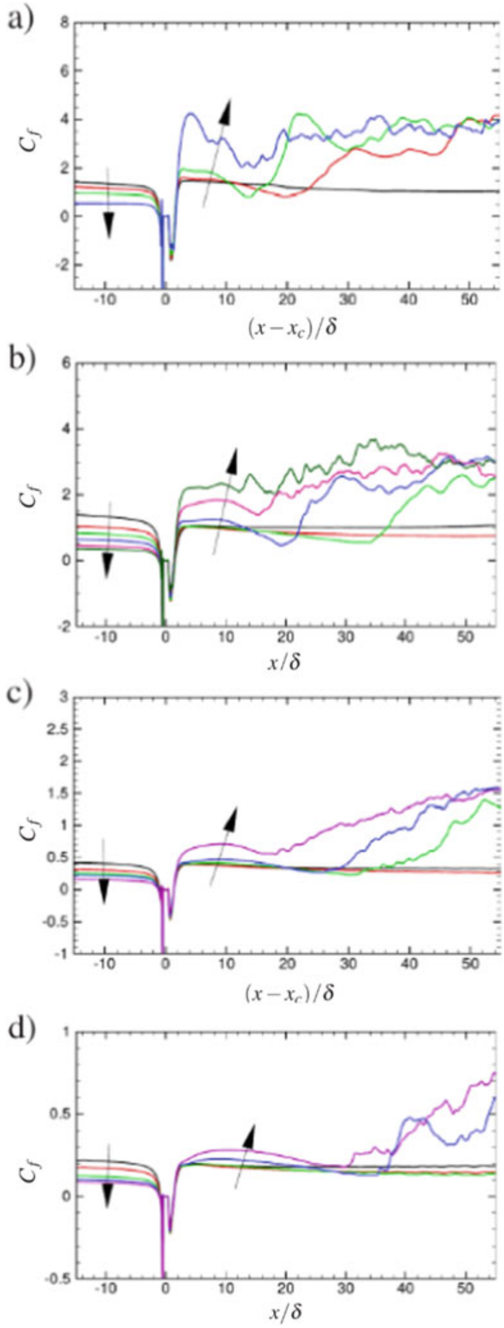

Fig. 38 Mean skin friction coefficient along the symmetry line for hemispherical roughness element with size $k/\delta = 0.4$ **a** $M_\infty = 1.1$, $\mathrm{Re}_\delta = 2500$, 2900, 3655, 6500; **b** $M_\infty = 2$, $\mathrm{Re}_\delta = 3000$, 4000, 5000, 6500, 9000, 11500; **c**, $M_\infty = 4$, $\mathrm{Re}_\delta = 15000$, 20000, 25000, 28000, 40000; **d**, $M_\infty = 6$, $\mathrm{Re}_\delta = 40000$, 50000, 70000, 85000, 100000. The arrows indicate the direction of increase Re_δ

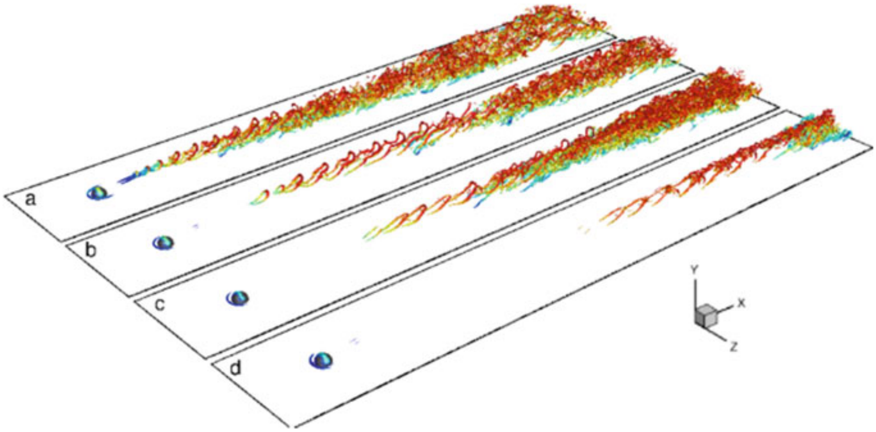

Fig. 39 Coherent vertical structures for flow around hemispherical roughness element. **a** $M_\infty = 1.1$, $\mathrm{Re}_\delta = 6500$; **b** $M_\infty = 2$, $\mathrm{Re}_\delta = 9000$; **c** $M_\infty = 4$, $\mathrm{Re}_\delta = 40000$; **d** $M_\infty = 6$, $\mathrm{Re}_\delta = 85000$. Vortices are educed as isosurfaces of swirling strength, and coloured with the streamwise velocity

the rapid rise of the skin friction coefficient. For a given Mach number, the transition point moves upstream as the Reynolds number is increased, attaining a limiting value for which the roughness is said to be ‘effective’, and further increase of the Reynolds number does not lead to movement of the transition point. A clear interesting effect of compressibility is observed on such limit position, which increases with the Mach number.

Similar considerations can also be drawn looking at the typical structures characterizing the roughness-induced transition process, shown in Fig. 39 through isosurfaces of the swirling strength (i.e. the imaginary part of the intermediate eigenvalue of the velocity gradient tensor) for representative super-critical flow cases. Regardless of the Mach number, the most prominent feature is the shedding of hairpin vortices past the roughness element, which propagate downstream leading to flow breakdown. The generation and the evolution mechanisms of these structures have been widely discussed in the low-speed regime by Acarlar and Smith [13] and Klebanoff et al. [14], and they are mainly related to the instability characteristics of the shear layer behind the obstacle. As for the skin friction, the main effect of the compressibility is to delay the flow breakdown, and the hairpin structures look more elongated as Mach number increases.

To further characterize the influence of compressibility on the transition process, we look at the frequency of hairpin shedding past the roughness element. For this purpose, the time-resolved streamwise velocity signal was stored along the centerline of the computational domain at an off-wall location corresponding to the edge of the roughness element (y = k). Pre-multiplied frequency spectra taken at different streamwise locations are shown in Fig. 40a for a super-critical flow case. As expected, the spectral densities immediately past the obstacle are characterized by a distinct peak, which is the signature of quasi-periodic shedding. The peak slowly vanishes at

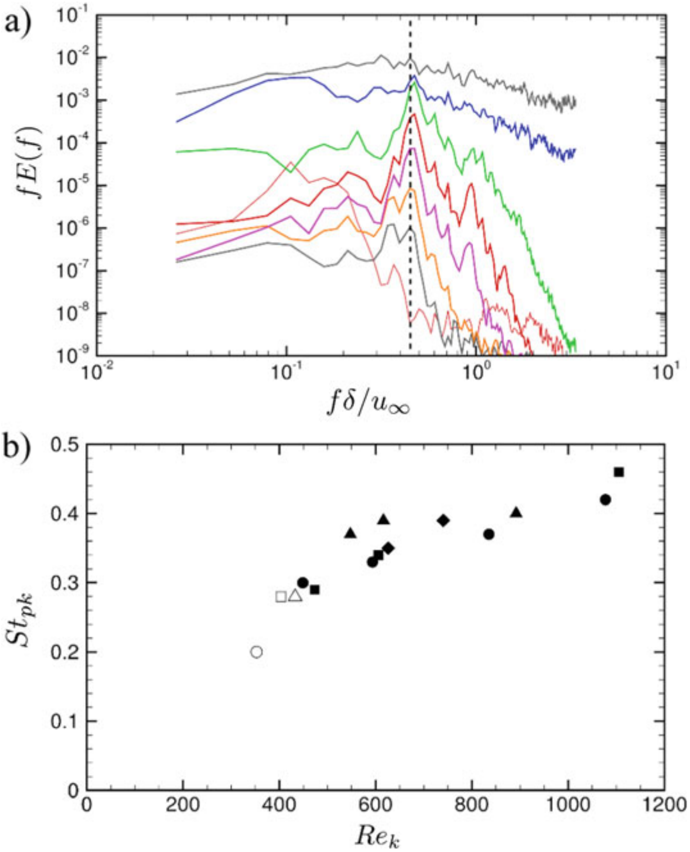

Fig. 40 Pre-multiplied frequency spectra of the streamwise velocity are shown in frame **a** at several streamwise stations ($x/\delta = 5, 17, 18, 19, 20, 23, 30, 40$, from bottom to top) in the symmetry plane at $x = k$, for hemisphere at $M_\infty = 4$, $\mathrm{Re}_\delta = 40000$. The vertical dashed line marks the peak frequency (f_{pk}). Frame **b** shows the peak Strouhal number ($St_{pk} = f_{pk}k/u_k$) derived from maps as in frame (**a**), for flow behind hemispherical obstacles, as a function of Re_k. Symbols: squares, $M_\infty = 1.1$; circles; $M_\infty = 2$; triangles, $M_\infty = 4$; diamonds, $M_\infty = 6$. Solid and hollow symbols correspond to super-critical and sub-critical cases, respectively

downstream stations, where the flow breakdowns, approaching a fully turbulent state, as indicated by the more broad-banded spectra. The typical Strouhal number ($St_{pk} = f_{pk}k/u_k$) associated with the vortex shedding is shown in Fig. 40b as a function of the roughness Reynolds number, for the hemispherical roughness element. Consistent with previous low-speed studies [13, 14], the Strouhal is found to increase with Re_k, in the present case ranging from $St_{pk} = 0.2$ to $St_{pk} = 0.4$. Apparently, the effect of Mach number is not significant when the roughness height and edge velocity u_k are used to form the Strouhal number.

1.6.5 Parametrization of the by-Pass Transition Process

Our goal here is to identify a (possibly) general threshold parameter for the onset of by-pass transition induced by the roughness element. Many generalizations of the roughness Reynolds number criterion to the compressible case have been proposed [22, 17, 19]. Based on the analysis of the present database, we find that a convenient generalization of Re_k is

$$e(x) = \int\int u_{rms}^2 dydz \tag{15}$$

where the density is evaluated at the obstacle edge, and the dynamic viscosity is taken at the wall. Note that Re_{kw} quantifies the ratio between the inertia forces at the edge of the obstacle and the viscous stress at the wall. The performance of Re_{kw} as a controlling by-pass transition parameter can be judged looking at the maps shown in Fig. 41 (left column), in which hollow symbols correspond to sub-critical flow cases, and solid symbols correspond to super-critical cases. To detect the transition onset we monitor the evolution of the time-averaged skin friction coefficient past the obstacle. While no doubts exist for super-critical cases, the stipulation of a flow as sub-critical is necessarily subjected to some uncertainty, owing to the finite streamwise extent of the computational domain.

The figure must then be interpreted with some caution in the sub-critical region. As evident in Fig. 41, the sub-critical and super-critical conditions are well segregated by Re_{kw}, which is promising in taking into account the effect of variations in the Mach number, Reynolds number and roughness height. Such segregation would not be obtained using the conventional definition of roughness Reynolds number. However, the critical value of Re_{kw} is not the same for all the roughness elements, and it ranges between 400 and 700.

limitations of the Re_{kw} criterion we propose an alternative controlling parameter, based on the observation that the main effect of the presence of the obstacle is a deficit in the mass flux (i.e. in the streamwise momentum) downstream of it, which translates into the formation of a low-momentum streak and of a pair of counter-rotating vortices. We then consider a Reynolds number formed with the momentum defect (Q, to be estimated), the maximum cross-stream section of the obstacle, and the wall viscosity,

$$\mathrm{Re}_Q = \frac{Q S_{yz}^{-1/2}}{\mu_w} \tag{16}$$

where $S_{yz} \sim k \cdot D$. It is possible to provide a rough estimate for Q by assuming that the upstream boundary layer is not affected by the obstacle. Assuming that the incoming velocity profile is linear up to the edge of the obstacle, it is easy to obtain the following estimate

$$Q \approx \rho_k k D u_k F(shape). \tag{17}$$

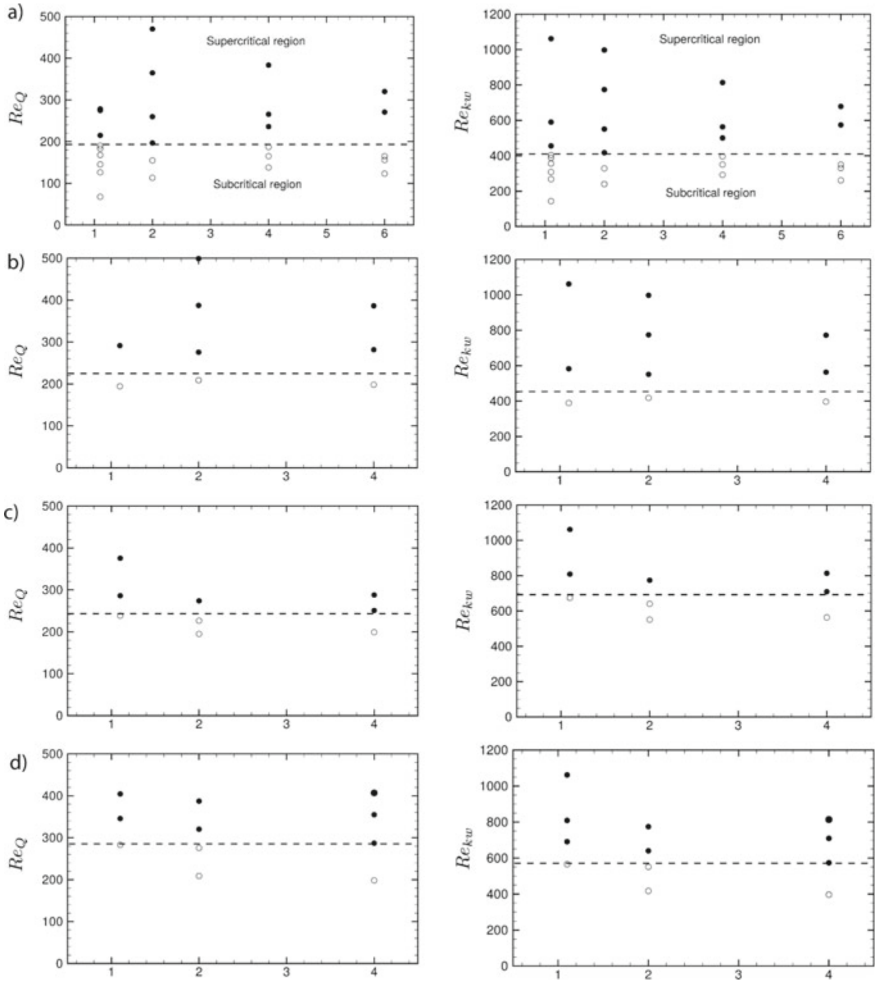

Fig. 41 Transition map as a function of Re_{kw} (left column). **a** hemispheres; **b** cubes; **c** cylinders ($D/k = 2$). Solid/open circles denote super/subcritical cases

Fig. 42 Sketch of the cross-sectional shape of the roughness element

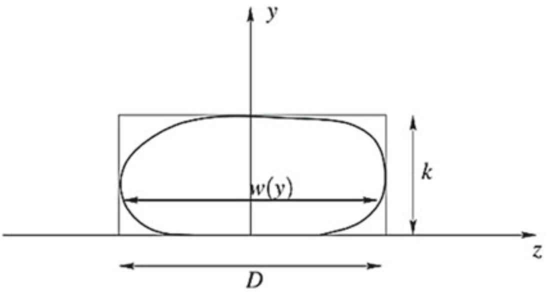

Fig. 43 Dependence of critical roughness Reynolds number on obstacle aspect ratio

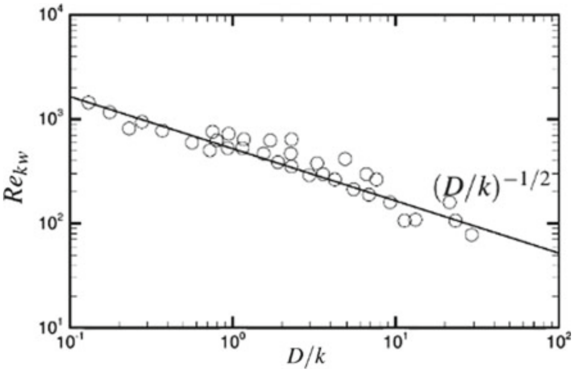

where

$$F(shape) = \int_0^1 \eta w^*(\eta) d\eta \tag{18}$$

with $\eta = y/k$ and $w^*(\eta) = w(y)/D$ defines the cross-sectional shape of the obstacle (see Fig. 9). It is then easy to relate Re_Q to Re_{kw} through

$$\mathrm{Re_Q = Re_{kw} \cdot (D/k)^{1/2} \cdot F(shape)} \tag{19}$$

showing potential of Re_Q to incorporate the effects of the obstacle shape and aspect ratio. The effectiveness of Re_Q as a by-pass transition parameter can be appreciated from Fig. 41 (right column). It appears that, regardless of the object shape and/or aspect ratio, by-pass transition occurs if $\mathrm{Re}_Q > 200 \div 280$, and the scatter is much less than with Re_{kw}.

Apparently, the by-pass transition criterion based on Re_Q correctly captures the experimentally observed trend with the obstacle aspect ratio. In Fig. 43 we show with symbols the critical roughness Reynolds number resulting from a series of experiments (van Driest and Blumer [19] with cylindrical obstacles with different aspect ratio. On the same graph, we show the trend of the critical roughness Reynolds number obtained from Re_Q, which predicts $\mathrm{Re}_{kw} \sim (D/k)^{-1/2}$. Apparently, the trend is correct, and it is at least equally plausible as the frequently quoted empirical scaling $\mathrm{Re}_{kw} \sim (D/k)^{-2/5}$ [23].

1.6.6 Computational Arrangement and Simulation Parameters

The numerical simulations foreseen in WP-1 and WP-2 include the presence of a normal shock wave that interacts with a boundary layer which can be fully laminar, fully turbulent or transitional. To arrange all the requested flow cases we have devised a simple and unified computational set-up, illustrated in Fig. 44.

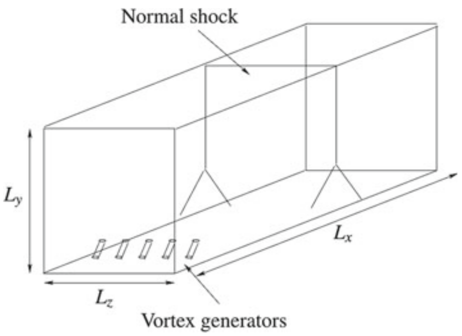

Fig. 44 Sketch of the computational arrangement used for the simulation of the interaction between a boundary layer and a normal shock wave

The domain is a Cartesian box with size $L_x \times L_y \times L_z$ in the streamwise (x), wall-normal (y) and spanwise (z) direction. The normal shock wave is located at some distance (x_s) from the inflow section, and it is made to interact with a boundary layer entering the domain from the inflow station. The leading edge of the plate is not directly simulated, and rather a compressible Blasius similarity solution is used as inflow velocity profile, and also to initiate the simulations. The inflow boundary layer thickness (based on 99% of freestream velocity) is hereafter indicated with, and it is used as the reference length. To control the state of the boundary layer at the beginning of the interaction (laminar, transitional or turbulent) an array of rod vortex generators is used, placed at distance x_r from the inflow.

The geometry of the VGs has been provided by IMP-PAN, and it is described in Fig. 45. Depending on the selected flow conditions (Mach and Reynolds number) and the relative size of the VGs with respect to the boundary layer thickness, the boundary layer may experience transition or not. The rod vortex generators are also used in the case of the laminar interaction to break the initial symmetry of the flow, and to allow the establishment of three-dimensionality across the interaction zone. In this case, care must be taken that the VGs are not effective in causing early transition to turbulence. Preliminary computations for the fully laminar case have shown that the effect of VGs is the same as with random inflow disturbances. Boundary conditions are prescribed by enforcing periodicity in the spanwise direction, and assuming

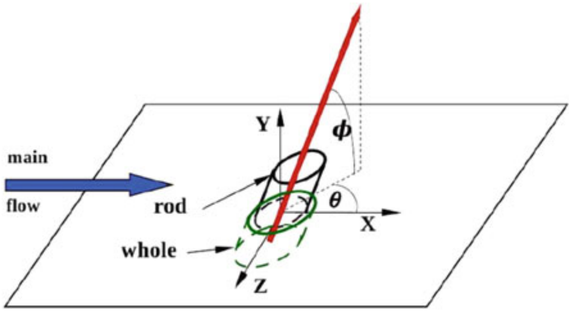

Fig. 45 Sketch of the vortex generator used in the computation

adiabatic no-slip wall conditions at the bottom of the computational domain. Non-reflecting boundary conditions are specified at the outlet and at the upper boundary to minimize spurious reflections of disturbances back into the computational domain [24]. The simulations are initialized by superposing a normal shock field onto the Blasius boundary layer, thus yielding a fictitious transient, after which flow statistics have been collected.

1.6.7 Numerical Parameters

Computations of fully laminar interaction have been carried out for a value of the normal shock strength equal to M = 1.2. The Reynolds number of the boundary layer at the inflow station is 4000, and the Reynolds number at the nominal shock impingement point is 1730000. An array of five VGs with diameter D = 0.11δ and height H = 0.22δ are located at $x_r = 15\delta$, equally spaced in the spanwise direction. The corresponding roughness Reynolds number is $e_k = 250$, at which the obstacles are ineffective in promoting transition.

The computational domain employed for the simulation has size 1000 × 600 × 11 δ and it has been discretized with a grid consisting of points 8192 × 512 × 256. The mesh points are non-uniformly spaced in the streamwise direction to allow better resolution in the region occupied by the VGs and in the interaction zone around the normal shock wave, whereas the spacing is increased towards the computational outlet, starting at x = 500 δ, to filter disturbances prior to hitting the boundary. Points are also clustered in the wall-normal direction to resolve the boundary layer, up to y = 15δ. Finally, the grid points are equally spaced in the spanwise direction. The size of the computational domain has been selected through a series of preliminary calculations. In particular, the length of the computational domain is dictated by the necessity to accommodate the entire interaction zone, including the large region of upstream influence (especially in the case of a laminar interaction) and a large part of the recovery region past the impinging shock. With regard to the extent of the domain in the wall-normal direction, we have found that it is critical to have it as large as possible to prevent choking of the computational duct, thus avoiding bulk motion of the impinging shock. Placing the upper boundary of the domain at 600 δ prevents the occurrence of computational choking over much longer times than those necessary to achieve stationarity of the flow and statistical convergence.

1.6.8 Results for Turbulent Interaction

Numerical parameters

The computation of the fully turbulent interaction has been carried out for a value of the normal shock strength equal to M = 1.3. The Reynolds number of the boundary layer at the inflow station is 20000. An array of ten VGs with diameter D = 0.11 δ and height H = 0.22δ is located at $x_r = 15\delta$, equally spaced in the spanwise direction.

The corresponding roughness Reynolds number is 950, at which the obstacles are expected to promote flow transition.

The computational domain employed for the simulation has a size 150 × 200 × 11δ and it has been discretized with a grid consisting of 10240 × 640 × 1024 points. The mesh points are non-uniformly spaced in the streamwise direction to allow better resolution in the region occupied by the VGs. Points are also clustered in the wall-normal direction to resolve the boundary layer, and the compression fan of the shock wave up to $y = 5\delta$. Finally, the grid points are equally spaced in the spanwise direction. The size of the computational domain has been selected through a series of preliminary calculations. In particular, the length of the computational domain is dictated by the necessity to accommodate the entire interaction zone, including the upstream influence region and a large part of the recovery zone past the impinging shock. With regard to the extent of the domain in the wall-normal direction, we have found that it is critical to have it as large as possible to prevent choking of the computational duct, thus avoiding bulk motion of the impinging shock. Placing the upper boundary of the domain at $y = 200\delta$ prevents the occurrence of computational choking over much longer times than those necessary to achieve stationarity of the flow and statistical convergence.

1.6.9 Characterization of the Incoming Boundary Layer

The statistics of the incoming flow are first analyzed to check that the structure of the boundary layer immediately upstream of the interaction is that of a canonical zero-pressure-gradient (ZPG) boundary layer. To that purpose, the distribution of the Van Driest-transformed mean streamwise velocity

$$U_{vd} = \int_0^u \sqrt{\rho/\rho_w}\, du \tag{20}$$

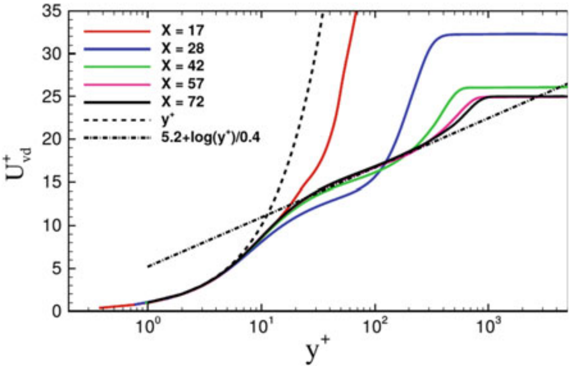

Fig. 46 Distribution of Van Driest transformed mean streamwise velocity in inner scaling at reference stations

Table 6 Properties of incoming boundary layer at the reference station $x_{ref} = 17.3\,\delta_{in}$. $\mathrm{Re}_\theta = \rho_e u_e \theta\ /\mu_e$; $\mathrm{Re}_{\delta 2} = \rho_e u_e \theta\ /\mu_w$; $\mathrm{Re}_\tau = \rho_w u_\tau \delta\ /\mu_w$; $H = \delta^*/\theta$; $H_i = \delta_i^*/\theta_i$

M_e	Re_θ	$\mathrm{Re}_{\delta 2}$	Re_τ	C_f	δ^*/δ	θ/δ	H	H_i
1.3	3770	3020	1003	$2.73 \cdot 10^{-3}$	0.381	0.188	2.03	1.36

is reported in Fig. 46 in inner scaling at some streamwise stations taken past the vortex generators. The figure well describes the evolution of the (initially laminar) boundary layer in the streamwise direction, which, owing to the presence of disturbances generated by the VGs, experience transition to a fully turbulent state, which is achieved approximately at x = 57 δ, where the shape of the velocity profile well conforms to that of a canonical TBL, with a nearly logarithmic region between $y^+ = 30$ and $y^+ = 200$, characterized by a von Karman constant k = 0.41 and additive constant C = 5.2. The global boundary layer properties at a location immediately upstream of the interaction (x = 80δ), are listed in Table 6. The thickness of the boundary layer is determined as the point where u = 99% u_e, and the displacement (δ^*) and momentum (θ) thicknesses are defined as

$$\delta^* = \int_0^{\delta_e} \left(1 - \frac{\overline{\rho}}{\rho_e}\frac{\overline{u}}{u_e}\right) \mathrm{dy},$$

$$\theta = \int_0^{\delta_e} \frac{\overline{\rho}}{\rho_e}\frac{\overline{u}}{u_e}\left(1 - \frac{\overline{u}}{u_e}\right) \mathrm{dy}, \tag{21}$$

where δ_e is the edge of the rotational part of the flow field, and u_e and ρ_e are the corresponding external mean velocity and density. The 'incompressible' boundary layer thicknesses (pedex i) and the associated shape factor (H_i) are also determined from the above equations by setting the density ratio to unity.

1.6.10 Mean Wall Properties

The mean wall pressure across the interaction zone is here compared with the experimental data of Delery and Marvin. Note that the former were obtained in a transonic channel with a wall-mounted bump to accelerate the flow and form a supersonic region terminated by a quasi-normal shock wave. Hence, owing to the presence of the bump, the boundary layer upstream of the shock wave develops under favourable pressure gradient, and it exhibits a fuller profile than in a ZPG boundary layer at the same Reynolds number. As a consequence, the wall pressure distribution is not constant upstream of the interaction, and the incompressible shape factor has a relatively small value (see Table 7). Because of the differences in the Reynolds numbers, and the sensitivity of the flow details on the downstream conditions, comparison with experiments should only be interpreted in qualitative sense.

Let the interaction length-scale L be defined as the distance between the sonic point location x_1(i.e. the streamwise station where the mean wall pressure equals the

Table 7 Interaction parameters for DNS and experiments (the subscript 0 refers to the origin of the interaction)

	M_0	$\mathrm{Re}_{\theta 0}$	H_{i0}	L/δ_0^*	$L/\delta_0^*/(H_{i0}-1)$
DNS	1.3	3770	1.36	25.5	70.
Delery and Marvin [25]	1.3	7526	1.30	21.	70.

critical pressure $p^* = 1.46 p_e$ at $\mathrm{M} = 1.3$), and the origin of the interaction x_0 (i.e. the point where the wall pressure starts to rise) For weak-to-moderate interactions, Delery and Marvin showed that scales with the upstream boundary layer properties according to

$$\mathrm{L} \approx 70\delta_0^*(H_{i0} - 1) \tag{22}$$

As observed in Table 7, the computed interaction length-scale agrees fairly well with the equation above; Delery and Marvin also showed collapse of the wall properties (at various Re and M) when reported in the scaled interaction coordinates $x^* = \frac{x - x_0}{L}$, $y^* = y/L$. In the following, for comparison purposes, the results are then reported in terms of x^* and y^* and we refer to three distinct zones: the upstream ZPG region ($x^* < 0$); the supersonic adverse-pressure-gradient (APG) region ($0 < x^* < 1$); and the subsonic APG region ($x^* > 1$).

The scaled mean wall pressure is reported in Fig. 47a together with the inviscid pressure jump predicted by the Ranking-Hugoniot relations. It exhibits a sharp rise in the supersonic APG region, in excellent agreement with experiments, and a milder increase in the subsonic APG region.

Note that, remarkably, the distribution obtained in the present DNS is nearly identical to that of a previous computation Pirozzoli et al. [26], performed with the recycling/rescaling method, without taking into account the full spatial evolution of the incoming boundary layer, from a laminar to a fully turbulent state. This agreement confirms the validity of the approach here followed, which has the advantage to be more general and to allow the opportunity of simulating transitional interactions.

The distribution of the mean skin friction coefficient is reported in Fig. 47b together with that obtained in the absence of the normal shock. These curves are nearly identical up to (x/δ ~ 90), which marks the location of the shock upstream influence and are characterized by a rapid rise of the friction coefficient at x, corresponding to the flow breakdown and the transition to a turbulent state. While in the absence of the normal shock the skin friction slightly decreases in the fully developed turbulent region, in the case of SBLI, starting from x = C_f exhibits a sudden drop, and attains a minim (close to zero), before showing a slow recovery past the interaction zone. According to Delery and Marvin the present case is to be classified as an incipient separation one.

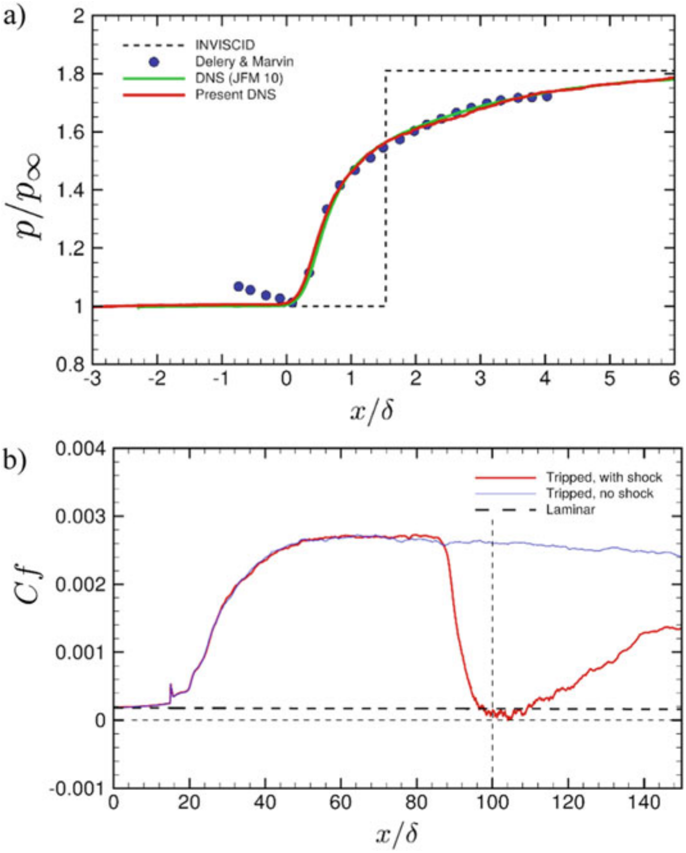

Fig. 47 Distribution of mean wall pressure (**a**) and skin friction coefficient (**b**). *R–H* denotes the inviscid distribution resulting from the Rankine-Hugo10niot jump conditions. Refer to Table 7 for nomenclature of symbols

1.6.11 Flow Visualizations: Instantaneous Fields

The computed instantaneous density, streamwise velocity and pressure fields are reported in Fig. 48 in the streamwise, wall-normal plane at a given time frame. As observed by Pirozzoli and Grasso [27]in the case of an impinging shock/boundary layer interaction at supersonic Mach number, and by Na and Moin [28] for a low-speed turbulent boundary layer under adverse pressure gradient, the instantaneous pressure field highlights the formation of pressure minima associated with the shedding of eddies that form in the proximity of the outermost inflection points of the mean velocity profiles. As better appreciated from inspection of the flow animations (available on the TFAST website), such vortices lift off from the wall approximately in the middle of the interaction zone, and propagate downstream giving rise to a turbulent mixing layer. Sharp density interfaces are also observed in the outermost

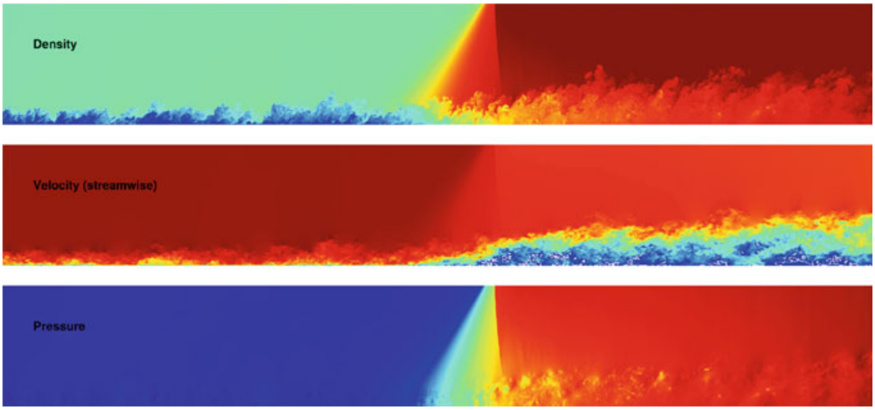

Fig. 48 Instantaneous fields of density, streamwise velocity and pressure in streamwise, wall-normal plane. The corresponding animation is available on the TFAST website

part of the boundary layer, separating boundary layer turbulence from the outer, essentially inviscid flow, and that become more convoluted past the interaction zone.

For a more complete representation of the flow, in Fig. 49 we report a three-dimensional instantaneous view of vortical structures educed with iso-surfaces of the swirling strength (i.e., the imaginary part of the intermediate eigenvalue of the velocity gradient tensor). The location of the normal shock is visible through contours of the pressure field, reported in a x-y plane slice. The figure allows to appreciate the full spatial evolution of the boundary layer, which undergoes transition past the

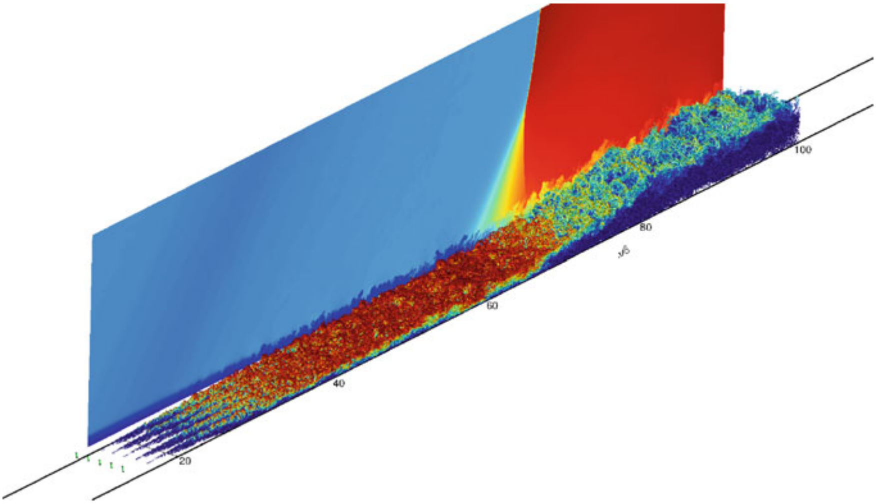

Fig. 49 Flow visualization for turbulent interaction at $M_s = 1.3$. Vortical structures are educed through iso-surfaces of the swirling strength. The pressure field is also shown in a x-y plane slice

VGs element. The most prominent feature is the shedding of hairpin vortices, which propagate downstream, past the roughness element, leading to flow breakdown. The generation and the evolution mechanisms of these structures have been widely discussed in the low-speed regime by Acarlar and Smith [13], Klebanoff et al. [14] and they are mainly related to the instability characteristics of the shear layer behind the obstacle.

2 Interaction Sensitivity to Transition Location

2.1 IUSTI

We present in this section an analysis of the influence of the position and the height of the perturbations on the transition to the turbulence of the interaction. All the experimental results have been summarized in order to define critical region of influence of upstream perturbations. From the various experiments achieved with different heights and unit Reynolds numbers it is possible to evaluate the critical size of the step able to generate turbulent conditions upstream and/or downstream from the interaction. In cases of turbulent upstream conditions, it has been found that the flow remains attached, whatever the imposed flow deviation considered. It has not been possible to obtained attached flow with no turbulent upstream boundary layer: all the other cases have been found separated with large aspect ratios of the interaction.

A Reynolds number based on the height of the step has been used to summarize these different results. It is based on the height of the step h, its location along the plate x and the maximum velocity seen by the step $U_h = U(y = h)$. This corresponds to an immersed Reynolds number. Then, Re_{hi} is defined as:

$$\mathrm{Re}_{hi} = \frac{\mathrm{U_h h}}{\upsilon_e} \tag{23}$$

In case of laminar boundary layers, the velocity profile can be considered as linear for $y/\delta < 0.5$. Therefore, U_h can be approximated by:

$$\frac{\mathrm{U_h}}{\mathrm{U_e}} \cong \frac{1}{\mathrm{k_1}} \frac{\mathrm{h}\sqrt{\mathrm{Re_u}}}{\sqrt{\mathrm{x}}} \tag{24}$$

with $k_1 = 4.2$ (see Fig. 21, chapter “WP-1 Reference Cases of Laminar and Turbulent Interactions”) and the relation (22) can be expressed as:

$$\mathrm{Re_{hi}} = \frac{1}{\mathrm{k_1}} \mathrm{Re_u^{3/2}} \frac{\mathrm{h^2}}{\sqrt{\mathrm{x}}} \tag{25}$$

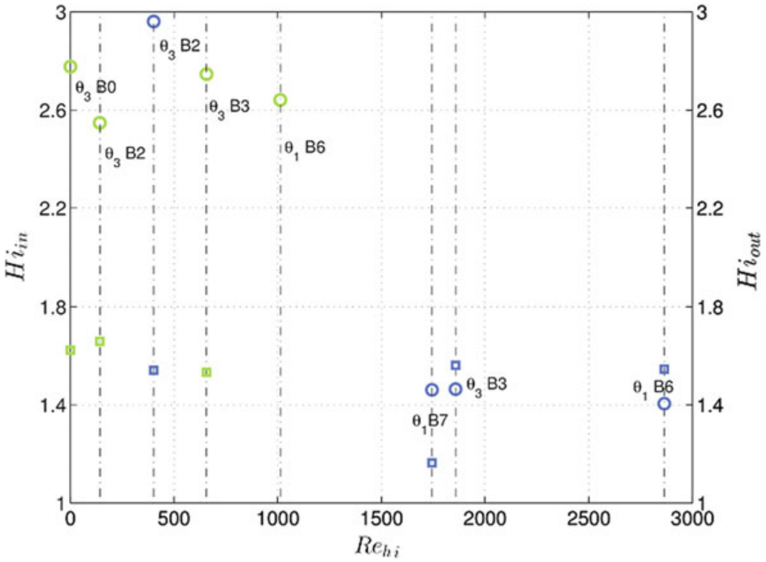

Fig. 50 $P_0 = 0.4$ atm

with Re_u the unit Reynolds number. The incompressible form factors of the upstream and downstream boundary layers are reported on Fig. 50 versus this parameter. Green and blue symbols correspond respectively to the $P_0 = 0.4$ atm and $P_0 = 0.8$ atm cases. The circles correspond to the upstream section and the square to the downstream one. Symbols are labeled with the corresponding flow deviation and tripping device. The form factors are plotted vs the immersed Reynolds number Re_{hi} and the natural case are reported for $\mathrm{Re}_{hi} = 0$. The largest form factors (about 2.7), correspond to the laminar conditions, when the turbulent conditions have form factors around 1.4. The downstream transitional states corresponds to the symbols labeled $\Theta_3 B_0$ and $\Theta_3 B_2$ for the $P_0 = 0.4$ atm cases: they are not clearly characterized from their form factors, only slightly larger than the other downstream turbulent cases. Different domains can be defined from these results:

- for experiments with values of immersed Reynolds number at least up to 140, laminar input conditions are observed and only a transitional boundary layer is developing downstream from the reattachment point
- for Reynolds number such as $400 \leq \mathrm{Re}_{hi} \leq 1000$, laminar input conditions are observed and a turbulent boundary layer is developing downstream from the reattachment point. The flow remains separated
- for Reynolds number such as $1750 \leq \mathrm{Re}_{hi}$, turbulent conditions are observed upstream and downstream from the interaction. The flow is attached whatever the imposed flow deviation.

These results are summarized on Fig. 51 for the two stagnation pressures $P_0 = 0.4$ atm and $P_0 = 0.8$ atm. The X axis is the longitudinal section of the flat plate and

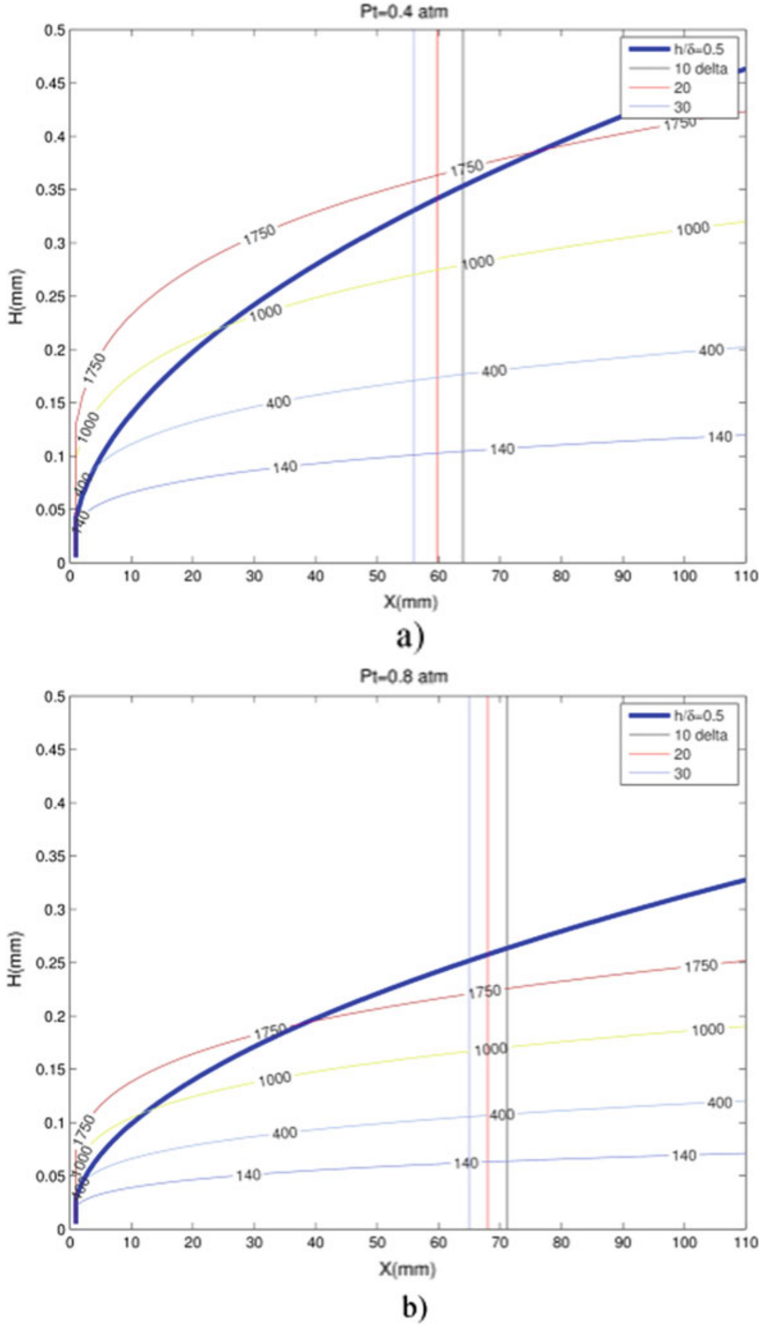

Fig. 51 Characteristic immersed Reynolds numbers. **a** $P_0 = 0.4\,\text{atm}$; **b** $P_0 = 0.8\,\text{atm}$

the Y axis is the height of the step in mm. The isovalues Reynolds number Re_{hi} curves are given for the values 140, 400, 1000 and 1750. Superimposed on the graphs is the curve corresponding to step heights equal to $0.5\delta_h$. This can be considered as an upper limit of the size of the steps. The 3 vertical lines show the section corresponding respectively to 10, 20 and 30 local boundary layer upstream from the location of the initial rise of pressure (compression waves).

These results are summarized in Fig. 51 for the two stagnation pressures $P_0 = 0.4$ atm and $P_0 = 0.8$ atm. The X axis is the longitudinal section of the flat plate and the Y axis is the height of the step in mm. The Reynolds number Re_{hi} isovalue curves are given for the values 140, 400, 1000 and 1750. Superimposed on the graphs is the curve corresponding to step heights equal to $0.5\delta_h$. This can be considered as an upper limit of the size of the steps. The 3 vertical lines show the section corresponding respectively to 10, 20 and 30 local boundary layer upstream from the location of the initial rise of pressure (compression waves). Therefore, these pictures give a first estimation of the possibilities (height and position) for control systems able to obtain:

- separated interactions, upstream laminar conditions, and downstream transitional conditions (region under the isoline 140)
- separated interactions, upstream laminar conditions, and downstream turbulent conditions (region between the isolines 400 and 1000)
- attached interactions, upstream turbulent conditions, and downstream turbulent conditions (region over the isoline 1750).

  The evolution of the unsteadiness inside along the interaction has been shown to follow these regions of immersed Reynolds numbers.
- unsteady interaction, involving low frequencies (if compared to the scales of the upstream boundary layer) developing along the mixing layer downstream of the separation point. Nevertheless, the dominant scales remain the unsteadiness coming from the upstream laminar boundary layer (region under the isoline 140)
- unsteady interaction, the dominant scales are the lower frequencies developing along the mixing layer (region between the isolines 400 and 1000)
- attached/turbulent interactions with no evidence of low frequency unsteadiness ($\mathrm{Re}_{hi} > 1700$).

From these figures it is clear that, with the actual set-up, the 0.4 atm case has limited possibilities to generate attached flow, it means upstream turbulent conditions. The 0.8 atm case has a larger efficient region, but requests quite small height (typically $y < 0.2$ mm). Of course, these results are based on steps experiments, and we can expect some differences for other perturbations such as Rod Vortex Generators, but the differences are not expected that large, and we should stay in vicinity of the regions highlighted on the figures.

2.2 ITAM

Passive and active methods of the laminar-turbulent transition control studied in ITAM (Sect. 1) have not led to a smooth displacement of the transition location. Therefore it was decided to investigate the sensitivity of the interaction zone to the transition location for the case of natural turbulization. Table 8 shows the main parameters of the experiments.

Figure 52 shows the results of schlieren visualization of the interaction zone. For the transitional case the size of the interaction region is less than for the laminar case. Decreasing of wedge angle results in slight shift of the position of the laminar-turbulent transition downstream. It is necessary to note that for zero pressure gradient BL (no shock) laminar-turbulent transition take place close to the interaction zone. Therefore, in this case the pressure gradient has little effect on the position of the transition. An increase of the Reynolds number significantly reduces the size of the separation region (not shown here).

The velocity fields measured at different wedge angles are shown in Fig. 53. It is interesting to note that in contrast to the laminar case, for the transitional one the separation shock wave was substantially weaker. Comparing the data obtained for similar size of the separation zone for the transition case (Fig. 53, $\beta = 3°$) and the laminar case (Fig. 53, $\beta = 2°$) it is clear to see that the reflected shock wave is well observed only for the laminar case. This flow feature can be explained by difference of unsteady flow in the interaction for different states of the incoming boundary layers. The periodic passage of turbulent spots through the interaction zone for the transitional case should lead to the suppression of the separation and the disappearance of the corresponding shock wave. After this the separation zone begins to return to its laminar state. As a result of this phenomenon the observed mean velocity fields are formed.

An important change of the flow was found in the wake, where the thickness of the turbulent boundary layer for the transitional case was much smaller than for the laminar or turbulent ones. This was confirmed by the data shown in the Fig. 65 (chapter "WP-1 Reference Cases of Laminar and Turbulent Interactions"). It is clear that weak growth of the momentum thickness for the transitional test case is accompanied by small level of pulsations in comparison with the laminar test case. In

Table 8 Parameters of experiments

M	P_0, bar	T_0 (K)	Re_1, 10^6 1/m	X_{imp} (mm)	β (°)	$\mathrm{Re}_{X\mathrm{imp}}$, 10^3	δ* (mm)	
1.43	0.533	284.7	8.77	183	4	1600	–	Tran.
1.43	0.688	284.5	10.91	183	1,2, 3,4	2000	0.31	Tran.
1.43	0.841	285.6	13.27	183.5	4	2435	0.31	Tran.
1.43	0.976	286.5	15.32	183.5	1,2, 3,4	2810	0.24	Tran.

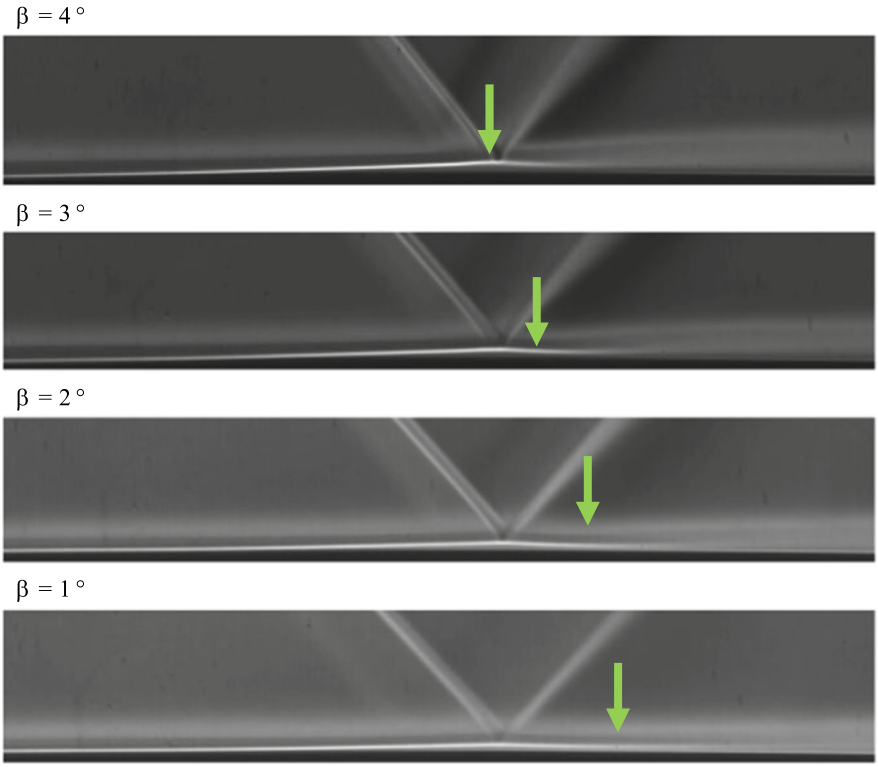

Fig. 52 Schlieren visualization (transitional case, L = 200 mm, $Re_1 = 10.9e6$ 1/m)

Fig. 54 one can see the energy distribution for the first 20 modes estimated by POD analysis. The zones of measurements for all cases were approximately the same that allows to perform a quantitative comparison. The energy of structured oscillations of the flow for the laminar case significantly exceeds the values obtained for turbulent and transitional cases. Thus for laminar case the powerful coherent structures present in the interaction zone. It is most likely that these structures have a significant effect on mean flow and are responsible for the rapid growth of the thickness of the boundary layer in the wake. The presence of turbulent spots for the transitional case destroys the mechanism of generation of these structures.

In Fig. 55 one can see the distribution of PSD$(f)f$ along the SWBLI in beginning (Fig. 55a) and ending (Fig. 55b) of the transition zone. For the transitional case in the incoming boundary layer on can see presence of a peak of pulsations with frequency of about 5–8 kHz, which may be related to processes of turbulent spot formation. Correlation analysis shows that these disturbances propagate downstream. Near the point of X_{imp} there is a sharp increase of the pulsations associated with the turbulization of the boundary layer. Further downstream we can see rapid increase of the β = 4 °

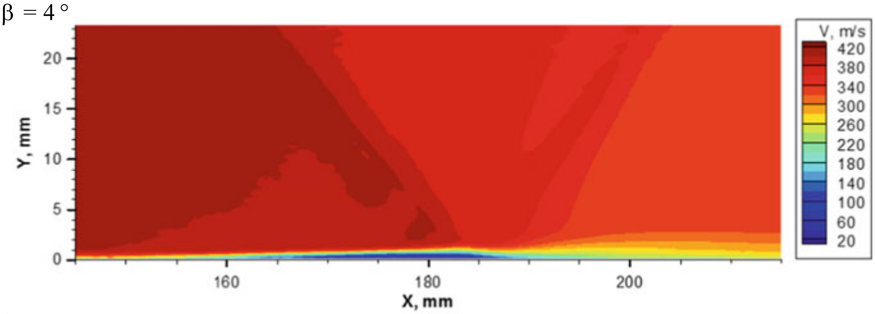

β = 3 °

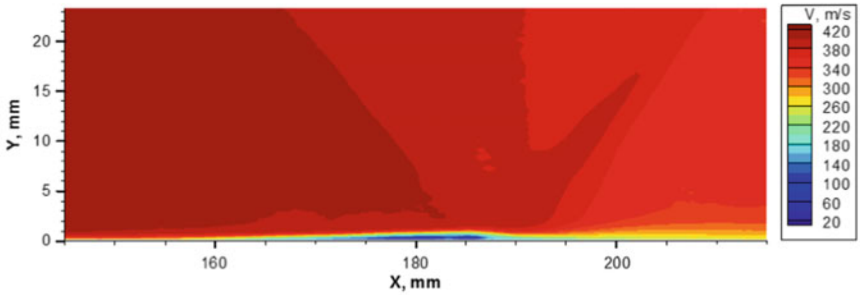

β = 2 °

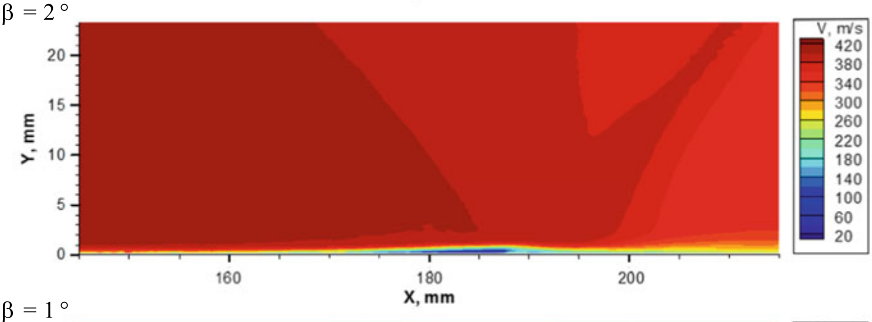

β = 1 °

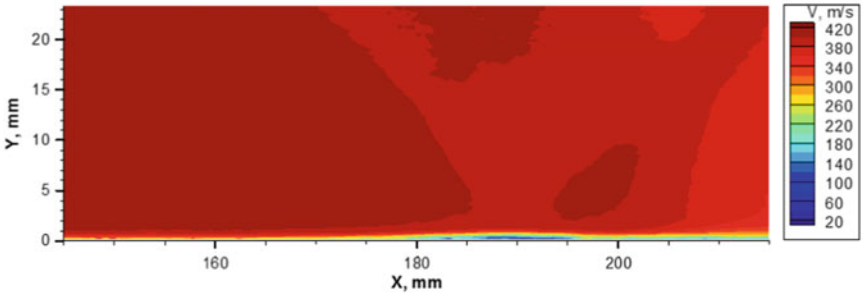

Fig. 53 Velocity fields (transitional case, L = 200 mm, $Re_1 = 10.9e6$ 1/m)

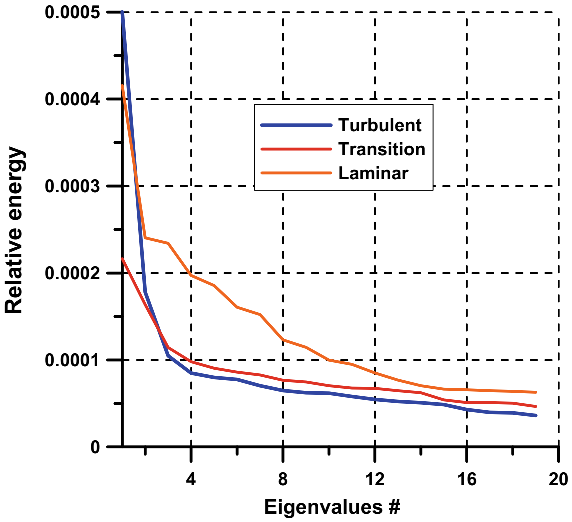

Fig. 54 Relative energy associated with mode #m

pulsations for all frequency band. This means the formation of well-developed turbulent boundary layer. Peak of pulsation at low frequency (about 1 kHz) is obviously due to some feedback process (oscillation of the shock wave and separation zone). From the correlation study it was concluded that disturbances up to 0.5 kHz are moving upstream in the separation region. The spectrogram obtained at the end of the transition zone is close to the turbulent case. However the low-frequency oscillations of the separation shock wave are not found here.

Data for a quantitative comparison can be obtained from the pressure fields. The method of the pressure fields calculation basing on PIV data is presented in [1]. For comparison two parameters are used: F_L and F_D. F_L corresponds to loss of lifting properties of a surface (for wing, compressor blades, etc.) due to the pressure rise in comparison with inviscid case and calculated as

$$F_L = \int_{X_{in}}^{X_{imp}} \left(P_{st} - P_{st_{in}}\right) dx \tag{26}$$

F_D is an integral value of the total pressure losses in the shear layer due to the formation of SWBLI zone. It is calculated as difference between the integral pressure losses at inflow boundary and the value obtained in point X_{imp}:

$$F_D = \int_0^y P_{0_{in}} dy - \int_0^y P_0 dy \tag{27}$$

Fig. 55 Spectrogramm of wall pressure pulsations for laminar test case ($P_0 =$ 0.7 bar)

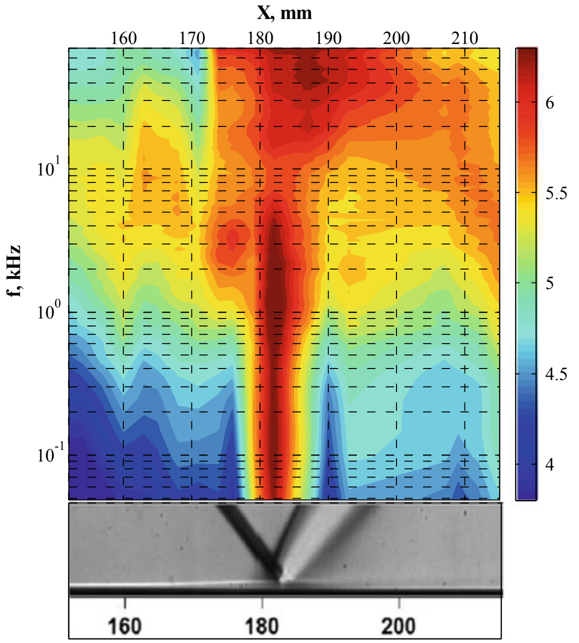

a) (L=200 mm)

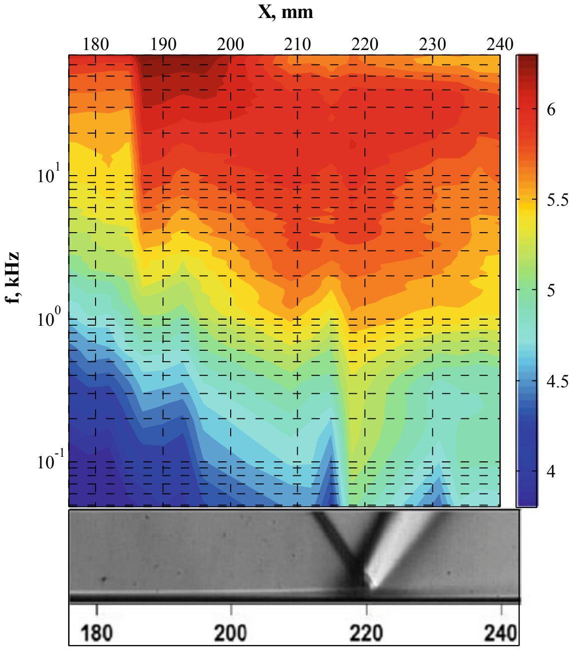

b) (L=160 mm)

The production of the upstream dynamic pressure and upstream boundary layer displacement thickness was chosen to normalize the parameters F_L and F_D.

In Fig. 56 it is clear to see that for the dimensional and dimensionless plots there is approximately linear dependence of the stagnation pressure losses on the wall pressure, regardless of the inflow boundary layer state. Let’s consider in detail the

Fig. 56 Dimension (**a**) and dimensionless (**b**) values of total pressure loss vs the increase of wall pressure on the model

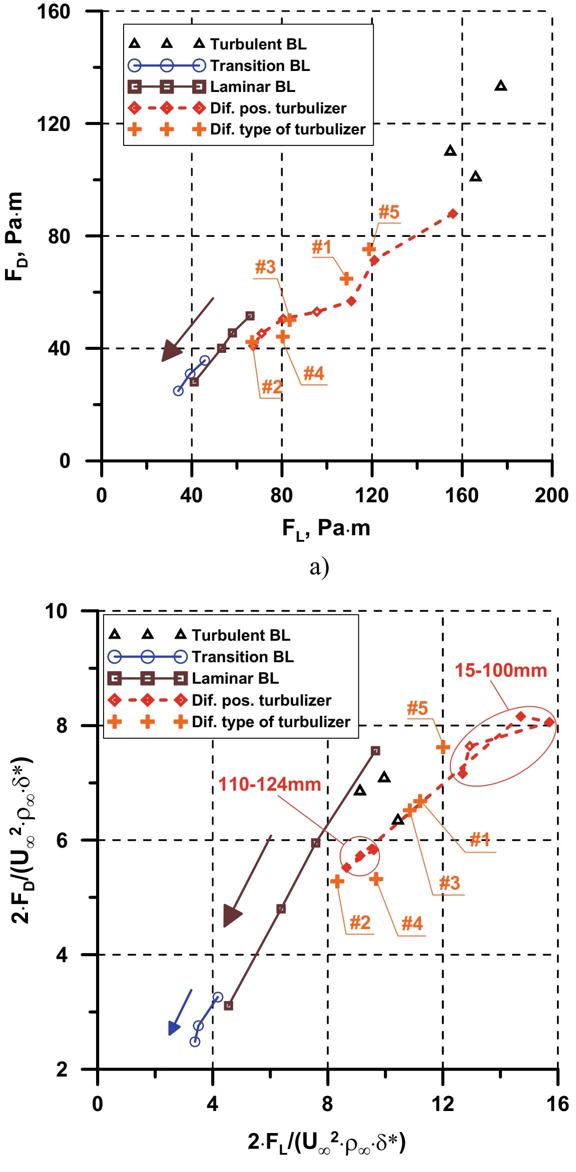

a)

b)

data presented in the Fig. 56b. The increase of unit Reynolds number (shown by arrow) improves the parameters of SWBLI for laminar and transitional cases. The values obtained for laminar and transitional cases lie on the same curve. This can be explained by the increase of inflow disturbances (up to the turbulent state of the inflow boundary layer) which make the boundary layer more resistant to adverse pressure gradient. However for the case of turbulent inflow boundary layer there is a sharp reduction of parameters of the interaction zone.

Unit Reynolds number has little effect on the dimensionless parameters F_L and F_D for the turbulent cases. This confirms the strong dependence of the SWBLI parameters on the level of and type of pulsations in the inflow boundary layer. It is interesting to note that the dimensionless parameters for the turbulent and laminar case at the low unit Reynolds number are approximately the same.

The turbulators producing laminar-turbulent transition upstream of the interaction zone, make the parameters of the zone slightly worse compared to the case of natural turbulization. As a result, we can make a preliminary conclusion that the best parameters of the SWBLI zone may be obtained when the inflow boundary layer is in the transitional state. Turbulent case has no advantages in comparison with laminar, therefore from this point of view, using of roughness for the laminar flow is not beneficial.

The obtained data show that the presence of turbulence spots (intermittency) can significantly improve the flow in the SWBLI zone, which is demonstrated in Sect. 1 for the example of active flow control by an electric discharge.

The physical mechanism of the development of nonstationary effects in the interaction zone for the transitional case raises many questions requiring an intensive study.

2.3 ONERA-DAFE

2.3.1 Comparison Between Cadcut and "ZZ" Tape Devices

Figure 57 shows a comparison of Schlieren visualizations from the reference case and the two controlled cases (Cadcut and ZZ100 tape) for the X_{d1} location on the flat plate. For the reference case (see Fig. 57a), the incoming laminar boundary layer is separated due to the impact of the shock-wave and the transition process appears in the interaction domain because vortex structures are visible only in the mixing layer downstream of the interaction region. The effect of both control devices (easily identified due the presence of compression and expansion waves, see Fig. 57b, c) is to eliminate the separation region and to rapidly trigger the transition. Indeed, vortex structures are now present far upstream of the interaction domain (behind the turbulators, more clearly visible for the ZZ100 tape device).

Figure 58 shows a comparison of oil flow visualizations from the reference case and the two controlled cases (Cadcut and ZZ100 tape) for the X_{d1} location on the flat plate. For the reference case, one notices the footprints of the shock pattern (I)

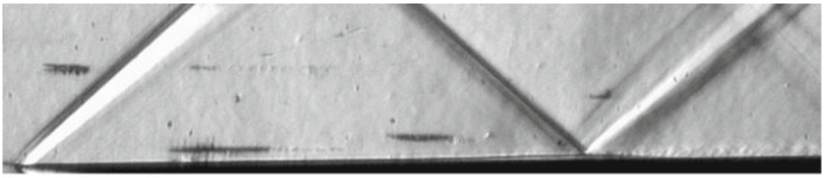

a) - reference case

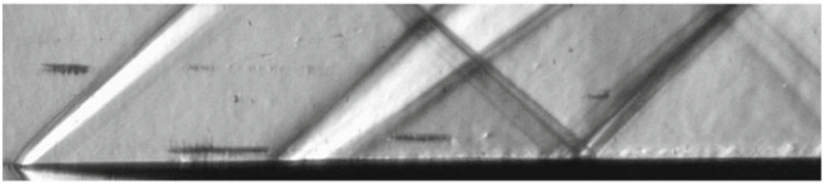

b) - control case: ZZ100 tape

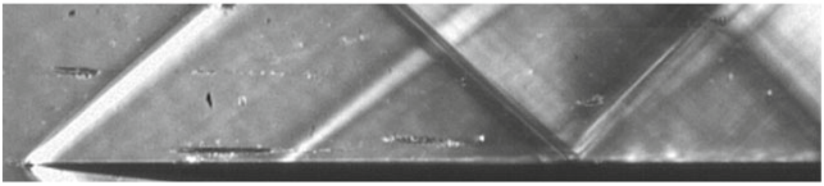

c) - control case: Cadcut

Fig. 57 Schlieren visualizations (devices at X_{d1} location)

and the waves emanating from the shock holder (R1 and R2). On the other hand, the separation line (D) is barely visible. For both controlled cases, flow topologies are very similar and one clearly sees the generation of vortices in the wake of the devices.

Figure 59 shows a comparison of temperature maps obtained by IR thermography measurements from the reference case and the two controlled cases (Cadcut and ZZ100 tape) for the X_{d1} location on the flat plate. While the temperature level increases in the interaction domain for the reference case, the temperature starts to increase just downstream of the devices (the ZZ100 tape is identified as a dark blue band, see Fig. 59b). This increasing is strengthened by the control with the Cadcut device (see on Fig. 59c the yellow spots in the vicinity of the device). This means that both devices forced the transition of the boundary layer. However, these temperature maps do not give a clear indication concerning the (no) existence of the separated region.

2.3.2 Effect of the Device Height

Figure 60 shows a comparison of oil flow visualizations from the "ZZ" tape device with the two selected heights (ZZ100 and ZZ200) for the X_{d1} location on the flat

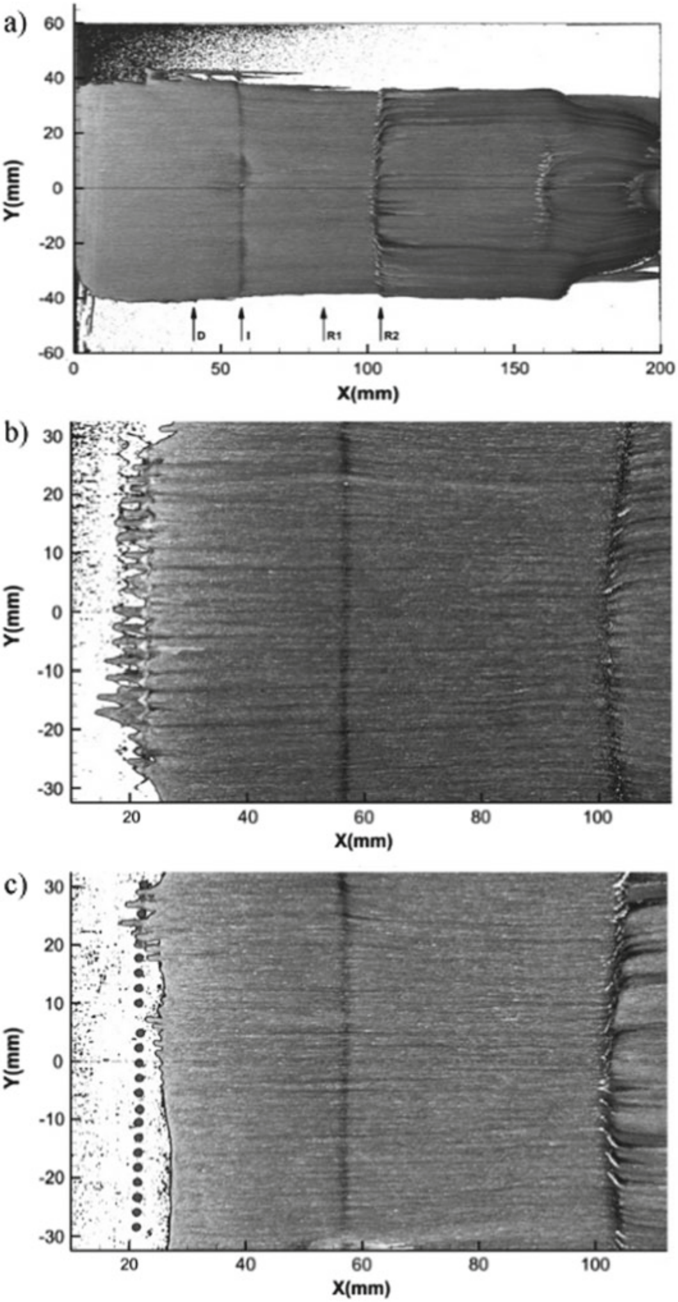

Fig. 58 Oil flow visualizations (devices at X_{d1} location)

Fig. 59 Temperature maps by IR thermography measurements (devices at X_{d1} location)

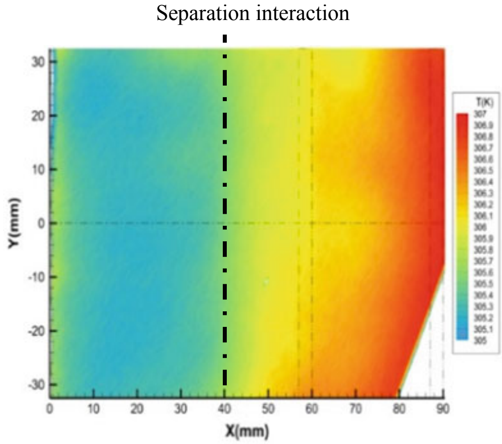

a) - refeence case

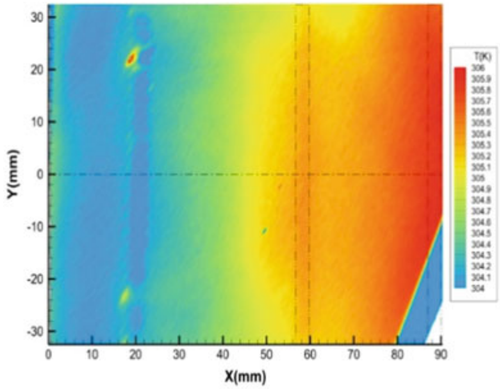

b) - control case: ZZ100 tape

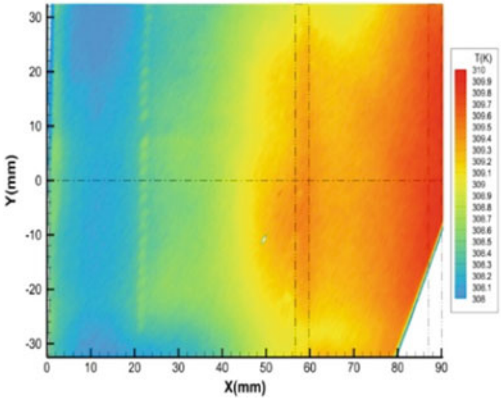

c) - control case: Cadcut

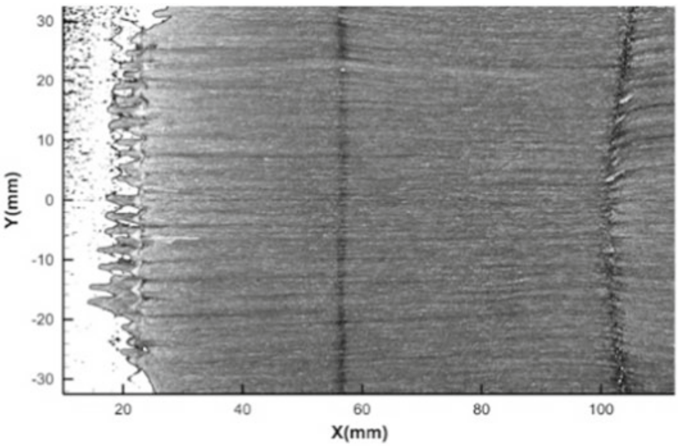

a) - control case: ZZ100 tape

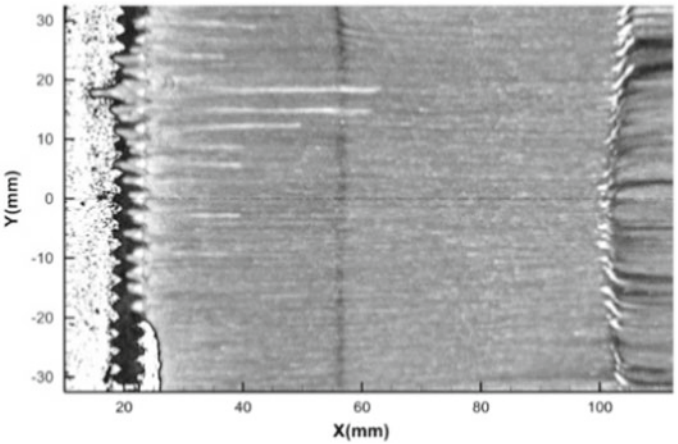

b) - control case: ZZ200 tape

Fig. 60 Oil flow visualizations (devices at X_{d1} location)

plate. Even if flow topologies are very similar, it seems that vortices generated in the wake of the highest device (ZZ200) are stronger.

Figure 61 shows a comparison of temperature maps obtained by IR thermography measurements from the “ZZ” tape device with the two selected heights (ZZ100 and ZZ200) for the X_{d1} location on the flat plate. While the temperature level starts to continuously increase just downstream of the ZZ100 tape device (see Fig. 61a), one notices a different evolution of temperature distribution behind the ZZ200 tape device: the temperature starts to increase but rapidly decreases to reach the level upstream of the turbulator and, then, increases again near the interaction region (see Fig. 61b). This (re-)laminar state of the boundary layer downstream of the turbulator

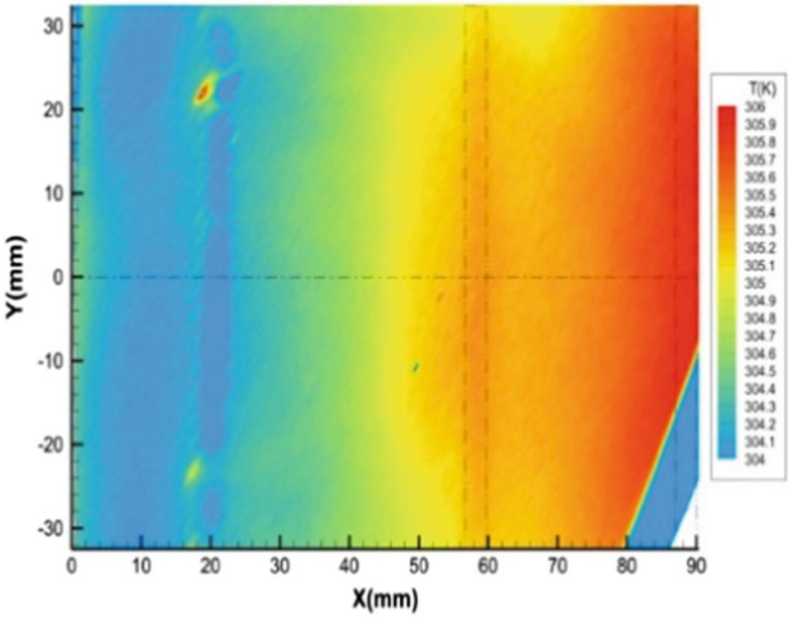

a) - control case: ZZ100 tape

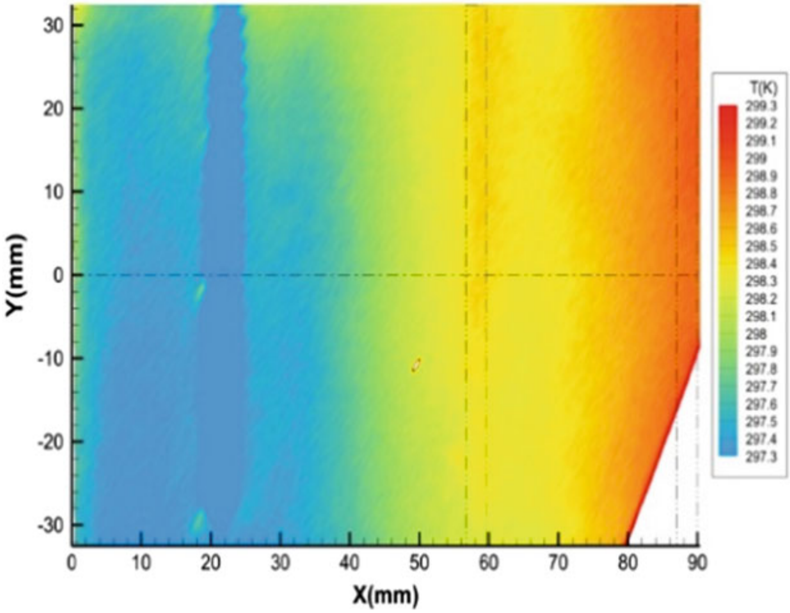

b) - control case: ZZ200 tape

Fig. 61 Temperature maps by IR thermography measurements (devices at X_{d1} location) is probably due to a too large height of the "ZZ" tape, which could lead to an "overtripping" of the boundary layer. Indeed, for this X_{d1} location of the devices, the choice of the ZZ100 tape is better because its height is closer to the value of the boundary layer displacement thickness at this distance from the flat plate leading edge.

2.3.3 Effect of the Device Location

Figure 62 shows a comparison of oil flow visualizations from the ZZ100 tape device for the two selected X_{d1} and X_{d2} locations on the flat plate. It seems that the turbulator in the upstream position (X_{d1}) is producing more intense vortices, but this does not modify the flow topology in the interaction region.

Figure 63 shows a comparison of temperature maps obtained by IR thermography measurements from the ZZ100 tape device for the two selected X_{d1} and X_{d2} locations on the flat plate. The position of the turbulator has a slight effect on the temperature increasing during the boundary layer transition process. This is due to the fact that both locations of the "ZZ" tape device are chosen upstream of the interaction domain and of the boundary layer separation line (for the reference case). One sees on Fig. 63 that the temperature starts to sharply rise into the interaction region, at $X > 40$ mm, for the two device locations.

2.3.4 Schlieren Visualizations and Fourier Modes Decomposition

Schlieren photography is used to gain a better understanding of the spatial distribution of the unsteadiness of the flow by performing Fourier analysis: FFT is the most important discrete transform used to perform Fourier analysis. In image processing, the samples can be the values of pixels along a row or column of a raster image. The time resolved image sequence can be written as $I(i, j, n)$ where I is the light intensity of each image point (or pixel). In this study, i and j vary from 1 to 464 and 1 to 360, respectively, and n defines the snapshot number and varies from 1 to $N = 60{,}000$. For a given position (i, j), the time series that represent the evolution of light intensity at a given pixel of the field can be written as $p_{ij}(n)$. Assuming a linear correspondence between light intensity and density gradient, one can compute the Fourier transform of $p_{ij}(n)$ using an FFT algorithm with Hanning window function, 60 blocks with 50% overlap of 2048 images. Due to the limited amount of data samples, the spectrum has a resolution of $f = 17$ Hz and does not present any peak.

Figure 64 shows a comparison of the flow density gradients obtained by Fourier modes decomposition from the reference case and the controlled case by ZZ100 tape for the X_{d1} location on the flat plate (see Fig. 57a, b, respectively). These pictures are obtained by a Phantom V710 camera and 60,000 images are recorded at 35 kHz frame rate. The three selected frequencies ($f = 1, 5$ and 10 kHz) are chosen to provide information on shock-wave unsteadiness and mixing layer instabilities. One notices the presence of a low-frequency (around 1 kHz) unsteadiness into the shock pattern

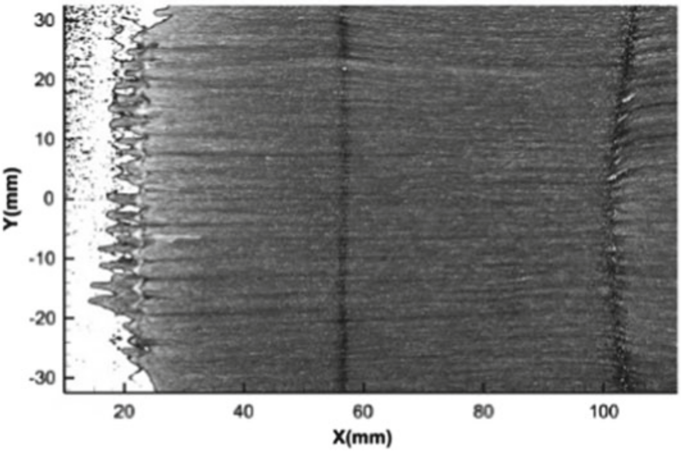

a) - control device at X_{d1} location

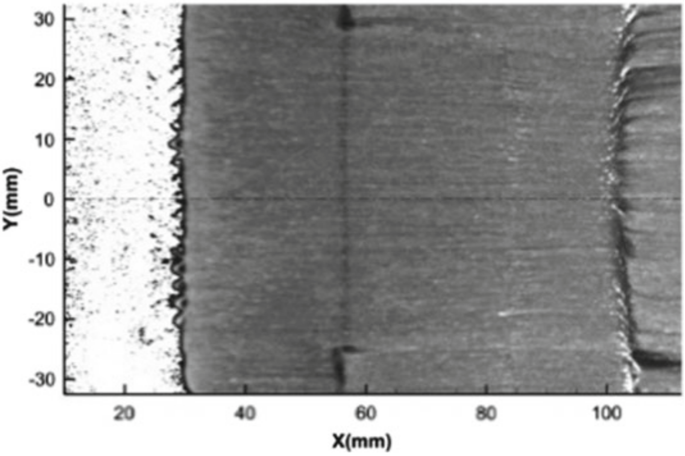

b) - control device at X_{d2} location

Fig. 62 Oil flow visualizations (for ZZ100 tape)

with a maximum of energy at the impact of the oblique shock on the boundary layer separation. So, the shock-waves seem to behave as a low-pass filter, displaying its maximum fluctuations at low frequencies. In the medium-frequency range (from 5 to 10 kHz), the circular structures can be related to the vortices generated by the Kelvin-Helmholtz instability, that are convected along the mixing layer in the downstream direction, behind the interaction region. However, these structures are already present upstream of the interaction domain when the control is applied (see Fig. 64b), which means that the "ZZ" tape device forced the transition and the boundary layer is turbulent upstream of the shock pattern.

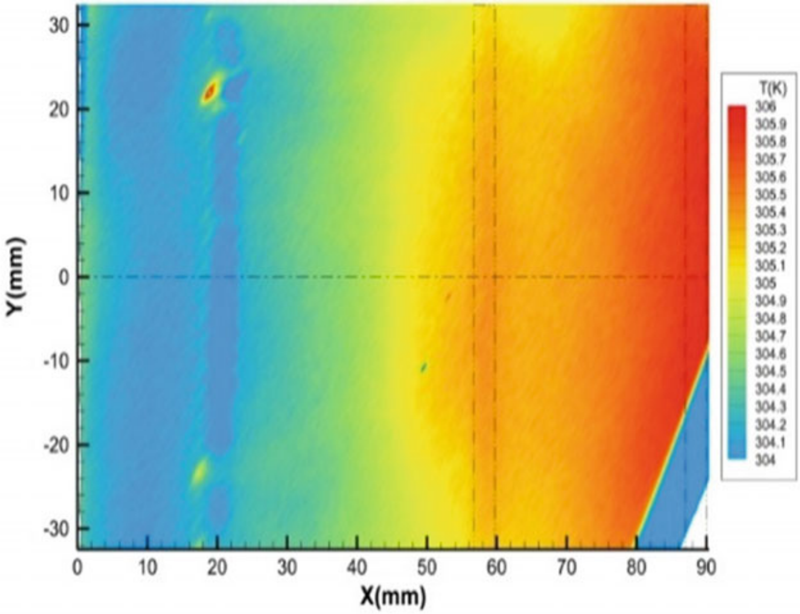

a) - control device at X_{d1} location

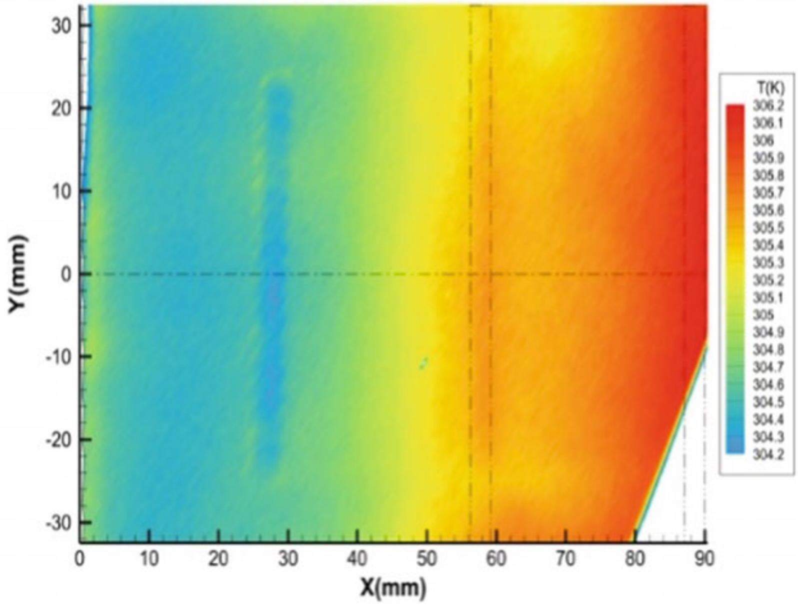

b) - control device at X_{d2} location

Fig. 63 Temperature maps by IR thermography measurements (for ZZ100 tape)

Fig. 64 Flow density gradients obtained by Fourier modes decomposition

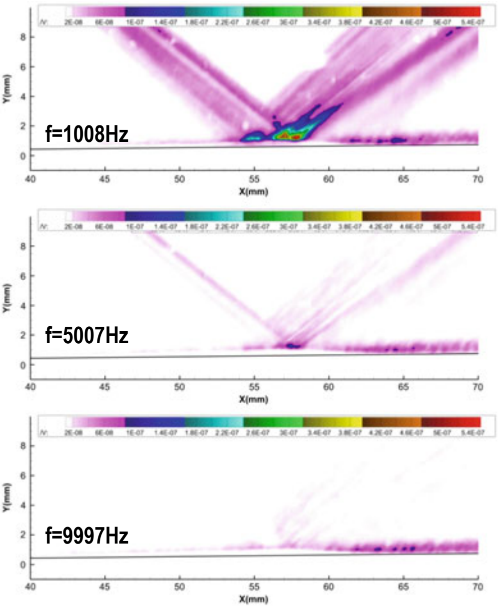

a) - reference case

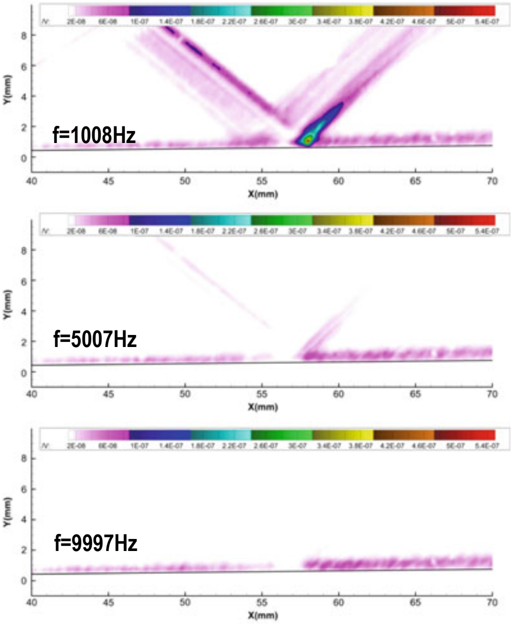

b) - control case:
ZZ100 tape

In our investigation the camera was equipped with a 12-bit colour depth sensor: the light intensity measured by each pixel is associated to a number between 0 and 4095. The available range is too small to describe at the same time both the strong density gradient due to the shock-wave and the small density variations in the mixing layer caused by the vortex shedding. For this reason, the image could present colour saturation on the shocks (black regions caused by the absence of light, see Fig. 57) or in the mixing layer (white region associated to too much light intensity). This problem can affect the results of the image processing, altering the Fourier modes by adding high-frequency energy in the saturated zone due to the signal truncation.

Finally, it was not possible to analyze flow unsteadiness for both very low-frequency (<500 Hz) and high-frequency (>15 kHz) modes.

2.3.5 Conclusions

Several parameters have been tested in order to optimize the effectiveness of control devices on the boundary layer transition, for a moderate oblique shock intensity configuration leading to a viscous interaction with separation. Both selected 3-D turbulators—a Cadcut device and a “ZZ” tape—forced the transition of the boundary layer and suppressed the separation region. The location of device with respect to the flat plate leading edge has a slight influence on the boundary layer transition process because the two tested positions of the turbulator are chosen far upstream of the interaction domain. Moreover, it is preferable to scale the height of device with the value of the boundary layer displacement thickness, where the control is applied, to avoid an “overtripping” of the boundary layer.

2.4 TUD

To study the effects of forced transition on a SWBLI, the oblique shock wave ($\theta = 3°$) is positioned at $x = 51$ mm, which under uncontrolled conditions corresponds to a strongly separated laminar interaction. The tripping devices are again installed and centred at $x = 40$ mm. Schlieren visualizations of the interaction were performed for the three tripping devices (Fig. 65), which may be compared to the uncontrolled interaction shown in Fig. 49 (chapter “WP-1 Reference Cases of Laminar and Turbulent Interactions”). The visualizations look very similar for the different tripping devices and suggest that flow separation has been eliminated in all cases. Notwithstanding the overall similarity in the three tripped cases, it may be observed that for the step the reflected shock region is slightly thicker for the other two trips. This might indicate a larger interaction region and a less effective tripping.

PIV measurements of the interaction region confirm that all trips indeed effectively remove the separation bubble. The PIV results will be further analysed in terms of the development of the integral boundary layer properties over the interaction.

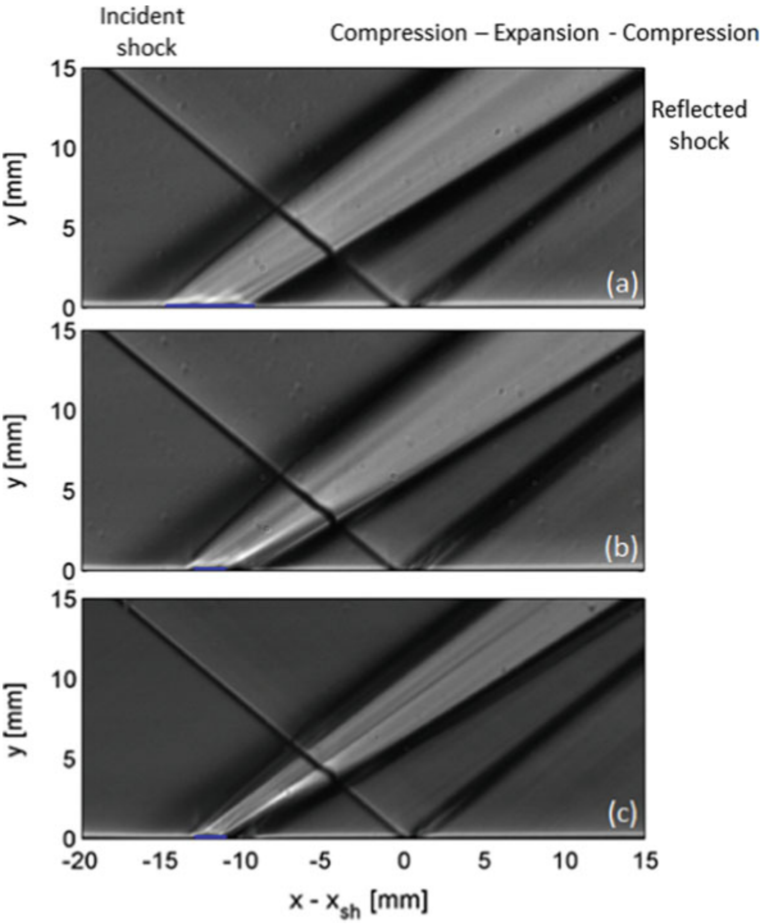

Fig. 65 Schlieren visualizations of the interaction for three tripping devices positioned 10 mm upstream of an impinging oblique shock wave ($x_{sh} = 51$ mm). **a** zig-zag strip; **b** step; **c** distributed roughness

First a comparison is made between the tripped boundary layer and the tripped interaction to assess the efficiency of the trip positioning on the interaction, as visualized by the incompressible shape factor (Fig. 66). Downstream of the trip the boundary layer quickly becomes turbulent, with an accompanying decrease of the shape factor, and at the shock impingement point (x = 51 mm) turbulent conditions have been established for all trips. Inside the interaction region the boundary layer velocity profile becomes less full, with the highest shape factors reached at the shock impingement location. For the step a maximum shape factor of 1.80 is reached in the interaction region, for the distributed roughness this is 1.72 while for the zig-zag strip a maximum shape factor of 1.61 is recorded. The flow downstream of the step is therefore concluded to be closest to separation in the interaction region, whereas

Fig. 66 Development of the incompressible shape factor H_i for the tripped boundary layer and tripped interaction: **a** zig-zag strip; **b** step; **c** distributed roughness

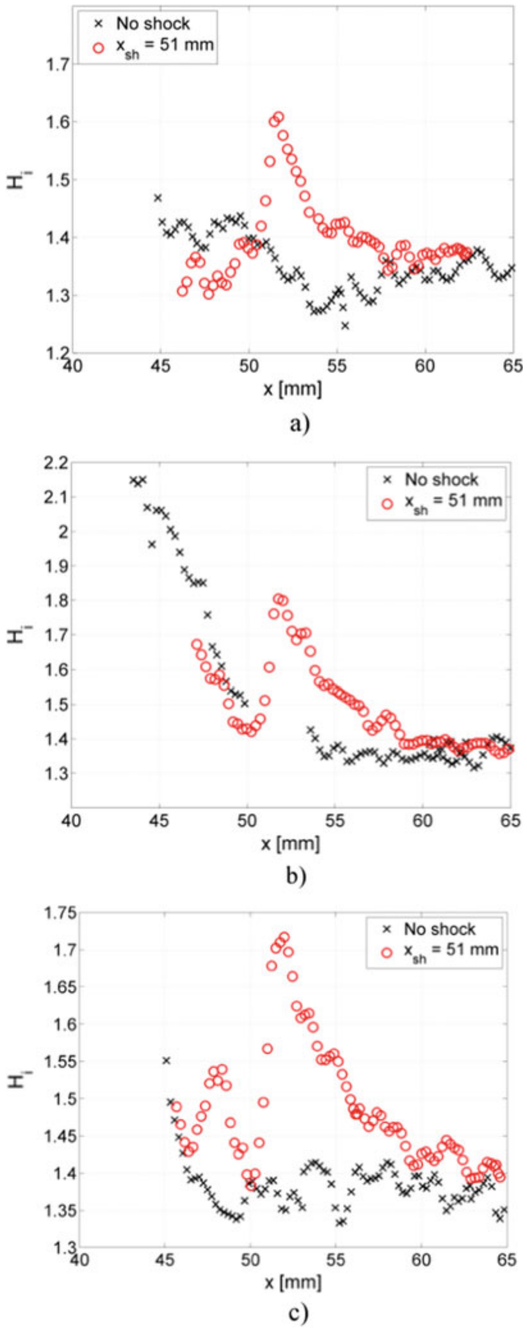

the flow downstream of the zig-zag strip is furthest removed from separation. The differences in shape factor are, however, relatively small.

Subsequently, a comparison is made between the tripped and untripped interactions (Fig. 67). For the untripped (laminar) interaction a large separation bubble is formed, which extends mostly upstream (ca. 8 mm) of the incident shock wave (see also Fig. 49, chapter "WP-1 Reference Cases of Laminar and Turbulent Interactions"). It was previously found that the boundary layer developing over the separation bubble remains in a quasi-laminar state up to the shock impingement location and transition only sets in after crossing the incident shock, resulting in a quick reattachment of the separated shear layer. This phenomenon is reflected in the development of the incompressible shape factor downstream of the interaction. The boundary layer for the untripped case recovers rapidly and within 5 mm of the shock wave it reaches the same level of fullness as recorded for the tripped interactions. Inside the interaction region the tripped cases display much lower values of the shape factor, consistent with the absence of a separation flow region.

From these results it is furthermore apparent that tripping the boundary layer upstream of the interaction results in a substantially thicker boundary layer downstream of the interaction. On average, tripping leads to an increase of the displacement thickness by 0.04 mm and an increase of the momentum thickness by 0.03 mm. In relative terms, this corresponds to a boundary layer that is ~50% thicker than the untripped boundary layer.

So, in summary it is confirmed that the transition control devices in the present configuration are able to remove the separation bubble, but do this at the price of having a substantially thicker boundary layer downstream of the interaction.

2.5 SOTON

2.5.1 Transition Location Effect on SWBLI

A quantitative comparison is made with the experiments conducted at the Institute of Applied Mechanics (ITAM) in Novosibirsk, Russia, for which large-eddy simulations (LES) simulations are performed due to the very large Reynolds number. The set of experiments by ITAM explores the effect of the unit Reynolds number Re_1 on the "perturbation zone" $\left(\mathrm{L}^*_{\mathrm{PER}}\right)$ for each type of interaction. By considering the flow quantities at the minimum distance from the wall that the particle image velocimetry (PIV) technology can accurately measure, the beginning of the perturbation zone is defined as the x-location where a 5% decrease of the streamwise velocity with respect to the inflow is recorded. A significant increase of the velocity indicates the end of the interaction. The experimental setup of ITAM for quantitative comparisons is summarised in Table 9.

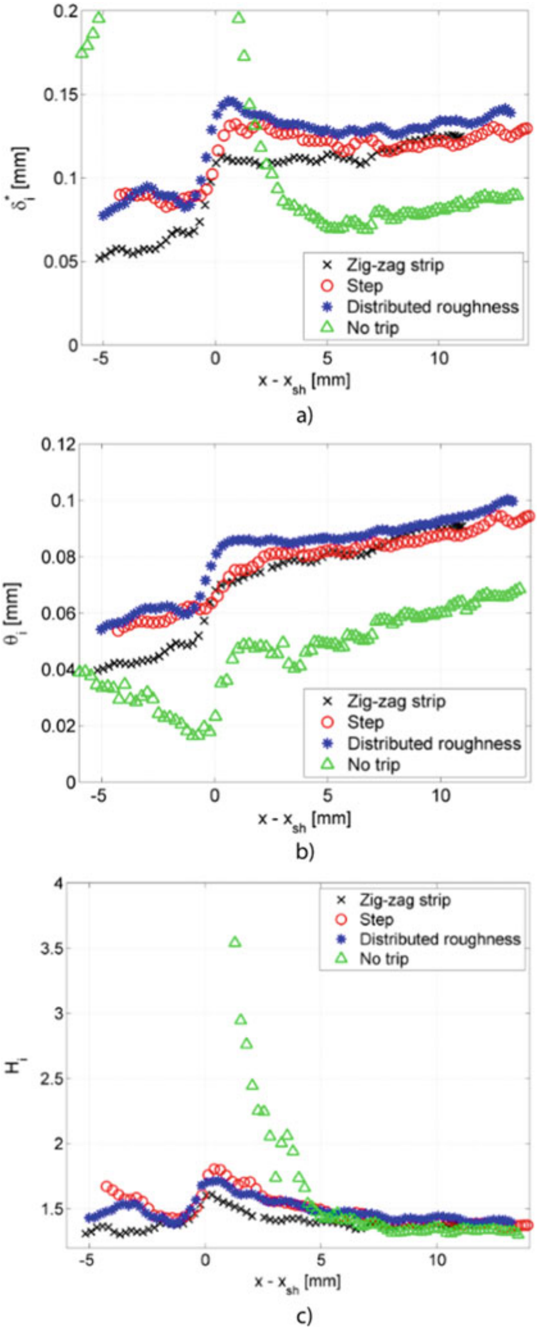

Fig. 67 Development of the boundary layer properties for the tripped and untripped interactions:
a incompressible displacement thickness δ_i^*,
b incompressible momentum thickness θ_i;
c incompressible shape factor H_i

Table 9 ITAM experimental case selected for comparisons

M	$T_0^*(K)$	$P_0^*(bar)$	$\mathrm{Re}_1(m^{-1})$	x_{imp}^*(mm)	Re $_{x_{imp}^*}$	$\theta(°)$	L_{PER}^*(mm)
1.4	289.1	0.65	$10.2 \cdot 10^6$	186.5	$1.77 \cdot 10^6$	3	20

2.5.2 Numerical Setup

The most relevant aspects of the numerical setup chosen to reproduce the experiments by ITAM are described here. Due to the large impingement Reynolds number, only LES calculations are carried out and the subgrid scale mixed-time scale (MTS) model is used. Due to computational resources limitations, only a transitional interaction. Details on the nature of the forcing, domain size and grid resolution are presented in the following sections. For consistency with the previous set of simulations the Mach number is $\mathrm{M} = 1.5$, but nosignificant effects are expected since the difference between experimental and numerical pressure ratios p_3/p_1 (downstream of the reflected shock to upstream of the incident shock) is about 1%. The numerical inflow is placed at $x_0 = 0.113$ m, $\delta_{1,0} = 2.78 \times 10^{-4}$ m. With a unit Reynolds number $\mathrm{Re}_1 = 10.18 \times 10^6$ m^{-1}, the corresponding Reynolds number based on the displacement thickness at the inlet is $\mathrm{Re}_{\delta_{1,0}} = 2835.84$. Inflow profiles are given by a similarity solution using the Illingworth transformation. The angle of the shock generator is either $\theta = 3$ or 4 deg and the oblique shock is introduced by the Rankine-Hugoniot jump relations at the top boundary. For all the selected cases, the free-stream temperature is $T_\infty^* = 197.93$ K and Sutherland's law is used to describe the variation of viscosity μ with temperature (Sutherland's constant temperature $\mathrm{TS}^* = 110.4$ K). The integration time step is $\Delta t = 0.025$ for all simulations, that are run until statistical convergence.

A complete summary of the cases is reported in Table 10. If no shock is introduced ($\theta = 0°$) the solution is a zero-pressure gradient (ZPG) growing boundary-layer, that is used to understand the transition scenario in the absence of an interaction. A sensitivity analysis on the shock strength is also performed.

The grid distribution in the wall-normal direction is stretched and clusters about 30% of the grid points within the boundary-layer at the inlet. The grid is stretched in the streamwise direction following a 10th-order polynomial distribution whose derivatives are continuous up to 4th-order. The spatial step size Δx continuously decreases from the inflow up to the transition location, after which uniform grids are used. The grid resolution is $\Delta x^+ = 22$, $\Delta z^+ = 18$ and $\Delta y_{wall}^+ = 1.11$. Details of the domain size, normalised with the displacement thickness at the inlet, and grid

Table 10 Numerical simulation cases summary. All the simulations are run at $\mathrm{M} = 1.5$ and $T_\infty^* = 197.93$ K

Case	Facility	Simulation	$\mathrm{Re}_{\delta_{1,0}^*}$	θ (°)	$\mathrm{Re}_{x_{\mathrm{imp}}^*} \times 10^6$	Interaction
IT-1	ITAM	LES-MTS	2835.84	0	–	–
IT-2	ITAM	LES-MTS	2835.84	4	1.77	Transitional
IT-3	ITAM	LES-MTS	2835.84	3	1.77	Transitional

Table 11 Numerical domain sizes and grid resolutions for each numerical simulation case

Case	$L_x \times L_y \times L_z$	$N_x \times N_y \times N_z$
IT-1	$335 \times 120 \times 31$	$1056 \times 240 \times 119$
IT-2	$335 \times 120 \times 31$	$1056 \times 240 \times 119$
IT-3	$335 \times 120 \times 31$	$1056 \times 240 \times 119$

resolution for all interactions are reported in Table 11. The boundary conditions applied to the computational domain are no-slip and fixed temperature conditions (with temperature equal to the laminar adiabatic wall temperature) at the wall and time-dependent fixed inlet (where the modal forcing is applied). To minimise the reflection of waves into the domain, an integral characteristic method is applied to the top boundary and a standard characteristic boundary condition at the outflow.

To mimic the broadband disturbances in the wind tunnel, the modal forcing technique is used, including a large number of stable and unstable modes. For all cases, 42 eigenmodes are calculated for each combination of $\omega = 0.02\text{: } 0.02\text{: } 0.12$ and $\beta = -0.6\text{: } 0.2\text{: } 0.6$. Since pairs of oblique modes are selected to construct the broadband modal disturbances, random phases are added to each mode in order to avoid any symmetry of the breakdown.

2.5.3 ZPG Boundary-Layer

The LES-MTS model is used to study a ZPG boundary-layer forced with the broadband modal forcing and forcing amplitude $A_o = 0.03$ (corresponding to a turbulence intensity at the inflow $\rho_{rms} = 0.15\%$). The time- and span-averaged skin friction distribution (a) and contours of time-averaged skin friction (b) and instantaneous streamwise velocity (c) are reported in Fig. 68. The forcing amplitude has been tuned to have the shock impingement location set by the experiments approximately halfway between the beginning ($Re_x = 1.4 \times 10^6$) and end ($Re_x = 1.9 \times 10^6$) of the transition region. The transition scenario shows long streaky structures that precede the breakdown, as shown in Fig. 69.

2.5.4 Intermittency Calculation

The first and second time derivatives of the skin friction distribution are used to calculate the span averaged intermittency distribution in Fig. 71 (black solid line with error bars for the threshold f sensitivity). In agreement with the skin friction and shape factor distributions the region with $0 < \Gamma < 1$ extends between $1.4 \times 10^6 < Re_x < 1.9 \times 10^6$. The hyperbolic tangent (red solid line) fitted curve seems to better represent the intermittency distribution than the Narasimha [29] (blue solid line) approximation.

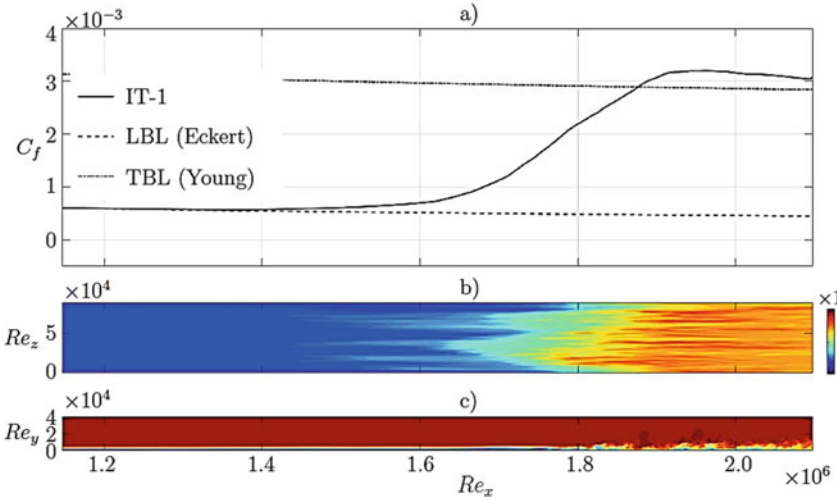

Fig. 68 **a** Time- and span-averaged skin friction distribution for the ZPG boundary-layer (black solid line) along with laminar (dashed-dotted black) and turbulent (dashed black) boundary-layer distributions by [9] and [10], respectively; contours of time-averaged skin friction (**b**) and instantaneous streamwise velocity (**c**). The extent of the transitional region is also confirmed by plotting the displacement thickness (**a**) and shape factor (**b**) distributions in Fig. 70, calculated with the compressible (solid black line) and incompressible (dashed black line) formulations

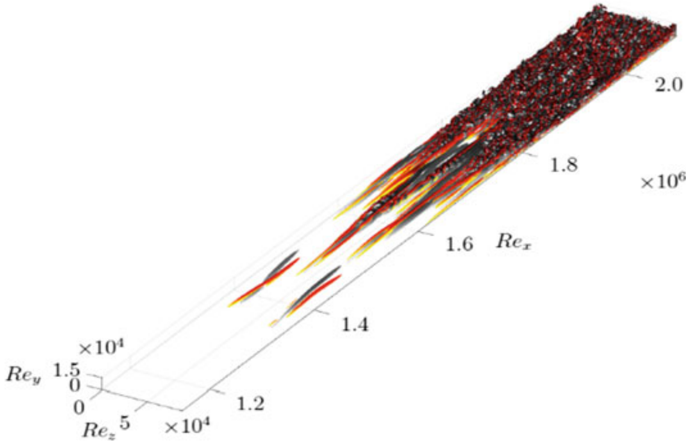

Fig. 69 Transition visualisation. Iso-surfaces of the wall-normal vorticity for the levels $\omega_y = +0.075$ (red) and $\omega_y = -0.075$ (black) and coloured with the streamwise velocity

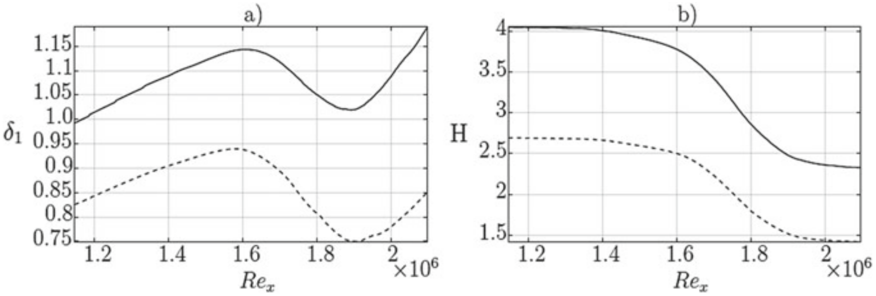

Fig. 70 Time- and span-averaged displacement thickness (**a**) and shape factor (**b**) distributions calculated with the incompressible (dashed lines) and compressible (solid lines) formulations

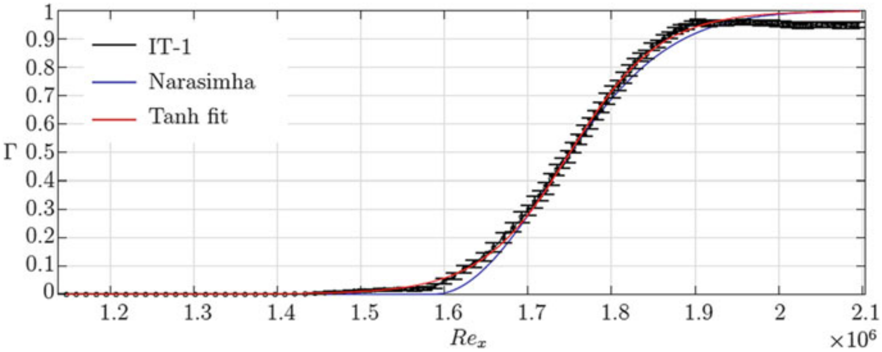

Fig. 71 DNS span averaged intermittency distribution (black solid line with error bars due to the threshold sensitivity) for the ZPG boundary-layer at $Re_{\delta_{1,0}} = 2835.84$ (case IT-1). Narasimha (blue solid line) and hyperbolic tangent (red solid line) fit curves are also plotted

2.5.5 SWBLI for Transitional Interactions

The transitional interaction at $Re_{x_{imp}} = 1.77 \times 10^6$ with $\theta = 4°$ (case IT-2) and $\theta = 3°$ (case IT-3) from the ITAM experiments are considered here for comparison. Figure 72 shows the skin friction (a), displacement thickness (b) and shape factor (c) distributions for the ZPG (solid black line), $\theta = 4°$ (blue solid line) and $\theta = 3°$ (red solid line) cases. Similarly to what happened for the previous setup at $Re_{\delta_{1,0}} = 1971.07$ (ONERA case), the presence of the shock causes breakdown to turbulence at the shock impingement location. The interaction size and boundary-layer thickness increases for increasing shock strength but the boundary-layer remains attached.

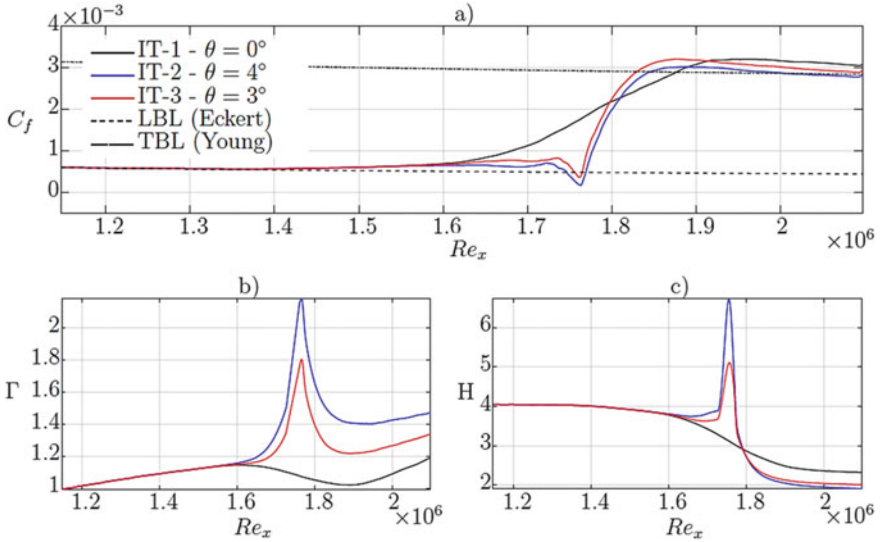

Fig. 72 Time- and span-averaged skin friction (**a**), displacement thickness (**b**) and shape factor (**c**) distributions for θ = 4° (blue solid line), θ = 3° (red solid line) and ZPG (black solid line—case IT-1). Laminar (dashed-dotted black) and turbulent (dashed black) boundary-layer distributions by [9] and [10], respectively

2.5.6 Intermittency Calculation

Figure 73 shows the span averaged intermittency distributions for the ZPG (black solid line), θ = 3° (red solid line) and θ = 4° (blue solid line) cases. Downstream

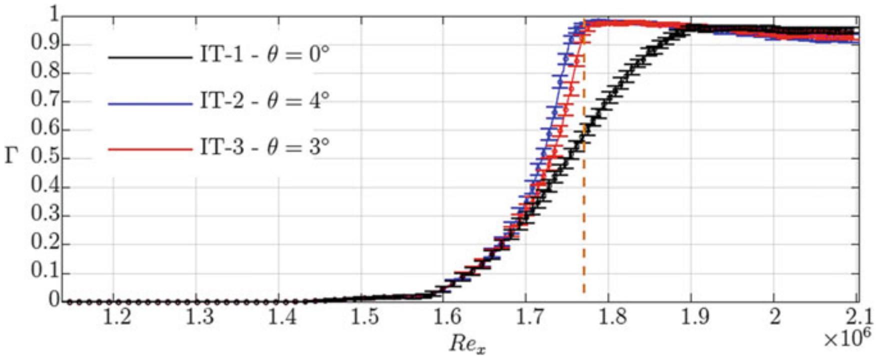

Fig. 73 Span averaged intermittency distributions (with error bars due to the threshold sensitivity) for the transitional case with θ = 4° (blue solid line—case IT-2) and θ = 3° (red solid line—case IT-3). The ZPG boundary-layer (black solid line—case IT-1) is also plotted. The vertical orange dashed line indicates the shock impingement location

of the interaction the boundary-layer becomes turbulent and the intermittency distribution deviates from the ZPG case and sharply jumps towards unity. Differently from the sensitivity study at lower Reynolds number, the effects of the shock strength on the intermittency distribution downstream of the interaction are negligible. The differences are more pronounced upstream of the impingement location ($\mathrm{Re}_x\mathrm{imp} = 1.77 \times 10^6$). The size of the interaction increases with the shock strength and the effects are visible for a larger upstream extent. Thus, the case with the weaker shock follows the ZPG solution for longer before deviating, however still reaching fully turbulent conditions at the impingement.

2.5.7 Experimental Comparisons

A comparison between the case at $\theta = 4°$ is done with the experimental PIV measurements performed by ITAM on a mean streamwise velocity x-y plane in Fig. 74. Although very qualitative, the comparison presents similar features: the boundary-layer visibly thickens after the shock and no recirculation region is detected. In order to compare the LES results with the experiments in terms of interaction length, a definition similar to the one provided by ITAM is used to calculate the perturbation zone. The beginning of the interaction region is taken as the location where the skin friction distribution deviates from the laminar solution by 5%. The interaction ends where a significant increase of the skin friction distribution is recorded. By following this definition, the perturbation length is LPER = 22 and 24 mm for $\theta = 3$ and 4°, respectively, in reasonable agreement with the value measured at $\theta = 3°$ by ITAM (LPER = 20 mm), as reported in Table 9. However, the differences in the definitions of the interaction region still do not allow a satisfactory comparison. The lack of complete experimental measurements makes the search of more appropriate definitions currently out of scope, but the width of the peaks in the displacement thickness or shape factor distributions, or the streamwise extension where the intermittency is between 0 and 1, could be used for quantifying the interaction lengths.

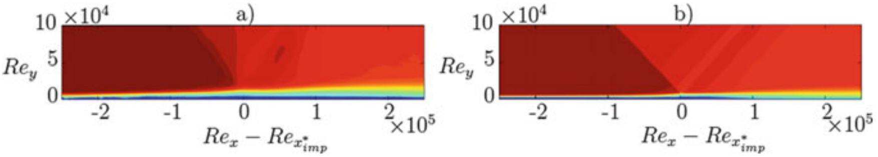

Fig. 74 Contours of instantaneous streamwise velocity from PIV measurements by ITAM (**a**) and LES-MTS (**b**). Levels between 0.0–1.0. (With permission of A. A. Sidorenko and P. A. Polivanov at the Institute of Theoretical and Applied Mechanics from Novosibirsk State University)

2.5.8 Reynolds Number Effect on the SWBLI

The present LES-MTS simulations for the ZPG and transitional SWBLI at θ = 4° are compared for the previous sets of calculations at $\mathrm{Re}_{\delta_{1,0}} = 1971.07$ (ONERA setup). Figure 75 summarises the results in terms of time- and span-averaged skin friction (a), displacement thickness (b) and shape factor (c) distributions. The main features of the transitional interaction are very similar and the effect of the Reynolds number are small. In both cases, the boundary-layer becomes turbulent downstream of the shock impingement and proportionally thickens by a factor of 1.5. The minimum in the skin friction distribution is higher for higher Reynolds number but the interaction length is practically unchanged.

The span-averaged intermittency distributions in Fig. 77 also show very similar features. The effect of the interaction on the region upstream of the impingement is gradual with respect to the ZPG cases and the extent of the upstream boundary-layer portion that is affected by the shock is in agreement with the size of the interaction. Despite differences in the transition breakdown scenarios, these results suggest a scalability of the main features of the interaction with the Reynolds number. However,

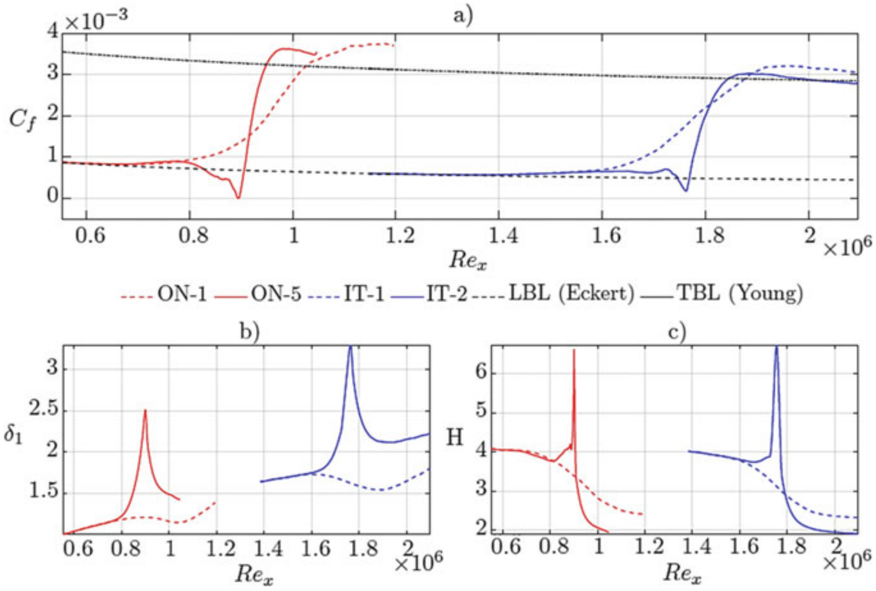

Fig. 75 Time- and span-averaged skin friction (**a**), displacement thickness (**b**) and shape factor (**c**) distributions for the ZPG (red dashed line—case ON-1) and θ = 4° (red solid line—case ON-5) cases at $\mathrm{Re}_{\delta_{1,0}} = 1971.07$ and the ZPG (blue dashed line—case IT-1) and θ = 4° (blue solid line—case IT-2) cases at $\mathrm{Re}_{\delta_{1,0}} = 2835.84$. Laminar (dashed-dotted black) and turbulent (dashed black) boundary-layer distributions by [9] and [10], respectively

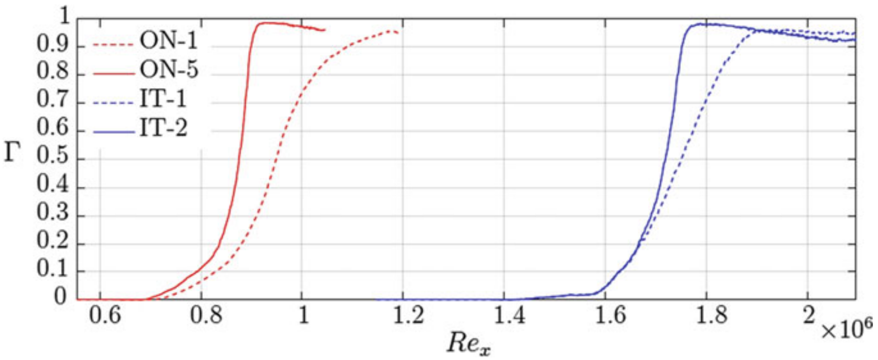

Fig. 76 Span averaged intermittency distributions for the ZPG (red dashed line—case ON-1) and $\theta = 4°$ (red solid line—case ON-5) cases at $Re_{\delta_{1,0}} = 1971.07$ and the ZPG (blue dashed line—case IT-1) and $\theta = 4°$ (blue solid line—case IT-2) cases at $Re_{\delta_{1,0}} = 2835.84$

Fig. 77 Coordinate system used to define unit vectors

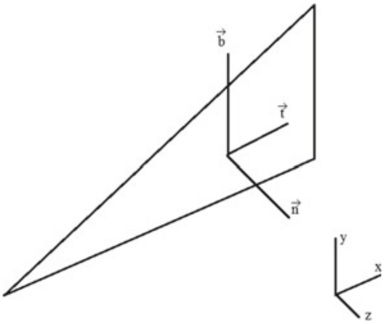

although not tested here, it is the authors' opinion that for the laminar cases the interaction region would significantly decrease in size for increasing shock impingement Reynolds number.

2.5.9 Conclusions

The transitional interaction is close to a marginal separation. The shock wave is strong and the boundary-layer becomes turbulent at the shock impingement location. Apart from boundary-layer thickness effects, similar results are obtained when the shock wave is weaker. For the same kind of interaction (transitional), the impingement Reynolds number has moderate effects apart from a larger boundary-layer thickening. Qualitative agreement is obtained with the experiments when LES calculations are compared with ITAM PIV measurements.

3 Physical Modelling of the Control Devices

3.1 IoA

Overview of BAY model of vortex generator

Implementation of numerical modelling of the effects of BAY model of thin-plate vortex generator

In BAY method developed by Bender et al. [30] the vortex generator (VG) is replaced by subdomain placed in original location of vortex generator, where the force distribution is applied. The force is introduced as momentum source by a source term in momentum balance equations. The vorticity is generated by force which depends on local velocity values and vortex generator's geometry and spatial orientation. The lifting force source term, L_i (3) acting at grid point i, is added to the governing discretized finite volume momentum (27) and energy (2) equations:

$$\Delta V_i \frac{\Delta \rho \overrightarrow{u_i}}{\Delta t} = \sum_j \overrightarrow{F_M} \Delta S + \overrightarrow{L_i} \tag{28}$$

$$\Delta V_i \frac{\Delta \rho \vec{E}}{\Delta t} = \sum_j \overrightarrow{F_E} \Delta S + \overrightarrow{u_i}\, \overrightarrow{L_i} \tag{29}$$

The source term $\overrightarrow{L_i}$ is a function of the lifting force caused by the vortex generator and is corrected for losses due to deviation of the flow from the vortex generator surface. F_M are inviscid and viscous fluxes in momentum equations. F_E are inviscid and viscous fluxes in energy equation. ΔS is the area of cell face *j*. The side force is approximated by Eq. (30).

$$\mathbf{L_i} = c_{VG} S_{VG} \frac{\Delta v_i}{v_m} \propto \rho u^2 \mathbf{l} \tag{30}$$

c_{VG} is relaxation parameter which controls the strength of the side force and consequently the intensity with which the local velocities align with the vortex generator, S_{VG} is plan parallel area of vortex generator, V_i is the volume of the cell where the force is calculated, V_m is the sum of volumes of cells where the force term is applied, α is the angle of local velocity **u** to the Vortex Generator, **l** is unit vector on which the side force acts.

The coordinate system is shown in the Fig. 77.

In the Fig. 77. the directions of x, y and z axes aren't parallel to t, b, n axes which represent vortex generator's vector due to Vortex Generator's angle of inclination and angle of attack. Vector **n** is the unit vector normal to vortex generator planform (36), **b** is the unit vector in the direction of the span of the VG (37) and **t** is unit vector tangential to the vortex generator planform and normal to **b** (38). The position of VG and its orientation are user inputs to User Defined Function in ANSYS Fluent commercial code.

Using a small angle approximation there is

$$\mathbf{l} = \frac{\mathbf{u}}{|\mathbf{u}|} \times \mathbf{b} \tag{31}$$

$$\propto \approx \sin\alpha = \cos\left(\frac{\pi}{2} - \alpha\right) = \frac{\mathbf{u} \cdot \mathbf{n}}{|\mathbf{u}|} \tag{32}$$

The final equation is multiplied by term (33)

$$\frac{\mathbf{u} \cdot \mathbf{t}}{|\mathbf{u}|} \tag{33}$$

which represents losses of side force due to high angles of attack. The final expression for side force (34) according to Bender et al. is as follows:

$$\mathbf{L_i} = \mathrm{c_{VG}S_{VG}}\frac{\Delta \mathrm{V_i}}{\mathrm{V_m}}\rho(\mathbf{u} \cdot \mathbf{n})(\mathbf{u} \times \mathbf{b})\left(\frac{\mathbf{u} \cdot \mathbf{t}}{|\mathbf{u}|}\right) \tag{34}$$

In the Eq. (35) **u** means local velocity vector

$$\mathbf{u} = [\mathrm{u, v, w}] \tag{35}$$

Velocities u, v, w are the local velocities in the cells where momentum source is applied. Velocities are accessed by the $\mathrm{C_{U(c,t)}}$, $\mathrm{C_{V(c,t)}}$, $\mathrm{C_{W(c,t)}}$ flow variable macros in the cells using User-Defined Functions. The unit vectors **n**, **b**, **t** in x, y and z directions are as follows

$$\mathbf{n} = \left[\mathrm{n_x, n_y, n_z}\right] \tag{36}$$

$$\mathbf{b} = \left[\mathrm{b_x, b_y, b_z}\right] \tag{37}$$

$$\mathbf{t} = \left[\mathrm{t_x, t_y, t_z}\right] \tag{38}$$

$$\begin{aligned}\mathbf{L_i} &= \mathrm{c_{VG}S_{VG}}\frac{\Delta \mathrm{V_i}}{\mathrm{V_m}}\rho(\mathbf{u} \cdot \mathbf{n})(\mathrm{u} \times \mathrm{b})\left(\frac{\mathrm{u} \cdot \mathrm{t}}{|\mathrm{u}|}\right) \\ &= \mathrm{c_{VG}S_{VG}}\frac{\Delta \mathrm{V_i}}{\mathrm{V_m}}\rho\left(\mathrm{u} \cdot \mathrm{n_x} + \mathrm{v} \cdot \mathrm{n_y} + \mathrm{w} \cdot \mathrm{n_z}\right) \\ &\quad \cdot \left(\left[\mathrm{v} \cdot \mathrm{b_z} - \mathrm{w} \cdot \mathrm{b_y}, \mathrm{w} \cdot \mathrm{b_x} - \mathrm{u} \cdot \mathrm{b_z}, \mathrm{u} \cdot \mathrm{b_y} - \mathrm{v} \cdot \mathrm{b_x}\right]\right) \cdot \left(\frac{\mathrm{u} \cdot \mathrm{t_x} + \mathrm{v} \cdot \mathrm{t_y} + \mathrm{w} \cdot \mathrm{t_z}}{|\mathrm{u}|}\right)\end{aligned} \tag{39}$$

The final expression for the side forces in cartesian coordinate system is as follows:

$$\mathrm{L_x} = \mathrm{c_{VG}S_{VG}}\frac{\Delta \mathrm{V_i}}{\mathrm{V_m}}\rho\left(\mathrm{u}\cdot\mathrm{n_x}+\mathrm{v}\cdot\mathrm{n_y}+\mathrm{w}\cdot\mathrm{n_z}\right)\left(\mathrm{v}\cdot\mathrm{b_z}-\mathrm{w}\cdot\mathrm{b_y}\right)\left(\frac{\mathrm{u}\cdot\mathrm{t_x}+\mathrm{v}\cdot\mathrm{t_y}+\mathrm{w}\cdot\mathrm{t_z}}{|\mathbf{u}|}\right) \tag{40}$$

$$\mathrm{L_y} = \mathrm{c_{VG}S_{VG}}\frac{\Delta \mathrm{V_i}}{\mathrm{V_m}}\rho\left(\mathrm{u}\cdot\mathrm{n_x}+\mathrm{v}\cdot\mathrm{n_y}+\mathrm{w}\cdot\mathrm{n_z}\right)\left(\mathrm{w}\cdot\mathrm{b_x}-\mathrm{u}\cdot\mathrm{b_z}\right)\left(\frac{\mathrm{u}\cdot\mathrm{t_x}+\mathrm{v}\cdot\mathrm{t_y}+\mathrm{w}\cdot\mathrm{t_z}}{|\mathbf{u}|}\right) \tag{41}$$

$$\mathrm{L_z} = \mathrm{c_{VG}S_{VG}}\frac{\Delta \mathrm{V_i}}{\mathrm{V_m}}\rho\left(\mathrm{u}\cdot\mathrm{n_x}+\mathrm{v}\cdot\mathrm{n_y}+\mathrm{w}\cdot\mathrm{n_z}\right)\left(\mathrm{u}\cdot\mathrm{b_y}-\mathrm{v}\cdot\mathrm{b_x}\right)\left(\frac{\mathrm{u}\cdot\mathrm{t_x}+\mathrm{v}\cdot\mathrm{t_y}+\mathrm{w}\cdot\mathrm{t_z}}{|\mathbf{u}|}\right) \tag{42}$$

The Eqs. (40), (41) and (42) are the equations directly implemented in the User-Defined Functions. After implementation of momentum sources as source terms in User-Defined Functions in ANSYS-FLUENT code the appropriateness of this implementation was checked. In order to simplify the equations and reduce computational cost and overcome the necessity of calculating the ΔV_i at every iteration it was assumed as 1. This simplification was taken into account during BAY model calibration.

3.1.1 BAY Model of Air-Jet Vortex Generator

In order to overcome difficulty with generating meshes of the air jet vortex generator at every investigated location the new source term model of air jet vortex generator was proposed. This model works by adding momentum source term to Reynolds-Averaged Navier-Stokes equations in Fluent commercial code. The model may be calibrated with respect to obtain the best circulation values agreement in location, where vortex is fully formed. The calibration with respect to circulation values is enough, because it is impossible to calibrate with one model constant more than one flow parameter, for example intermittency. Additionally, BAY model predicts in proper way other flow parameters such as turbulent kinetic energy and shear stresses as predicted by grid-resolved vortex generator if BAY model constant is calibrated with respect to circulation only, which will be shown in the plots.

3.1.2 Numerical Method and Flow Configuration

In the Fig. 78. is shown schematic of JVG orientation used in computations. The skew angle of a jet (the angle between main flow direction and the direction of jet blow) α is equal to 90° and the injection angle of a jet θ is equal to 45°.

Fig. 78 Schematic of JVG orientation

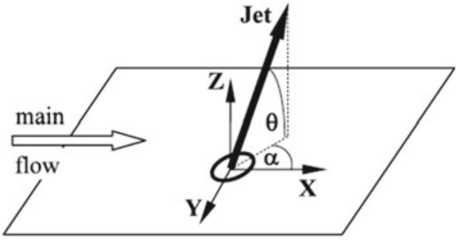

3.1.3 Source Term Model of JVG—New Approach

A new ABAY model is a generalization of BAY model on JVG models. The name jBAY is reserved by Jirasek [30], who proposed a model of thin-plate vortex generator defined by grid points. A new approach to model JVG doesn't consider MFR_{jet}, because the mass flow rate in grid-resolved AJVG is regulated by total pressure at inlet of AJVG. The total pressure at jet inlet is set as in main flow. The new ABAY model takes into account the directional components of two unit vectors (**b** and **t**) of three (**n**, **b** and **t**) proposed originally by Bender et al. and assumes that vortex generator's angle of attack is equal to 1, because skew and injection angle of jet is just defined by unit vectors **b**, **t** orientation. The unit vectors values were used as presented in the Table 12 which correspond to vortex generator's orientation as mentioned above. In the Fig. 79 with the dashed edge is drawn the shape of modelled JVG.

Additional reason of doing assumption of $\alpha = 1$ is that the u velocity gradient in boundary layer is very high and it is difficult to control body force in this region. The volume of cell V_i is also assumed as 1 in order to reduce computational cost of calculating cell volume. The body force used in computations is (40). Cells are selected in the place of inlet of jet to the main flow and the height of selected cells is in described case the 1/10 of boundary layer height.

Table 12 Parameters of unit vectors used in model of JVG

Parameter	Value
n_x	0
n_y	0.5
n_z	0.5
t_x	−1
t_y	0
t_z	0
b_x	0
b_y	0.5
b_z	−0.5

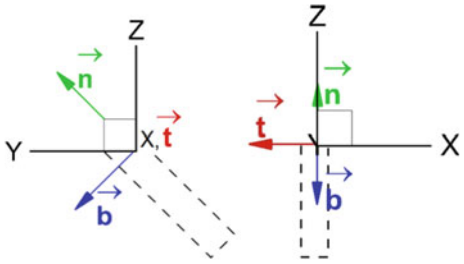

Fig. 79 Representation of unit vectors used in new model of JVG

$$L_i = c_{VG} S_{VG} \frac{1}{V_m} \rho\alpha \left(\frac{\mathbf{u}}{|\mathbf{u}|} \times \mathbf{b}\right)\left(\frac{\mathbf{u}\cdot\mathbf{t}}{|\mathbf{u}|}\right) \tag{43}$$

S_{VG} is the area of the jet inlet with respect to the diameter of 1 mm. The V_m is the sum of volume of cells, where source term is applied, which is the area of the jet inlet multiplied by the height of model of vortex generator, which may be assumed as $H = 1/10$ of boundary layer thickness. The density ρ is calculated in every volume cell.

The cell is selected in the model of vortex generator if cell's centroid is in the region selected by constraints (44) and (45).

$$X^2 + Y^2 < D^2 \tag{44}$$

$$Z < H \tag{45}$$

where D is the diameter of jet inlet and H is the height of cells, where source term is applied.

In the Fig. 80. are presented the skin-friction coefficient distributions behind JVG modelled in the computational domain in shape of cuboid, which modelled the measurement chamber of wind-tunnel located in Institute of Fluid-Flow Machinery in Gdansk. In the Fig. 80. is presented the skin-friction coefficient at $X = 0.048$ m in the left plot and in the $X = 0.108$ m in the right plot compared with experimental data. The AJVG is located at $X = 0$ m. Good agreement of plots, especially in shape of distribution. In the region, where is the influence of the AJVG, the values are a bit different. This difference may be caused by different intensity of vortex calculated in CFD and measured in experiment, different location of vortex near wall, which influences the local velocity gradients and measurement error in experiment.

During numerical simulations the new model of JVG based on lifting-force theory was implemented to predict effects induced by grid-resolved JVG. It has been proven that new ABAY model of AJVG is is sufficiently precise to predict such flow parameters such as x-velocities, skin-friction coefficients and circulation as close as grid-resolved air-jet vortex generator under conditions that the BAY model c_{VG} is calibrated, the **b** and **t** vectors are defined properly and cells, where source term is applied are properly chosen. ABAY model is a good candidate model to predict flow

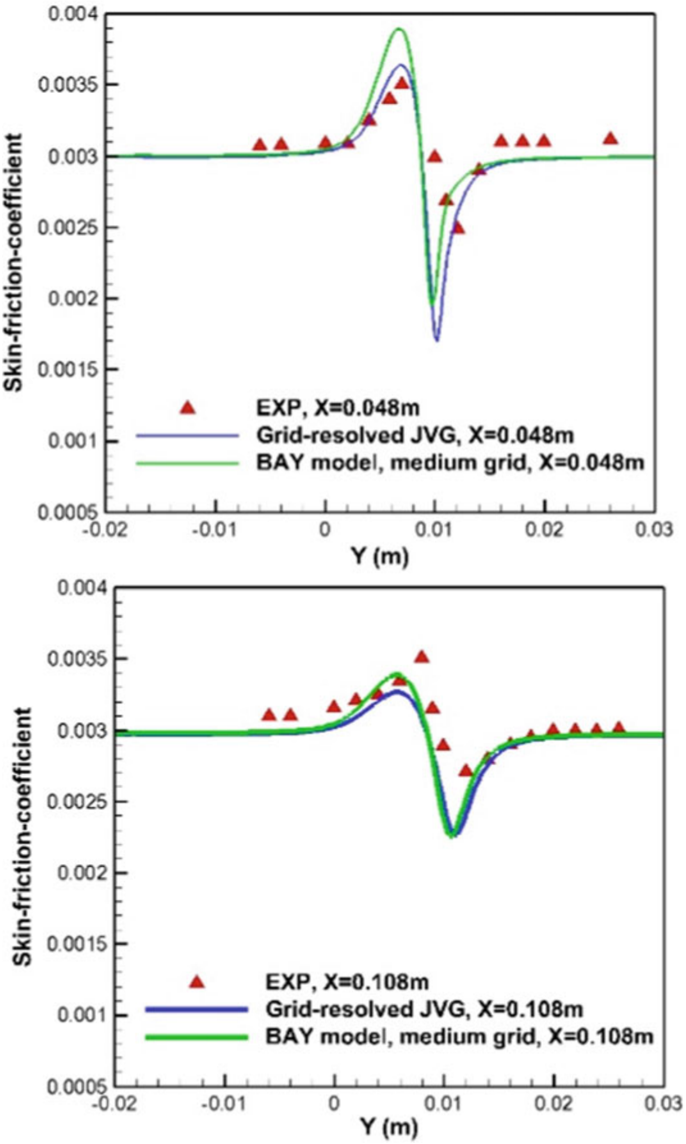

Fig. 80 Skin-friction coefficient plot on tunnel wall surface in the X = 0.048 m (left plot) and X = 0.108 m (right plot)

parameters as grid-resolved AJVG using the ANSYS Fluent solver with implementation by system of User Defined Functions. The disadvantage of the BAY model of AJVG is the fact that doesn't predict flow parameters in the close vicinity of AJVG hole (around 10 mm for a hole of diameter D = 1 mm) in the proper way due to different principle of work. The second disadvantage of the ABAY model is the fact, that it doesn't work in an asymptotic mode for large model constants C_{VG} as original BAY model. It implies the necessity of generation of mesh with grid-resolved Air Jet Vortex Generator (AJVG) and the necessity for calibration of the model constant. The effects in locations further from AJVG hole- from distance of 5 mm and higher the effects of AJVG are predicted in good agreement with grid-resolved AJVG. The advantage of BAY model is the fact, that during calculations it is possible to choose the cells, where source term is applied without need to generate new computational mesh. This model is also grid independent. The other advantage is the fact that using coarse mesh it is possible to obtain solution faster and with approximation error less than 10% in the distance to 5 cm and less than 5% in the distance to 10 cm. The best method to calibrate BAY model is to choose a slice far enough from AJVG—around 5 diameters of AJVG, because at location far enough from AJVG the vortices are fully formed and then using linear approximation method select proper c_{VG} constant.

References

1. P.A. Polivanov, A.A. Sidorenko, A.A. Maslov, Artificial turbulization of the supersonic boundary layer by dielectric barrier discharge, in *2014 29th Congress International Council of Aeronautical Sciences ICAS* (2014) pp. 1–10
2. R.H.M. Giepman, R. Louman, F.F.J. Schrijer, B.W. van Oudheusden, Experimental study into the effects of forced transition on a shock-wave/boundary-layer interaction. AIAA J. **54**(4), 1313–1325 (2016)
3. C.J. Gibbings, J.M.B. Ingham, D. Johnson, Flow in a Supersonic Jet expanding from a Convergent Nozzle (2002)
4. W. Shyy, B. Jayaraman, A. Andersson, Modeling of glow discharge-induced fluid dynamics. J. Appl. Phys. **92**(11), 6434–6443 (2002)
5. C.-C. Wang, S. Roy, Three-dimensional simulation of a microplasma pump. J. Phys. D. Appl. Phys. **42**(18), 185206 (2009)
6. M. Forte, J. Jolibois, J. Pons, E. Moreau, G. Touchard, M. Cazalens, Optimization of a dielectric barrier discharge actuator by stationary and non-stationary measurements of the induced flow velocity: application to airflow control. Exp. Fluids **43**(6), 917–928 (2007)
7. R.H.M. Giepman, M. Kotsonis, On the mechanical efficiency of dielectric barrier discharge plasma actuators. Appl. Phys. Lett. **98**(22) (2011)
8. B. Jayaraman, W. Shyy, Modeling of dielectric barrier discharge-induced fluid dynamics and heat transfer. Prog. Aerosp. Sci. **44**(3), 139–191 (2008)
9. E.R.G. Eckert, Engineering relations for friction and heat transfer to surfaces in high velocity flow. J. Aeronaut. Sci. **22**, 585–587 (1955)
10. A.D. Young, Boundary layers—AIAA education series. Blackwell Sci. (1989)
11. H.L. Dryden, Review of published data on the effect of roughness on transition from laminar to turbulent flow. J. Aeronaut. Sci. **20**(7), 477–482 (1953)
12. E. Reshotko, Is Retheta/Me a Meaningful Transition Criterion?. AIAA J. **45**(7), 1441–1443 (2007)

13. C.R. Smith, M.S. Acarlar, A study of hairpin vortices in a laminar boundary layer. Part 1. Hairpin vortices generated by hemisphere protuberances. J. Fluid Mech. **175**, 1–41 (1987)
14. K.P. Klebanoff, W. Cleveland, K.D. Tidstrom, On the evolution of a turbulent boundary layer induced by a three-dimensional roughness element.pdf. **237**, 101–187 (1992)
15. F.G. Ergin, E.B. White, Unsteady and transitional flows behind roughness elements. AIAA J. **44**(11), 2504–2514 (2006)
16. G. Groskopf, M.J. Kloker, O. Marxen, Bi-global secondary stability theory for high-speed boundary-layer flows, in *Proceedings of the 2008 Summer Program*, no. 1994 (2008) pp. 55–72
17. M. Bernardini, S. Pirozzoli, P. Orlandi, Compressibility effects on roughness-induced boundary layer transition. Int. J. Heat Fluid Flow **35**, 45–51 (2012)
18. D.P. Rizzetta, M.R. Visbal, Direct numerical simulations of flow past an array of distributed roughness elements. AIAA J. **45**(8), 1967–1976 (2007)
19. E.R. Van Driest, C.B. Blumer, Boundary-layer transition at supersonic speeds—three-dimensional roughness effects (spheres). J. Aerosp. Sci. **29**(8), 909–916 (1962)
20. P. Balakumar, Receptivity of a supersonic boundary layer to acoustic disturbances. AIAA J. **47**(5), 1069–1078 (2009). https://doi.org/10.2514/1.33395
21. O. Marxen, G. Iaccarino, E.S.G. Shaqfeh, Disturbance evolution in a mach 4.8 boundary layer with two-dimensional roughness-induced separation and shock. J. Fluid Mech. **648**, 435–469 (2010)
22. J.A. Redford, N.D. Sandham, G.T. Roberts, Compressibility effects on boundary-layer transition induced by an isolated roughness element. AIAA J. **48**(12), 2818–2830 (2010)
23. S.P. Schneider, Effects of Roughness on Hypersonic Boundary-Layer Transition. AIAA J. **45**(2), 255–276 (2013)
24. T. Colonius, S.K. Lele, Computational aeroacoustics: progress on nonlinear problems of sound generation. Prog. Aerosp. Sci. **40**(6), 345–416 (2004)
25. J. Delery, J.G. Marvin, Shock wave - boundary layer interactions. AGARDograph **280** (1986)
26. S. Pirozzoli, Generalized conservative approximations of split convective derivative operators. J. Comput. Phys. **229**, 7180–7190 (2010). https://doi.org/10.1016/j.jcp.2010.06.006
27. S. Pirozzoli, F. Grasso, Direct numerical simulation of impinging shock wave/turbulent boundary layer interaction at M=2.25. Phys. Fluids. **18** (2006). https://doi.org/10.1063/1.2216989
28. Y. Na, P. Moin, Direct numerical simulation of a separated turbulent boundary layer. J. Fluid Mech. 0022-1120, 379 (1998)
29. R. Narasimha, The laminar-turbulent transition zone in the boundary layer. Prog. Aerospace Sci. **22**, 29–80 (1985)
30. A. Jirasek, Vortex-generator model and its application to flow control. J. Aircr. **42**(6), 1486–1491 (2005)
31. M. Choudhari, F. Li, C.-L. Chang, J. Edwards, M. Kegerise, R. King, Laminar-turbulent transition behind discrete roughness elements in a high-speed boundary layer, in *48th AIAA Aerospace Sciences Meeting Including the New Horizons Forum and Aerospace Exposition* (2010), pp. 1–21